Report No. K-TRAN: KSU-21-7 ▪ FINAL REPORT ▪ May 2026

Computationally Informed Methodologies for Capturing the Effect of Intervening Structures During Truck Impact Events: Phase II

Fahed H. Salahat, Ph.D.
Christopher A. Jones, Ph.D.
Hayder A. Rasheed, Ph.D., P.E.

Kansas State University Transportation Center

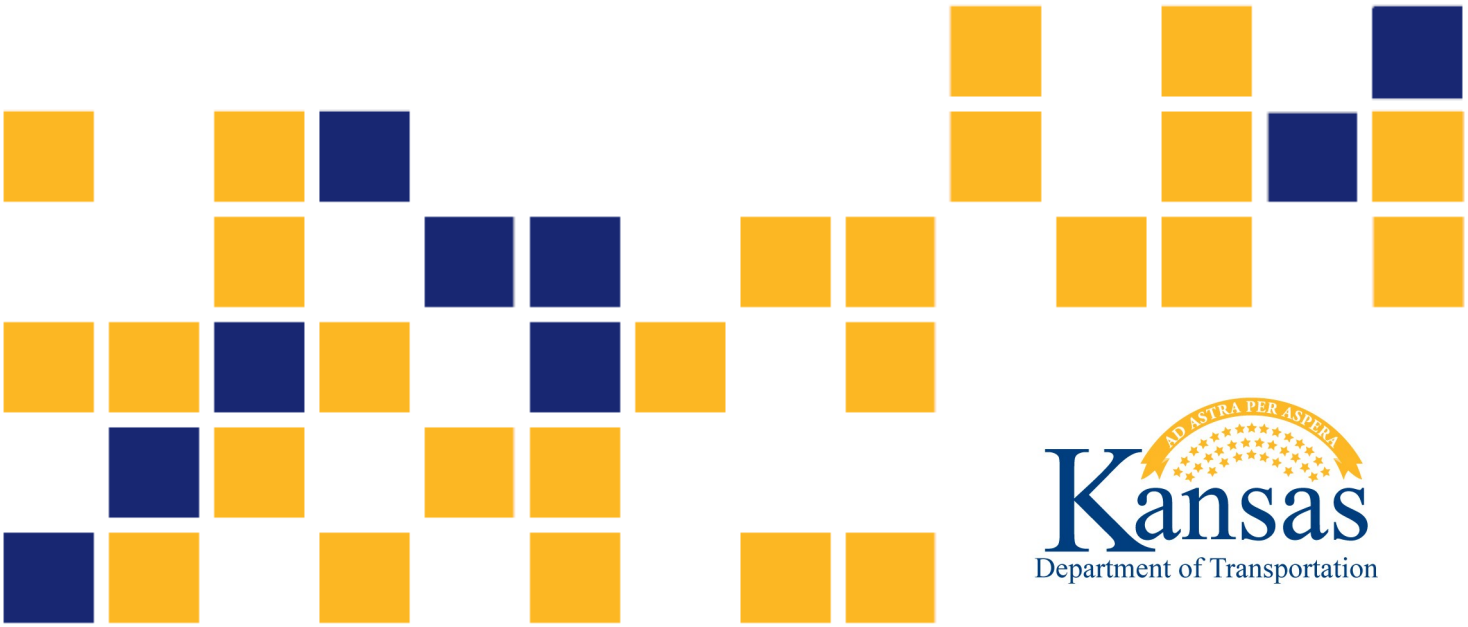

Kansas Department of Transportation

1 Report No. K-TRAN: KSU-21-7	**2 Government Accession No.**	**3 Recipient Catalog No.**
4 Title and Subtitle Computationally Informed Methodologies for Capturing the Effect of Intervening Structures During Truck Impact Events: Phase II		**5 Report Date** May 2026 **6 Performing Organization Code**
7 Author(s) Fahed H. Salahat, Ph.D.; Christopher A. Jones, Ph.D.; Hayder A. Rasheed, Ph.D., P.E.		**8 Performing Organization Report No.**
9 Performing Organization Name and Address Kansas State University Transportation Center Department of Civil Engineering 2118 Fiedler Hall 1701C Platt Street Manhattan, KS 66506-5000		**10 Work Unit No. (TRAIS)** **11 Contract or Grant No.** C2167
12 Sponsoring Agency Name and Address Kansas Department of Transportation Bureau of Research 2300 SW Van Buren Topeka, Kansas 66611-1195		**13 Type of Report and Period Covered** Final Report August 2020 – August 2023 **14 Sponsoring Agency Code** RE-0812-01
15 Supplementary Notes For more information write to address in block 9.		

16 Abstract

Reinforced concrete (RC) barriers are often used as railings to protect bridge piers against vehicular collision force (VCF). RC barriers absorb collision energy and/or redirect vehicles. According to bridge design specifications of the American Association of State Highway and Transportation Officials (AASHTO), barriers used to protect bridge piers should have a minimum height of 42 in. and survive MASH Test Level 5 (TL-5). Although many barriers in current use do not meet this requirement, these sub-standard barriers can reduce the severity of vehicle-pier collisions and decrease the AASHTO-specified VCF for pier resistance in upgraded bridges.

The primary objective of this research was to assess the performance of sub-standard RC barriers as protection for bridge piers against VCF and quantify their reduction of the equivalent static force (ESF) that piers must resist according to AASHTO specifications. This report describes current procedures to determine the transverse static capacity of RC barriers and proposes alternative, accurate methodologies. A matrix of crash scenarios is simulated in dynamic explicit analysis using the finite element software LS-DYNA to comprehensively encapsulate the behavior of sub-standard RC barriers. The investigated parameters include energy dissipation, velocity reduction, contact force absorption, and lateral displacement. This research also utilized a simulation matrix on a bridge pier that failed to withstand the ESF under the required AASHTO's extreme load event behind a sub-standard barrier. A series of dynamic impact force time histories was used to extract the ESF and compare the resulting ESF to the AASHTO-required force, leading to a proposed reduction in the ESF due to the presence of sub-standard RC barriers.

Research results showed that AASHTO's existing procedure to determine the transverse static capacity of RC barriers may underestimate capacity by approximately 50%. In addition, the inadequacy of sub-standard barriers to absorb and/or redirect an impacting vehicle was shown to relate to geometrical deficiency (insufficient height), meaning that sub-standard barriers can resist high-impact load demands and protect piers if the barrier is a sufficient height (i.e., 42 in. for TL-4). Sub-standard barriers may reduce the AASHTO-required ESF for bridge piers by at least 25%.

17 Key Words Bridges, Bridge piers, Reinforced concrete, Load and resistance factor design, Finite element analysis		**18 Distribution Statement** No restrictions. This document is available to the public through the National Technical Information Service www.ntis.gov.	
19 Security Classification (of this report) Unclassified	**20 Security Classification (of this page)** Unclassified	**21 No. of pages** 122	**22 Price**

Form DOT F 1700.7 (8-72)

This page intentionally left blank.

Computationally Informed Methodologies for Capturing the Effect of Intervening Structures During Truck Impact Events: Phase II

Final Report

Prepared by

Fahed H. Salahat, Ph.D.
Christopher A. Jones, Ph.D.
Hayder A. Rasheed, Ph.D., P.E.

Kansas State University Transportation Center

A Report on Research Sponsored by

THE KANSAS DEPARTMENT OF TRANSPORTATION
TOPEKA, KANSAS

and

KANSAS STATE UNIVERSITY TRANSPORTATION CENTER
MANHATTAN, KANSAS

May 2026

PREFACE

The Kansas Department of Transportation's (KDOT) Kansas Transportation Research and New-Developments (K-TRAN) Research Program funded this research project. It is an ongoing, cooperative and comprehensive research program addressing transportation needs of the state of Kansas utilizing academic and research resources from KDOT, Kansas State University and the University of Kansas. Transportation professionals in KDOT and the universities jointly develop the projects included in the research program.

NOTICE

The authors and the state of Kansas do not endorse products or manufacturers. Trade and manufacturers names appear herein solely because they are considered essential to the object of this report.

This information is available in alternative accessible formats. To obtain an alternative format, contact the Office of Public Affairs, Kansas Department of Transportation, 700 SW Harrison, 2nd Floor – West Wing, Topeka, Kansas 66603-3745 or phone (785) 296-3585 (Voice) (TDD).

DISCLAIMER

The contents of this report reflect the views of the authors who are responsible for the facts and accuracy of the data presented herein. The contents do not necessarily reflect the views or the policies of the state of Kansas. This report does not constitute a standard, specification or regulation.

Abstract

Reinforced concrete (RC) barriers are often used as railings to protect bridge piers against vehicular collision force (VCF). RC barriers absorb collision energy and/or redirect vehicles. According to bridge design specifications of the American Association of State Highway and Transportation Officials (AASHTO), barriers used to protect bridge piers should have a minimum height of 42 in. and survive MASH Test Level 5 (TL-5). Although many barriers in current use do not meet this requirement, these sub-standard barriers can reduce the severity of vehicle-pier collisions and decrease the AASHTO-specified VCF for pier resistance in upgraded bridges.

The primary objective of this research was to assess the performance of sub-standard RC barriers as protection for bridge piers against VCF and quantify their reduction of the equivalent static force (ESF) that piers must resist according to AASHTO specifications. This report describes current procedures to determine the transverse static capacity of RC barriers and proposes alternative, accurate methodologies. A matrix of crash scenarios is simulated in dynamic explicit analysis using the finite element software LS-DYNA to comprehensively encapsulate the behavior of sub-standard RC barriers. The investigated parameters include energy dissipation, velocity reduction, contact force absorption, and lateral displacement. This research also utilized a simulation matrix on a bridge pier that failed to withstand the ESF under the required AASHTO's extreme load event behind a sub-standard barrier. A series of dynamic impact force time histories was used to extract the ESF and compare the resulting ESF to the AASHTO-required force, leading to a proposed reduction in the ESF due to the presence of sub-standard RC barriers.

Research results showed that AASHTO's existing procedure to determine the transverse static capacity of RC barriers may underestimate capacity by approximately 50%. In addition, the inadequacy of sub-standard barriers to absorb and/or redirect an impacting vehicle was shown to relate to geometrical deficiency (insufficient height), meaning that sub-standard barriers can resist high-impact load demands and protect piers if the barrier is a sufficient height (i.e., 42 in. for TL-4). Sub-standard barriers may reduce the AASHTO-required ESF for bridge piers by at least 25%.

Acknowledgments

This research was made possible through funding from the Kansas Transportation Research and New-Developments (K-TRAN) program from the Kansas Department of Transportation (KDOT). Thanks are extended to KDOT team members in the Bureau of Structural and Geotechnical Services who supported the project during all its development stages. Special thanks are extended to Jeff Ruby and Mark Hurt.

Table of Contents

List of Tables

List of Figures

Abbreviations

AASHTO: American Association of State Highway and Transportation Officials

DIF: Dynamic Impact Force

ESF: Equivalent Static Force

FEA: Finite Element Analysis

FHWA: Federal Highway Administration

GESF: Global Equivalent Static Force

KDOT: Kansas Department of Transportation

LESF: Local Equivalent Static Force

LRFD: Load and Resistance Factor Design

MASH: Manual for Assessing Safety Hardware

NCHRP: National Cooperative Highway Research Program

PFMSA: Peak of Fifty Millisecond Average

PIF: Peak Impact Force

QoI: Quantities of Interest

RC: Reinforced Concrete

SUT: Single Unit Truck

TL: Test Level

TST: Tractor Semi-Trailer

TTI: Texas Transportation Institute

VCF: Vehicular Collision Force

YLA: Yield Line Analysis

Chapter 1: Introduction

1.1 Background

Critical infrastructures, such as bridges, must be able to resist extreme loading and potentially hazardous events such as vehicle collisions. Maintaining the structural integrity of bridge piers during vehicle collisions is critical for continued bridge operation. Many vehicle-pier collisions have had catastrophic consequences, as shown in Figure 1.1. Between 1951 and 2000, 31 of 617 (5%) of reported bridge collapses were caused by vehicle impact with bridge piers (Harik et al., 1990; Wardhana & Hadipriono, 2003).

Figure 1.1: Failure of Bridge Structures Due to Vehicle Collisions
Source: Nemec (2013)

The American Association of State Highway and Transportation Officials (AASHTO) first addressed vehicular collision force (VCF) as a design limit for bridge piers in the second edition of their AASHTO LRFD Bridge Design Specifications: SI Units, which required bridge piers to be designed to structurally resist an equivalent static force (ESF) of 400 kips (AASHTO, 1998). After studying a collection of crash data, analyzing bridge pier collision scenarios via finite element analysis (FEA), and collecting empirical data related to forces during full-scale collision tests, the research team at the Texas Transportation Institute (TTI) recommended increasing the ESF to 600 kips (Buth et al., 2010; Buth et al., 2011). The latest AASHTO LRFD Bridge Design Specifications (AASHTO, 2020) include this recommended value, as well as the suggested

redirection of vehicle impact or VCF absorption via bridge pier protection. One suggested protection method includes the use of an intervening structure that measures 42 in. high with a traffic face positioned at least 3.25 ft from the vulnerable component. The intervening structure should be able to survive a Test Level-5 (TL-5) crash event as specified in the guidelines of the AASHTO Manual for Assessing Safety Hardware (MASH) (AASHTO, 2016).

Reinforced concrete (RC) barriers are commonly used as intervening structures to protect bridge piers against VCF, but many RC barriers currently used in old bridge infrastructures do not meet the acceptance criteria for TL-5. Although these sub-standard barriers are inadequate for the sole protection of bridge piers against VCF, their presence helps reduce the severity of vehicle-pier collisions and they reduce the AASHTO-specified ESF for piers to account for the dynamic VCF. However, current AASHTO specifications neglect the presence of sub-standard barriers when considering VCF on bridge piers as demonstrated by the absence of research studies that accurately estimate the barriers' capacity, assesses their performance during crash events, and quantifies their reduction of required ESF resistance by piers. Therefore, accurate analysis methodologies are crucial to obtaining the structural capacity of sub-standard RC barriers and assessing their efficiency during crash events to determine their contribution to VCF absorption and ESF reduction.

This research utilized analytical methodologies to accurately estimate the lateral static capacity of RC barriers. Numerical simulations were conducted to investigate the behavior of a sub-standard RC barrier during vehicular collision events and evaluate its response under dynamic impact load effects. The numerical simulations were extended to estimate the VCF on bridge piers with a sub-standard RC barrier and the ESF reduction for piers according to current AASHTO specifications.

1.2 Aim and Objectives

The aim of this research was to assess the performance of sub-standard RC barriers as protective structures for bridge piers against VCF and to quantify their reduction of required ESF resistance per current AASHTO specifications. This study established the following objectives:

1. Develop rigorous analysis and innovative methodology to evaluate the transverse structural capacity of RC barriers.
2. Assess the performance of sub-standard RC barriers as protective structures for bridge piers against VCF.
3. Estimate the VCF on bridge piers with sub-standard intervening RC barriers.

1.3 Scope

This report is comprised of six chapters. Chapter 1 introduces the problem, defines the aim and objectives of this research, and explains the scope of the work. Chapter 2 contains a literature review and expanded background on the problem of this project; while Chapter 3 presents a detailed analysis to obtain the transverse load capacity of RC barriers using theories and mechanics of reinforced concrete while introducing an alternative innovative truss analogy method to simulate RC barriers and obtain their transverse capacity. Chapters 4 and 5 include explicit dynamic simulations of a matrix of crash events using the FEA program LS-DYNA. The simulation matrix of the crash environment consisted of only the barrier and the crashing vehicle. A comprehensive behavior analysis on the performance of sub-standard RC barriers during heavy vehicle crash events was conducted, including the discussion of several quantities of interest (QoI). The simulation matrix in Chapter 5 includes a representative bridge pier placed behind a sub-standard RC barrier. The time histories of the dynamic impact forces on the pier, including the peak impact force (PIF), were obtained via analysis of the simulation matrix. The ESF on the pier was then derived from the time histories. Conclusions and recommendations are presented in Chapter 6.

Chapter 2: Literature Review

2.1 Estimated Transverse Static Capacity of RC Barriers

RC barriers are utilized in transportation infrastructures for a variety of purposes. For example, median barriers are commonly used to separate opposing lanes of traffic, while railing barriers are used to prevent vehicle access to roadway shoulders and protect sign structures and pedestrians. RC barriers also are commonly used as intervening structures to protect bridge piers against VCF, meaning the estimated capacity of these barriers when subjected to VCF is essential for effective barrier design and placement. Successful placement of these barriers includes three main factors: (1) knowing the required performance level, (2) accurately analyzing and designing the barrier to fulfill the required performance level, and (3) testing the barrier to ensure the acceptance criteria is satisfied. The second factor (barrier analysis and design) has proven to be the most challenging because, despite set objectives (performance levels) and measures to determine if objectives are met (acceptance criteria), the analysis methodology leads to achieving the objectives.

The Ross et al. (1993) report was the first research to specify the performance levels and acceptance criteria for applying RC barriers as intervening structures. The performance levels, or Test Levels (TLs), in the Ross et al. (1993) report differ according to impact conditions, with a specific impact condition acting as a function of the vehicle designation (passenger car, single-unit truck (SUT), tractor-semi-trailer (TST), etc.), the impact speed, and the impact angle. Higher TLs indicate severe impact conditions, such as heavy vehicles travelling at high velocity. The report also includes three categories of acceptance criteria: structural adequacy, occupant risk, and post-impact vehicular trajectory. The criteria imply that a test article (barrier) is acceptable for a certain TL if it is structurally adequate to dissipate the energy of the impacting vehicle for that TL without excessive damage to the barrier or penetration and minimizes the risk of occupant injury and any potential subsequent multivehicle accident by bringing the impacting vehicle to a controlled stop (Ross et al., 1993).

The Ross et al. (1993) report also recommends procedures that were implemented by the Federal Highway Administration (FHWA) in 1998, followed by AASHTO's MASH in 2009, which upgraded the impact conditions for some TLs to reflect more damaging crash events and

produce more robust barriers for certain applications. The most current MASH (AASHTO, 2016) is included in the AASHTO LRFD Bridge Design Specifications (AASHTO, 2020) to define TLs that determine design forces for traffic railings. The various TLs according to AASHTO (2016) are shown Table 2.1.

Table 2.1: MASH Test Levels

Vehicle Type	Small Automobiles	Pickup Truck	Single-Unit Truck	Tractor-Trailer	Tractor-Tanker-Trailer
Mass, kips (ton)	2.4–3.3 (1.1–1.5)	5 (2.27)	22 (10)	80 (36)	80 (36)
Angle of attack	25°	25°	15°	15°	15°
		Speed, mph (km/h)			
TL-1	31 (50)	31 (50)	N/A	N/A	N/A
TL-2	31 (50)	44 (70)	N/A	N/A	N/A
TL-3	62 (100)	62 (100)	N/A	N/A	N/A
TL-4	62 (100)	62 (100)	56 (90)	N/A	N/A
TL-5	62 (100)	62 (100)	N/A	50 (80)	N/A
TL-6	62 (100)	62 (100)	N/A	N/A	50 (80)

N/A: not applicable

After determining the performance level and acceptance criteria, designing the barrier to meet the performance level and pass the acceptance criteria is the next challenge. Barriers are typically designed to resist certain levels of loading and satisfy geometry proportioning; Table A13.2.1 in AASHTO (2020) shows the design forces and designations for traffic railings required for various TLs. Hirsch (1978) first introduced the yield line analysis (YLA), the most common analysis method to verify if a proposed barrier design meets performance level requirements. The YLA, which is currently included in AASHTO (2020), synthesizes the work done by external applied forces and internal energy via the formation of yield lines due to a triangular (V-shaped) failure pattern. However, the current AASHTO procedure of YLA includes assumptions that are intended to simplify the analysis process but are criticized by many researchers due to the

inaccurate capacity estimation and failure pattern. Jeon et al. (2008) conducted a full-scale test to vary the loading patterns and simulate vehicle crashes. The results revealed a lower load than the load predicted by AASHTO's equations and a failure pattern that resembled a W-shaped failure pattern. Cao et al. (2020) confirmed this failure pattern using dynamic explicit numerical simulations and quasi-static pushover analysis. When Loken et al. (2021) compared the traditional V-shaped and the W-shaped (modified YLA) failure patterns in terms of punching shear capacities, the results revealed a significant increase of punching shear capacity in the modified YLA. Although punching shear is a potential failure mechanism reported in many studies (Alberson et al., 2005; Williams et al., 2007; Sennah et al., 2018), it is less likely for this failure mode to control with sufficient transverse reinforcement.

The existing literature agrees that AASHTO's current YLA procedure must distinguish between using the YLA as an initial qualifier for proposed barrier designs and judging barrier capacity for decisions related to barrier structural adequacy and crashworthiness. The former is a conservative analysis that produces barriers designed with excessive capacity, while the latter yields a very conservative analysis that significantly underestimates the actual capacity of RC barriers. While both cases have negative economic effects, underestimating the capacity of existing RC barriers is more significant because the load demands for some upgraded TLs prevent many of these barriers from being considered structurally adequate. For example, Rosenbaugh et al. (2007) designed and developed a TL-5 RC barrier for which the AASHTO YLA procedure was used to verify the initial loading capacity and geometric requirements according to Table A13.2.1 (AASHTO, 2020). Then the barrier underwent cycles of design cost optimization before it was subjected to an actual TL-5 crash event to pass the acceptance criteria.

Comparatively, Bullard et al. (2010) conducted an experimental study of crash tests to evaluate the performance of common barriers according to the upgraded MASH requirements. Results showed that 45% of the tested barriers failed to meet the acceptance criteria due to vehicle rollovers, but no significant damage (e.g., major structural cracks or barrier penetration) was observed. This failure was shown to relate to geometrical deficiency (insufficient height). Similarly, Salahat et al. (2023) conducted a numerical dynamic analysis study to estimate the VCF transferred to bridge piers in the presence of a disqualified RC Jersey-shaped barrier as a protective

structure to bridge piers. The results showed that the disqualified barrier reduced the equivalent static load demand by at least 25%. The remaining load transferred to the pier was a result of contact between the cargo area and the pier; no structural damage or penetration of the barrier was observed.

Guidance regarding detailed analysis methods and procedures is essential to accurately estimate the structural capacity of RC barriers and distinguish geometrical deficiencies from structural inadequacy related to the acceptance criteria. Chapter 3 of this research presents a rigorous YLA according to the current and common V-shaped failure pattern. Many simplifying assumptions are eliminated, a clear analytical solution is presented, and an original and innovative alternative method is introduced to predict the lateral capacity of RC barriers using a truss analogy model. The developed model provides guidelines to simulate the RC barrier as an equivalent space truss. This approach uses incremental analysis to track the formation of the V-shaped yield lines. Finally, Chapter 3 includes an analysis of a case study of an RC barrier using rigorous YLA, the equivalent truss method, and the numerical FEA via Abaqus. The results of this work confirm the accuracy of the proposed solutions, and the scope of the work in Chapter 3 includes the flexural capacity of barriers since shear failure avoidance is assumed due to sufficient distribution of transverse reinforcement.

2.2 Performance of RC Barriers During Vehicular Collision Events

When RC barriers are used as intervening structures against vehicular impacts, they are expected to be subjected to VCF. The performance of these barriers depends on factors such as the barrier profile (cross sectional shape and size), base boundary condition (fixed or free boundary condition), and the barrier segment length. Ross et al. (1993) provides guidelines to evaluate the safety of roadside features, such as concrete barriers. These guidelines address the various test levels that correspond to different applications and the performance acceptance criteria. These levels are functions of the impacting vehicle type and the impact conditions (angle of attack and initial velocity). The acceptance criteria are comprised of three factors: structural adequacy, occupant risk, and post-impact vehicular response. The structural adequacy factor corresponds to the barrier's ability to contain and redirect the impacting vehicle or absorb the VCF from the crash

event and bring the impacting vehicle to a controlled stop. This factor is directly related to barrier performance when protecting bridge piers. The latter two factors relate to the safety of vehicle occupants due to impact and the likelihood of the vehicle subsequently colliding with another vehicle or fixed object. After the FHWA implemented these guidelines in 1998, transportation agencies began to follow these guidelines when designing barriers to meet the performance criteria corresponding to various test levels. In 2009, when AASHTO published MASH with improved guidelines from Ross et al. (1993), the requirements for certain test levels were upgraded to reflect more damaging crash events, as shown in Table 2.1. The current FHWA recommendation is to evaluate the protective barriers in accordance with MASH guidelines.

The upgraded MASH requirements rendered many existing concrete barriers as insufficient for the corresponding test level. As mentioned, Bullard et al. (2010) conducted an experimental study of 11 crash tests to evaluate the performance of nine types of common roadside safety hardware, including concrete barriers, under the upgraded MASH requirements. Results showed that five of the 11 crash tests (45%) failed to meet the evaluation criteria. Among the failing barriers was the Jersey-shaped barrier tested under a TL-4 crash event. These barriers are currently in wide use because they were installed before the minimum height required to survive high test levels was recognized. Notably, only approximately 10% of current bridge infrastructure in the United States was built after 2009, the year when the first MASH was published (FHWA, 2022). In the experimental program by Bullard et al. (2010), this barrier included only qualitative description about its structural adequacy, meaning no information about the resulting impact force or lateral displacement of the barrier was presented. Therefore, the performance of this barrier with the upgraded MASH requirements must be extensively assessed for different test levels.

Because full-scale testing is neither easy to accomplish nor economically feasible for many agencies, numerical simulations can provide a comprehensive view of crash behavior and yield accurate parameters since the simulations validate a suitable experimental reference. For example, Itoh et al. (2007) simulated a crash event of a 44-kip truck impacting a median F-shaped concrete barrier with a clear height of 44 in. plus 12 in. into the pavement. The barrier segment length, the velocity, and the angle of attack were 164 ft, 62 mph, and 17°, respectively. The barrier, which successfully passed the structural adequacy criterion, redirected the truck with a maximum lateral

displacement of the barrier of approximately 1 in. and a maximum impact force of approximately 225 kips. Atahan (2009) simulated a 66-kip truck impacting Jersey-shaped barriers with heights of 32, 38, 40, and 42 in. to examine the effect of barrier height on vehicle stability after collision. The angle of attack and impact speed were 20° and 40 mph, respectively. The author concluded that the 42-in. barrier height was the only height that redirected the vehicle without causing the vehicle to roll over the barrier. In another study, Cao et al. (2020) simulated two crash events for TL-4 and TL-5. The barrier for TL-4 was single sloped with a clear height of 36 in., while the TL-5 barrier was a Jersey-shaped barrier with a clear height of 42 in. Both barriers redirected the impacting vehicles with a lateral displacement and impact force during the TL-4 event of approximately 0.5 in. and 124 kips, respectively, and approximately 0.47 in. and 281 kips, respectively, during the TL-5 event.

Although the described simulations are informative, the simulated crash events, with the exception of the TL-5 event by Cao et al. (2020), do not align with specific MASH test levels (Table 2.1). Also, none of the previous simulations evaluated barriers as intervening structures to protect bridge piers against VCF. Rather, the primary focus of most barrier impact studies has been the crashworthiness of a particular barrier design (e.g., barrier ability to redirect an impacting vehicle). AASHTO's requirements for a standard barrier used for bridge pier protection include a barrier minimum clear height of 42 in. and the barrier must survive a MASH TL-5 crash event. Consequently, since many bridges in the United States were constructed prior to the upgraded MASH requirements, many sub-standard barriers are currently in use as bridge pier protection, meaning a comprehensive study of the behavior of sub-standard barriers used as protective structures against VCF during MASH crash events is necessary.

As described in Chapter 4, this study conducted a matrix of numerical simulations using LS-DYNA in which the common Jersey-shaped barrier (designed prior to the upgraded MASH guidelines) was subjected to a MASH TL-4 crash event (22 kips SUT traveling at 56 mph) and a MASH TL-5 crash event (80 kips TST traveling at 50 mph). The QoI in this study were impact force, energy dissipation, velocity reduction, and lateral displacement. Based on the results, discussion about the structural adequacy of the sub-standard barrier, as well as a case study

reflecting the effectiveness of the sub-standard barrier for protecting bridge piers during a TL-4 crash event, are presented in Chapter 4.

2.3 VCF Estimation of Bridge Piers

Bridge infrastructures are essential for connecting communities and providing uninterrupted passage for travelers. When the purpose of a bridge is to span roadways, however, bridge piers are often subject to extreme loading events due to vehicle collisions with the piers. The severity of collision consequences depends on factors such as the type and velocity of vehicle in the crash and the condition of the bridge infrastructure. Some collision events have caused severe damage to the bridges, including pier fracture and complete collapse, while other events have caused only slight damage, such as concrete cracking or spalling at the location of impact (Zhou et al., 2017).

According to FHWA (2022), 620,699 bridges were located throughout the United States in 2022. Bridge conditions were classified as good, fair, or poor based on the condition of bridge components, including sub-structural elements such as bridge piers. According to the report, an estimated 66% of bridges in the United States are classified as poor-fair condition, revealing the increased risk of bridge failure when the piers are subjected to loading events such as VCF.

VCF was first addressed by AASHTO (1998), in which AASHTO required bridge piers to be designed to structurally resist a lateral static force of 400 kips to account for VCF. Several subsequent studies have evaluated the VCF and structural elements to quantify an ESF that can be used for analysis and design. For example, El-Tawil et al. (2005) conducted an FEA of vehicles colliding with a bridge pier and proposed that 400 kips insufficiently represents the impact force in some crash scenarios.

After studying a collection of crash data, analyzing bridge pier collision scenarios via FEA, and collecting empirical data of forces during full-scale collision tests, the research team at TTI recommended increasing the VCF to 600 kips (Buth et al., 2010; Buth et al., 2011), as adopted in AASHTO (2020). Thus, any upgrades or changes to an existing bridge must consider the VCF per the latest AASHTO requirements. Old bridges with poor-fair sub-structures have piers that often fail to satisfy the strength requirement. Such piers are hereby referred to as under-designed piers.

However, because design consideration of VCF using structural resistance may require expensive rehabilitation and repairs, AASHTO recommends redirecting or absorbing the VCF by protecting bridge piers. One method is to use a 42 in. high intervening structure with a traffic face more than 3.25 ft from the pier. The structure should be able to survive a TL-5 crash event as specified in MASH (Table 2.1). Although this solution may be convenient for newly constructed bridges, existing bridges often have piers within 3 ft from the barrier or barriers that do not pass the acceptance criteria for a TL-5 crash event, or a combination of the two cases (piers within 3 ft (1 m) distance and sub-standard barrier), as shown in Figure 2.1. Consequently, the structural resistance and intervening structure fail to address the VCF according to AASHTO requirements.

Therefore, Chapter 5 proposes a new approach to address the VCF using a blended contribution of the existing sub-standard barrier and the under-designed pier. This approach was developed and validated via dynamic simulation of an envelope of crash events with varying key parameters to investigate the worst-case scenario. Crash events corresponding to TL-4 for SUT and TL-5 for TST in Table 2.1 were considered, and simulations were conducted using LS-DYNA.

Figure 2.1: KS-177 Intersection with Interstate 70 (S-W)
Source: Google Maps (n.d.)

Chapter 3: Rigorous Analysis to Evaluate the Transverse Static Capacity of RC Barriers

Among their many uses, RC barriers are often used as railings to protect bridge piers against VCF, meaning they must be designed to absorb collision energy and/or redirect a vehicle away from the piers. Efficient design and placement of RC barriers depend on the accurate estimation of barrier capacity during crash events. AASHTO utilizes YLA to predict barrier capacity using assumptions and simplifications that significantly underestimate a barrier's actual capacity and potentially disqualify many existing RC barriers due to structural inadequacy. Consequently, many researchers have proposed alternative failure patterns and methodologies to better predict the capacity of RC barriers. This research shows that the AASHTO YLA, with the current failure mechanism, can accurately predict barrier capacity when certain simplifying assumptions are eliminated. This research also presents an alternative innovative truss analogy model to accurately predict RC barrier capacity. The results of the rigorous YLA and the proposed truss model, which were validated by FEA via Abaqus, provide analysis guidance for accurate estimation of RC barrier capacity using YLA for design and/or assessment.

3.1 AASHTO YLA Procedure

The simplified YLA procedure by AASHTO utilizes the following assumptions, some of which are reasonable, while others may significantly underestimate RC barrier capacity:

1. The deck has sufficient resistance to the applied transverse forces; thus, the yield line failure pattern will remain within the parapet.
2. The parapet has sufficient longitudinal length to produce the assumed V-shaped yield line failure pattern.
3. The flexural capacity of the RC barrier is only due to the concrete; the contribution of the stirrups and/or ties prevents shear and diagonal tension.
4. The wall resistance is the average of its value along the height when the width of the barrier varies along the height.
5. The negative and positive wall resisting moments are equal.

In the first and second assumptions, the deck slab is usually heavily reinforced to sufficiently anchor the parapet dowels, and barriers are typically long enough to ensure the development of yield lines according to the suggested V-shaped failure pattern. The last three assumptions, however, often cause underestimation. For example, the third assumption neglects longitudinal and transverse reinforcement, resulting in decreased flexural capacity. In the fourth assumption, the cantilever action produces a moment around an axis parallel to the longitudinal axis of the bridge; this moment demand has a minimum linear function at the top of the barrier that peaks at the support. Therefore, averaging the sectional capacity along the height reduces the flexural capacity at locations of high demand and increases the capacity where it is not needed. The three zones in Figure 3.1 indicate that the flexural capacity function has geometrical (width) discontinuity along the height of the barrier and when calculating the capacity function around an axis vertical to the longitudinal axis of the barrier.

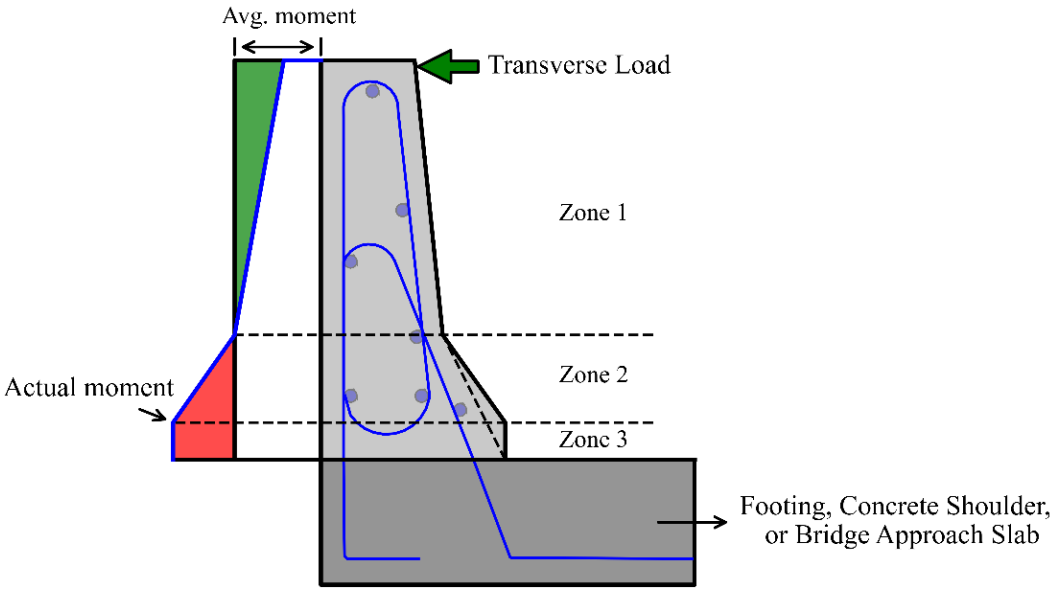

Figure 3.1: Variation of Actual versus Assumed Moment Capacity

In the final assumption, equating the positive and negative resisting moment does not make a big difference because of the third and fourth assumptions. However, if the barrier's reinforcement is considered when calculating the flexural capacity, minimum variation between the positive and negative sectional capacities occurs around the longitudinal axis (x-axis in Figure

3.2) because each side has the same number of stirrups. Comparatively, the sectional capacity around the vertical axis (z-axis in Figure 3.2) is lower at the back side of the barrier (less longitudinal rebar), which can be conservatively used for positive and negative moments as described in the fifth assumption. According to the proposed V-shaped failure pattern, this lower resistance from the positive moment represents the two front yield lines for resisting components around the vertical axis *Mz* in Figure 3.2. Therefore, the error imposed by these assumptions accumulates to result in significant underestimation of the barrier's transverse capacity. Equations 3.1 and 3.2 are the current equations per AASHTO (2020) based on the previous assumptions:

$$R_w = \left(\frac{2}{2L_c - L_t}\right) \times \left(8M_b + 8M_z + \frac{M_x {L_c}^2}{H}\right)$$

Equation 3.1

$$L_c = \frac{L_t}{2} + \sqrt{\left(\frac{L_t}{2}\right)^2 + \frac{8H(M_b + M_z)}{M_x}}$$

Equation 3.2

Where:

Rw = total transverse resistance of the railing (kips),

Lc = critical length of yield line failure pattern (ft),

Lt = longitudinal length of distribution of impact force Ft (ft), specified in (Table A13.2-1) (AASHTO, 2020),

Mb = additional flexural resistance of beam in addition to *Mz* at top of wall (kip-ft),

Mx = flexural resistance of cantilevered walls about an axis parallel to the longitudinal axis of the bridge (kip-ft/ft), (i.e., Mc in AASHTO specifications),

Mz = flexural resistance of the wall about its vertical axis (kip-ft), (i.e., *Mw* in AASHTO specifications), and

H = height of wall (ft).

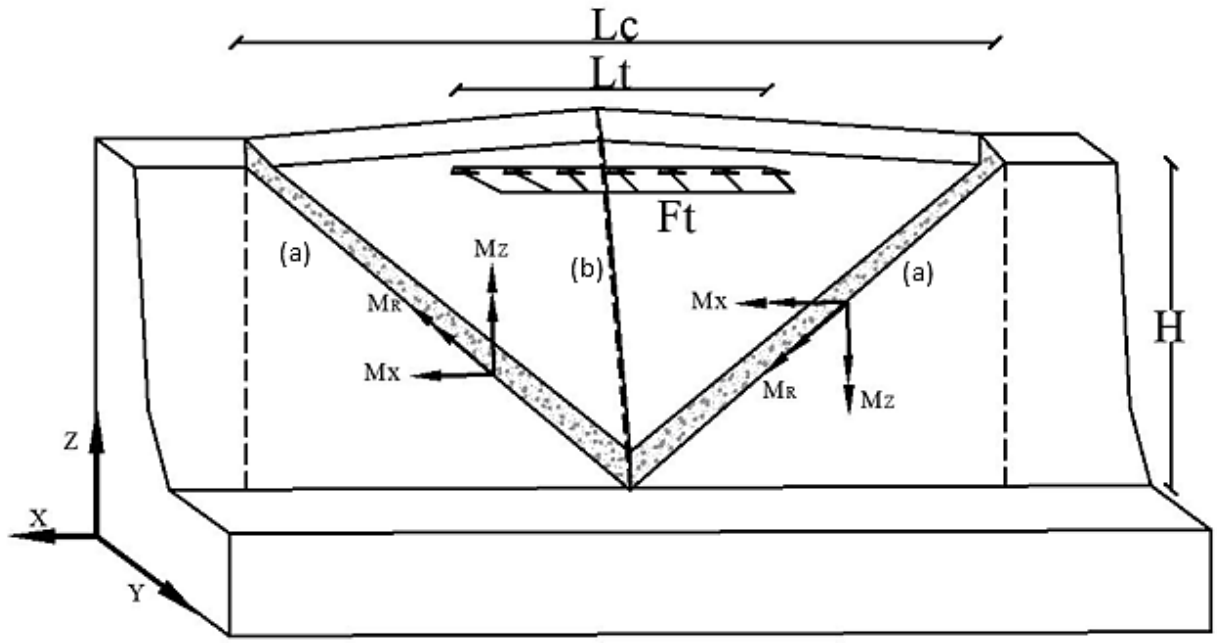

Figure 3.2: Difference in Negative and Positive Moments Capacities: (a) Represents Face Yield Lines, (b) Represents Back Yield Line

Total transverse resistance *Rw* should be equal to or greater than *Ft*, the resultant transverse force specified in AASHTO (2020) and assumed to be acting at top of a concrete wall.

3.2 Rigorous YLA of RC Barriers

The procedure in this section covers the generalized case of RC barriers when the barrier width is not uniform along its height and the positive and negative flexural capacities are not equal due to differences in reinforcement distribution at the back and front faces of the barrier. This procedure also covers other simpler barriers configurations, such as when the barrier has uniform width along its height or the reinforcement is similar at both sides.

3.2.1 Sectional Capacity

The flexural capacity around a certain axis is determined by dividing the barrier into sections at locations of geometrical discontinuities. For example, as shown in Figure 3.1, the moment function of zone 2 is merged with the moment function of zone 3 by following the sloped dotted line in Figure 3.1. The procedure for obtaining the sectional flexural capacity around the

vertical and longitudinal axes is shown in Figures 3.3(a) and (b), respectively. The procedure shown in Figure 3.3 is detailed in the case study section (Section 3.4).

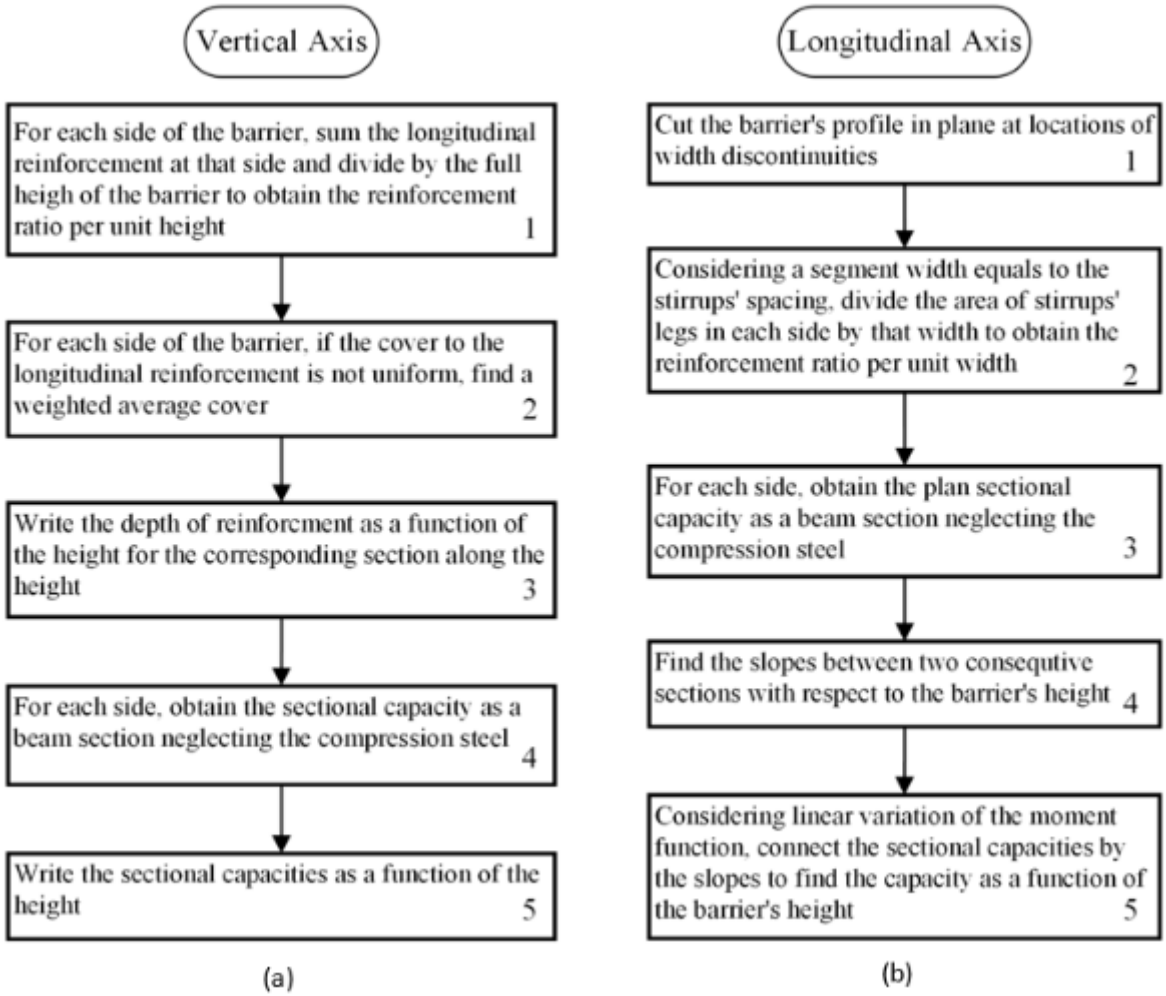

Figure 3.3: Procedure to Obtain Sectional Capacity around (a) Vertical Axis, (b) Longitudinal Axis

3.2.2 Formation of Yield Lines

The following assumptions were made to develop the yield line analysis:

1. Concrete is inextensible through the thickness.
2. For barriers that have sloped sides, the value of the deformation angle measured with respect to an assumed vertical plane and the deformation

angle of the actual sloped side is almost the same. Therefore, the angle used in the derivations are referenced with respect to the vertical plane.

To prove the second assumption, this study considered a unity deformation at the top of a barrier with two slopes, as shown in Figure 3.4. The rotation of the vertical plane is given in Equation 3.3.

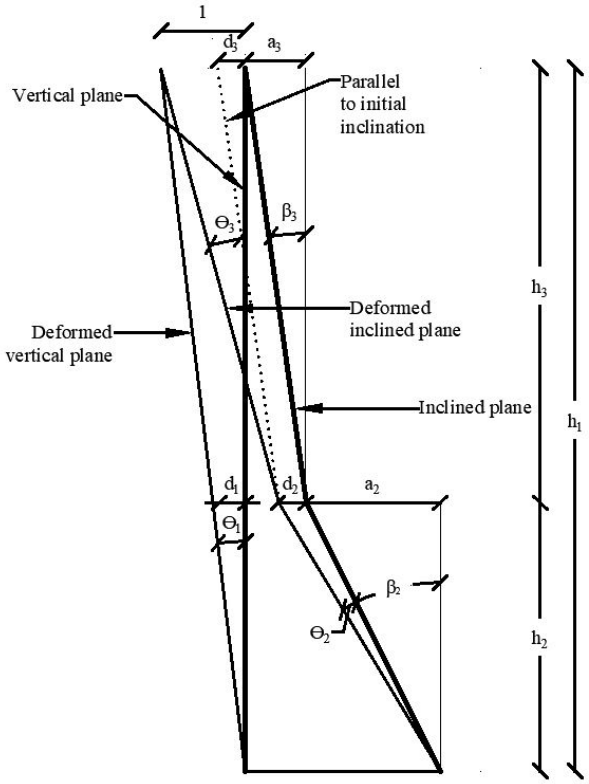

Figure 3.4: Rotations of Inclined versus Vertical Planes

$$\boldsymbol{\theta_1 = tan^{-1}\frac{1}{h_1}}$$

Equation 3.3

Distance d_1 was obtained using Equation 3.4. Using the first assumption regarding the inextensibility of concrete, distances d_1, d_2, and d_3 should be equal.

$$\boldsymbol{d_1 = d_2 = d_3 = h_2 tan\,\theta_1 = \frac{h_2}{h_1}}$$

Equation 3.4

Distances a_2 and a_3 are given in Equations 3.5 and 3.6, respectively.

$$\boldsymbol{a_2 = h_2 tan\, \beta_2}$$

Equation 3.5

$$\boldsymbol{a_3 = h_3 \tan \beta_3}$$

Equation 3.6

The tangent of total inclination at the lower part of the barrier is given as:

$$\boldsymbol{\tan (\beta_2 + \theta_2) = \frac{a_2 + d_2}{h_2}}$$

Equation 3.7

Substituting the values of d_2 and a_2 from Equations 3.4 and 3.5 into Equation 3.7 yields:

$$\boldsymbol{\tan (\beta_2 + \theta_2) = \frac{1 + h_1 \tan \beta_2}{h_1}}$$

Equation 3.8

Expanding the tangent of two summed angles using trigonometric identities and simplifying the expression gives the rotation of the lower part as:

$$\boldsymbol{\theta_2 = tan^{-1} \frac{1}{h_1 + h_1 tan^2 \beta_2 + tan\, \beta_2}}$$

Equation 3.9

Similarly, the tangent of total inclination at the upper part of the barrier is:

$$\boldsymbol{tan\, (\beta_3 + \theta_3) = \frac{1 + a_3 - d_3}{h_3}}$$

Equation 3.10

Substituting the values of d_3 and a_3 from Equations 3.4 and 3.6 yields:

$$\boldsymbol{\tan (\beta_3 + \theta_3) = \frac{1 + h_1 \tan \beta_3}{h_1}}$$

Equation 3.11

Expanding the tangent of two summed angles using trigonometric identities and simplifying the expression gives the rotation of the upper part as:

$$\boldsymbol{\theta_3 = tan^{-1} \frac{1}{h_1 + h_1 tan^2 \beta_3 + tan\, \beta_3}}$$

Equation 3.12

Equations 3.9 and 3.12 show that the rotation of the upper part is similar to the rotation of the lower part because they both depend on the initial inclination of the corresponding surfaces (β_2 and β_3). Differences between Equations 3.3, 3.9, and 3.12 are due to extra terms in the denominator. However, these extra terms are small compared to h_1. Because all the calculations are based on an exaggerated unit deformation at the tip, the actual angle difference is even smaller for the small deformation theory. Therefore, the detailed YLA equations derived in the following section are based on rotations with respect to the vertical plane (θ_1).

Internal work along the yield lines is the sum of the products of the yield moments and the rotations through which they integrate along the barrier height (z-axis). Rotations that correspond to *Mz(z)* and *Mx(z)* are $\theta z(z)$ and $\theta x(z)$, respectively, as shown in Figure 3.5 and Equations 3.13–3.16.

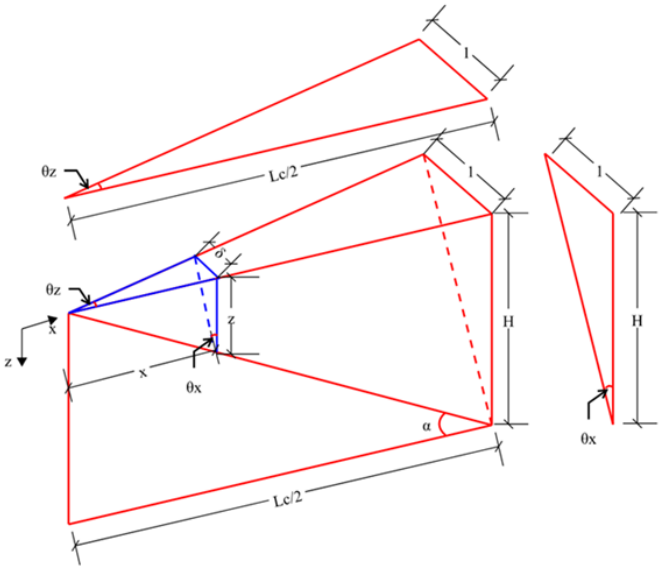

Figure 3.5: Formation of Yield Lines

$$\boldsymbol{\theta z(z) = \frac{\delta}{x}}$$

Equation 3.13

$$\boldsymbol{\frac{\delta}{1} = \frac{x}{L_c/2} \rightarrow \delta = \frac{2\,x}{L_c} = \frac{2\,z}{L_c\,tan\,\alpha}}$$

Equation 3.14

$$\boldsymbol{x = \frac{z}{tan\,\alpha}}$$

Equation 3.15

$$\boldsymbol{L_c = \frac{2H}{tan\,\alpha}}$$

Equation 3.16

Substituting Equations 3.14 and 3.15 into Equation 3.13 results in:

$$\boldsymbol{\theta z(z) = \frac{tan\,\alpha}{H}}$$

Equation 3.17

Rotation about the horizontal axis is given in Equations 3.18:

$$\boldsymbol{\theta x(z) = \frac{\delta}{z}}$$

Equation 3.18

Substituting Equations 3.14 and 3.16 into Equation 3.18 results in:

$$\boldsymbol{\theta x(z) = \frac{1}{H}}$$

Equation 3.19

Finally, the differential distance along an inclined yield line d_s is given in terms of d_z will be resolved into two components: dx and dz. As the integration is with respect to the depth Z, *dx* is given in terms of *dz* by differentiating Equations 3.15 in terms of z.

$$\boldsymbol{d_s = \sqrt{dx^2 + dz^2} = dz\sqrt{\left(\frac{dx}{dz}\right)^2 + 1} = dz\sqrt{1 + cot^2\alpha} = dz.csc\,\alpha}$$

Equation 3.20

3.2.3 Internal Work Along Yield Lines

After obtaining geometrical relationships of the moments and the rotations along the formed yield lines, the integrals of the internal work along the yield line at the back of the barrier that are associated with two rotations around the z-axis (one rotation from each triangular piece) and the two face yield lines are given as:

$$\boldsymbol{U_i = \int_0^H M_{z\,back}(z) \times 2\theta_z \times dz + 2\int_0^{L_c/2} M_{x\,front}(z) \times \theta_x \times dx + 2\int_0^H M_{z\,front}(z) \times \theta_z \times dz}$$

Equation 3.21

The integration direction shown in Figure 3.5 will be from top to bottom for the Z-direction and from left to center for the X-direction (or right to center when considering the right segment of the barrier). That is, when $x = 0 \rightarrow z = 0$, and when $x = {}^{L_c}/_2 \rightarrow z = H$. Also, from Equations 3.17 and 3.19, the rotations in both directions along the yield line are constants. Substituting Equations 3.17, 3.19 and 3.20 into 3.21 gives:

$$\boldsymbol{U_i = 2\int_0^H \frac{M_{z\,back}(z) \times \tan\alpha \times dz}{H} + 2\int_0^H \frac{M_{x\,front}(z) \times \cot\alpha \times dz}{H} + 2\int_0^H \frac{M_{z\,front}(z) \times \tan\alpha \times dz}{H}}$$

Equation 3.22

3.2.4 External Work by Applied Loads

The length of contact between the vehicle and the concrete barrier is L_t in Figure 3.6, and the force applied by the vehicle is equal to F_t. The value of L_t is specified in AASHTO (2020).

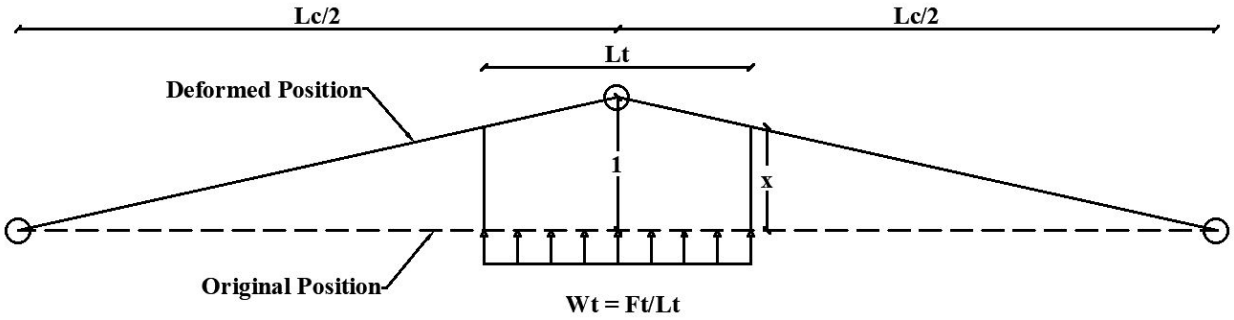

Figure 3.6: Top View of Vehicle-Barrier Contact

The external work is given as:

$$\boldsymbol{U_e = \frac{1}{2} \times (1 + x) \times \frac{L_t}{2} \times W_t \times 2 = \frac{L_t\, W_t\, (1 + x)}{2}}$$

Equation 3.23

Using similar triangles in Figure 3.6, the value of x can be:

$$\boldsymbol{x = 1 - \frac{L_t}{L_c}}$$

Equation 3.24

Substituting the value of L_c from Equation 3.16 into Equation 3.24 and then back into Equation 3.23 gives the external work as:

$$\boldsymbol{U_e = L_t\, W_t \left(1 - \frac{L_t\, tan\, \alpha}{4H}\right)}$$

Equation 3.25

When the load acting on the barrier is concentrated at one point (the tip of the barrier), Equation 3.25 becomes:

$$\boldsymbol{U_e = F_t \times 1 = F_t}$$

Equation 3.26

Where load F_t is the applied concentrated load.

Equating the internal work from Equation 3.22 with the external work from Equations 3.25 or 3.26 yields the solution for W_t and F_t as in Equations 3.27 and 3.28, respectively. A closed-form solution for Equation 3.27 and Equation 3.28 can be obtained by solving $\frac{dWt}{d\alpha} = 0$, $\frac{dFt}{d\alpha} = 0$, respectively. Another approach to solving for the critical load is to plot their functions against a range of angles for α and then select the minimum value of W_t in Equation 3.27 and F_t in Equation 3.28, as conducted for the case study for this research.

$$\boldsymbol{W_t = \frac{2\left(\int M_{z\,back}(z) \times tan\, \alpha \times dz + \int M_{x\,front}(z) \times cot\, \alpha\, dz + \int M_{z\,front}(z) \times tan\, \alpha \times dz\right)}{H \times L_t \left(1 - \frac{L_t\, tan\, \alpha}{4H}\right)}}$$

Equation 3.27

$$F_t = \frac{2\left(\int M_{z\,back}(z) \times \tan\alpha \times dz + \int M_{x\,front}(z) \times \cot\alpha\, dz + \int M_{z\,front}(z) \times \tan\alpha \times dz\right)}{H}$$

Equation 3.28

3.3 Truss Analogy

One of the primary contributions of this research is an innovative approach for obtaining the ultimate transverse capacity of RC barriers. The approach is based on an equivalent space truss model with properties defined to mimic the reinforcement of an actual RC barrier. This analogy differs from the AASHTO YLA presented in Section 3.1 because it relates barrier capacity to the steel reinforcement only and neglects the contribution of the concrete.

3.3.1 Modeling Concept

The space truss model represents the flexural capacity of the barrier about the longitudinal and vertical axes by truss elements. The truss profile has the same shape as the barrier stirrups, and the vertical framing elements of the truss have equal area and spacing to existing stirrups in the actual barrier, as shown in Figure 3.7(a). Longitudinal reinforcement of the barrier is distributed on the truss elements that run longitudinally, as shown in Figure 3.7(b). Diagonal members were provided to satisfy the barrier's ability to transfer shear forces and diagonal tension.

3.3.2 Equivalent Failure Mechanism

The proposed failure mechanism to simulate barrier failure tracks the yielding of a vertical or longitudinal bar at a junction node along the first yield line, as shown in Figure 3.8. The tracked members on the front face of the barrier represent two diagonal yield lines. By the time the two yield lines complete formation, the back yield line is formed, meaning the ultimate capacity of the barrier depends on the completion of those two yield lines.

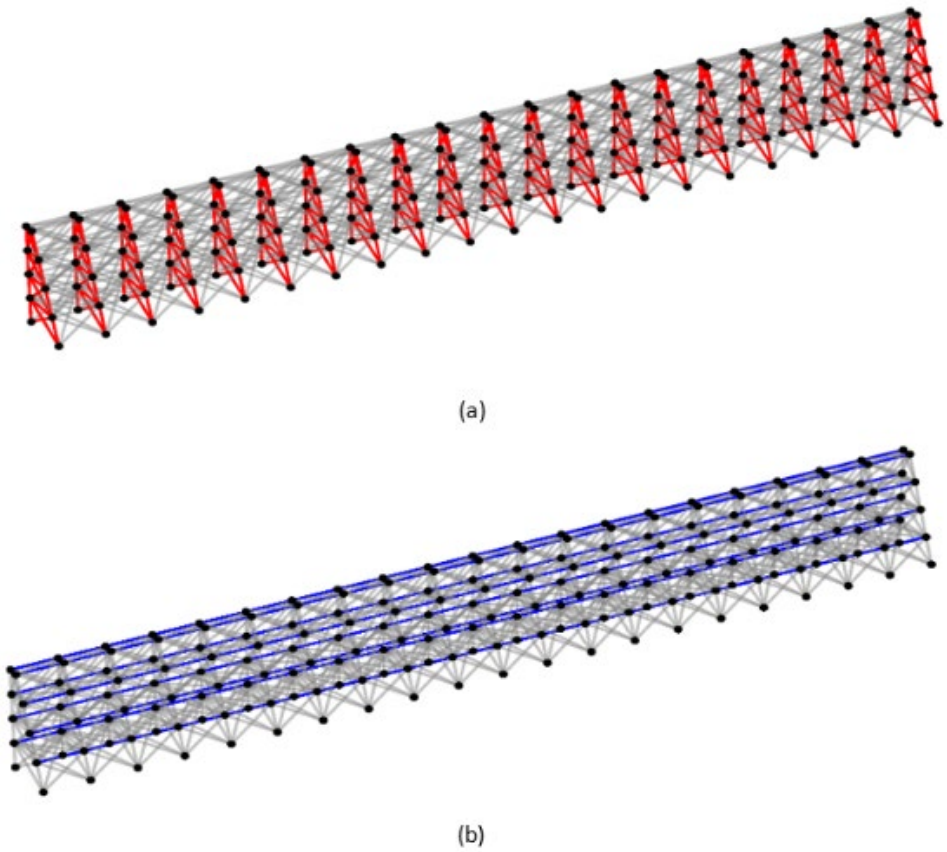

Figure 3.7: Truss Analogy: (a) Vertical Frames for Stirrups, (b) Longitudinal Elements for Longitudinal Reinforcement

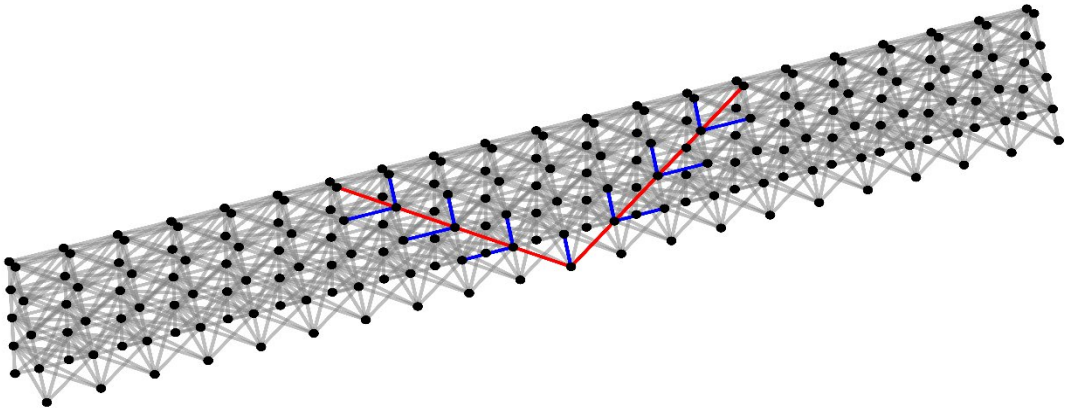

Figure 3.8: Truss Analogy with Formation of the First Yield Line

Research results revealed three essential factors to obtain accurate results of a barrier's ultimate capacity via the proposed truss analogy. First, the analysis type must be nonlinear to consider the material nonlinearity of the truss elements and capture progressive failure due to yield

line formation. Therefore, the authors developed a Python script to read input files that contain nodes, members, boundary conditions, and a loading point. The script then solves the truss using the stiffness method. The load was applied incrementally using small steps, and all the members were checked for yielding at each load increment. Yielded members exhibited an updated stiffness that was used for the truss global stiffness matrix in the next loading step.

Second, the angle of the first yield line (red line in Figure 3.8) varied when determining the critical angle of inclination that gives the least ultimate load. This variation was due to changing distances between the vertical frames of the truss. However, varying this distance changed the configuration of the actual barrier, so the stiffness of the vertical members was multiplied by a factor equal to the new spacing divided by the original spacing to maintain the same stiffness distribution of the original barrier model. This factor was sufficient to produce equivalent truss since the member length and orientation were not affected by the angle variation.

Finally, sizing the diagonal members is a crucial step that affects the results of ultimate capacity. The recommended approach to size diagonal members starts with an area equal to the vertical or longitudinal members and then analyzes one loading step while the structure is still elastic to proportion the magnitude of the load in a diagonal member with respect to longitudinal and vertical members that form a joint along the yield line. Then the stresses are calculated in the vertical and longitudinal members and scaled up to the yielding stress level. After applying Mohr's circle for the two normal stresses and rotating the angle to the desired diagonal orientation, Equations 3.29–3.31 were used to find the stress at the diagonal orientation. The obtained diagonal stress should be scaled up to the yielding stress by reducing the initial area of the diagonal. For more accuracy, the elastic analysis can be repeated with the updated reduced diagonal area, the stress calculations can be repeated, and the diagonal area reduction ratio can be obtained until no change in this ratio is observed.

$$\boldsymbol{R = \frac{\sigma_{vertical} - \sigma_{longitudinal}}{2}}$$

Equation 3.29

$$\boldsymbol{C = \frac{\sigma_{vertical} + \sigma_{longitudinal}}{2}}$$

Equation 3.30

$$\sigma_{diagonal} = R + C \times cos\, 2\alpha$$

Equation 3.31

In Equations 3.29–3.31, α is the angle of the desired orientation from the longitudinal direction.

The following section presents a case study that applied the current AASHTO procedure of YLA, the detailed YLA from Section 3.2, and the truss analogy model presented in Section 3.3. The solution was verified against numerical analysis of the barrier using Abaqus.

3.4 Case Study

The geometry of the Jersey-shaped barrier shown in Figure 3.1 was simplified by merging zones 2 and 3. The design of the barrier was provided by the Kansas Department of Transportation (KDOT), and the dimensions and reinforcement details are shown in Figure 3.9. The concrete compressive strength ($f'c$) was 4 ksi, and the steel yield stress (fy) was 60 ksi. Table 3.1 shows the concrete cover and rebar area information for the capacity calculations.

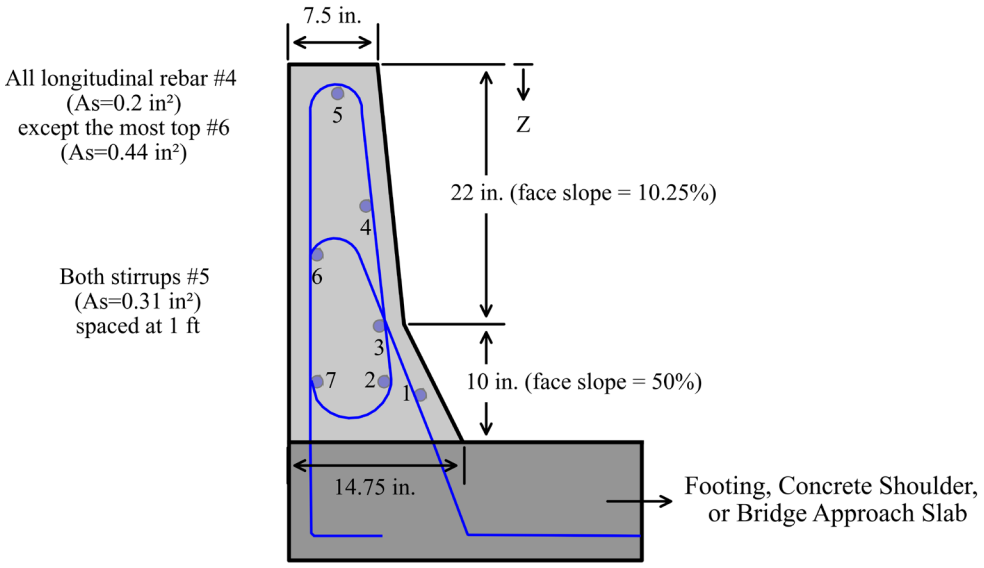

Figure 3.9: Case Study Jersey-Shaped Barrier

Table 3.1: Rebar Layout in the Barrier

	Front Side					Back Side		
Bar Id (as in Figure 3.9)	1	2	3	4	5	5	6	7
Area, in^2	0.2	0.2	0.2	0.2	0.44	0.44	0.2)	0.2
Cover, in.	1.77	4.8	3	3	4.21	3.62	2.36	2.36

3.4.1 AASHTO YLA Procedure

Because the equations provided by AASHTO (2020) are in U.S. customary units, the calculations presented in this section are also in U.S. customary units. Neglecting the section reinforcement and considering the ultimate moment capacity as the capacity corresponding to the concrete rupture results in:

$$\boldsymbol{f_r = \frac{M_r \times c}{I_g}}$$

Equation 3.32

Where:

Mr = rupture moment,

c = centroid of the section, and

I_g = gross moment of inertia.

According to the ACI (2014), the rupture modulus is:

$$\boldsymbol{f_r = 7.5\,\lambda\sqrt{f'c}}$$

Equation 3.33

Where λ is 1 for normal weight concrete and *f'c* is the concrete compressive strength in psi.

Substituting the value of *f'c* as 4000 psi results in an *fr* value of 0.474 ksi. Calculation of the sectional capacity is given in Table A.1.

According to Table A13.2-1 in AASHTO (2020), the height of this barrier classifies as a TL-4 barrier, so loading was applied at a distributed distance of L_t = 3.5 ft. Substituting the values from Table A.1 in Equations 3.1 and 3.2 resulted in L_c = 9.39 ft and R_w = 56.2. According to AASHTO (2020), TL-4 barriers must resist a transverse load F_t of 54 kips, which this barrier

satisfies. However, as described in the following sections, that was not the actual capacity of this barrier.

3.4.2 Rigorous YLA

In this study, the barrier capacity was obtained using the detailed process described in Section 3.2. The procedure presented in Figure 3.3 was also followed to obtain the sectional flexural capacity. Two regions with different linear variations in terms of depth (z) were identified (Figure 3.9), so two sections were defined to find the flexural capacity around the vertical axis (z-axis) at the back and front sides. Also, there are three planes with distinct geometry and reinforcement (the top of the barrier, the point of slope discontinuity, and the base of the barrier). Therefore, the flexural capacity around the longitudinal axis (x-axis) was represented by the capacity of these planes and assumed to vary linearly in between the planes. Detailed calculations of these capacities are shown in Table A.2–A.5 and summarized in Equations 3.34–3.37.

$$\boldsymbol{M_{z\_back}(z)} = \begin{cases} \boldsymbol{6.723 + 0.1615\, z\ kips.\frac{in}{in}} & , \quad \boldsymbol{0 \le z \le 22} \\ \boldsymbol{18.14 - 0.7875\,(32 - z)\ kips.\frac{in}{in}}, & \boldsymbol{22 \le z \le 32} \end{cases}$$

Equation 3.34

$$\boldsymbol{M_{z\_front}(z)} = \begin{cases} \boldsymbol{8.447 + 0.2383\, z\ kips.\frac{in}{in}} & , \quad \boldsymbol{0 \le z \le 22} \\ \boldsymbol{25.325 - 1.1625\,(32 - z) kips.\frac{in}{in}} & , \quad \boldsymbol{22 \le z \le 32} \end{cases}$$

Equation 3.35

$$\boldsymbol{M_{x\_back}(z)} = \begin{cases} \boldsymbol{14.443 + 0.8517\, z\ kips.\frac{in}{in}} & , \quad \boldsymbol{0 \le z \le 22} \\ \boldsymbol{19.83 + 0.3353(32 - z)\ kips.\frac{in}{in}}, & \boldsymbol{22 \le z \le 32} \end{cases}$$

Equation 3.36

$$\boldsymbol{M_{x\_front}(z)} = \begin{cases} \boldsymbol{4.443 + 0.764\, z\ kips.\frac{in}{in}} & , \quad \boldsymbol{0 \le z \le 22} \\ \boldsymbol{17.487 + 0.3763\,(32 - z)\ kips.\frac{in}{in}}, & \boldsymbol{22 \le z \le 32} \end{cases}$$

Equation 3.37

Substituting the moment functions from Equations 3.34–3.37 into Equation 3.27 for the distributed load along L_t = 3.5 ft and into Equation 3.28 for a concentrated load at the middle of the barrier results in Equations 3.38 and 3.39, respectively.

$$W_t = \frac{48\,tan\,\alpha + 30\,cot\,\alpha}{42\left(1 - \frac{42\,tan\,\alpha}{4 \times 32}\right)}$$

Equation 3.38

$$F_t = 48\,tan\,\alpha + 30\,cot\,\alpha$$

Equation 3.39

Solving Equations 3.38 and 3.39 for a range of angles and extracting the minimum values (Figure 3.10), Equation 3.38 gives W_t = 3.119 kip/in., which, when multiplied by L_t = 42 in., results in a capacity *Ft* of 98 kips. The capacity *Ft* under the concentrated load (Equation 3.39) is 76 kips. Although the concentrated load does not represent the vehicular impact force on RC barriers, it allows a comparison when solving the case study using the truss analogy where loading is concentrated at the center-upper joint.

Figure 3.10 shows that the ultimate capacity of the barrier obtained using the analytical solution is about 80% and 40% more than the capacity obtained using the AASHTO YLA for the distributed and concentrated loading patterns respectively, potentially because the smaller region of the barrier resisted the concentrated load, causing a localized failure. In addition, the range of angles with almost the same barrier capacity was 25°–38° when the load pattern was distributed and 32°–45° under the concentrated load effect, indicating that the variation of yield line orientation within these ranges does not significantly influence the barrier's capacity, although it alters the range of *Lc*.

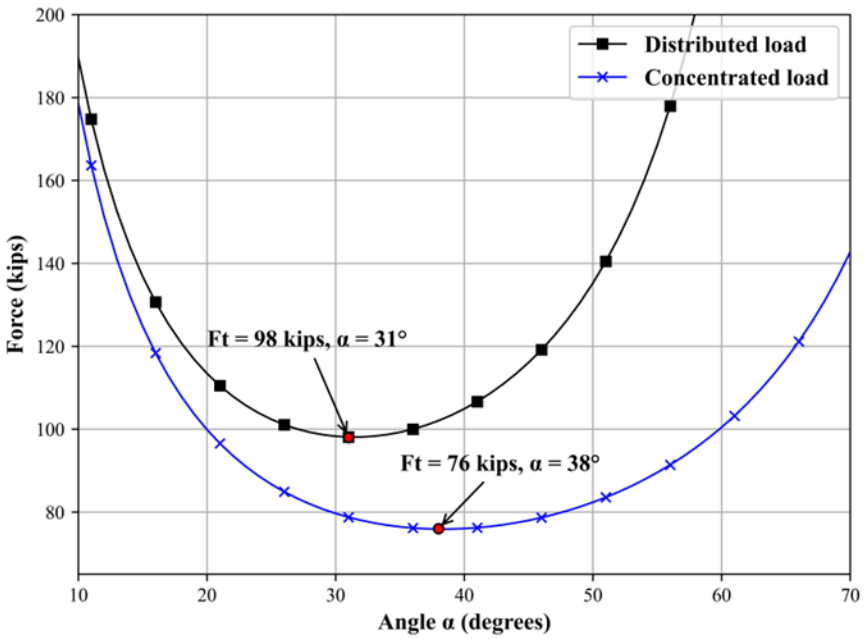

Figure 3.10: Critical Capacity Using the Analytical Model

3.4.3 Truss Analogy

This section models barrier reinforcement as an equivalent truss structure with a similar profile shape to the stirrup cage shown in Figure 3.11, with vertical elements having an area equal to the stirrup area 0.31 in^2 (200 mm^2), spaced at 1 ft (300 mm) (Figure 3.9), and the longitudinal elements with an area equal to the sum of all the front side bars divided by four—the number of vertical panels (1.24/4 = 0.31 in^2). The truss can be divided into more vertical panels along its height to yield more accurate results; however, as the number of elements increases, the analysis complexity increases. Elastic analysis under 0.25 kips load step with an initial diagonal size of 0.31 in^2 gave vertical and longitudinal stresses of 0.27 and -0.011 ksi, respectively. Scaling the higher value to the yielding stress of 60 ksi produced a scale factor of approximately 222 (60/0.27 = 222.2), meaning when the vertical member reaches the yielding stress of 60 ksi, the longitudinal member has 222 times the stress of -0.011, or -2.4 ksi. The negative value indicates that the member is under compression. Angle α can be found using the following equation:

$$\alpha = tan^{-1}\frac{7}{12} \approx 31°$$

Equation 3.40

Where 7 in. is the height of the first vertical panel (Figure 3.11) and 12 in. is the stirrup spacing.

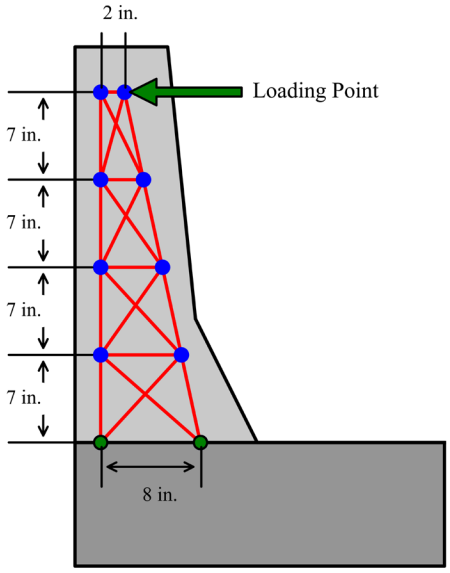

Figure 3.11: Model of the Barrier Reinforcement as Truss

Applying Equations 3.29–3.31 yields a diagonal stress of 43.5 ksi, as shown in Figure 3.12. Therefore, to cause yielding in a diagonal member when the vertical member begins to yield, the area of the diagonal member must be scaled down by a factor of (300/413 = 0.72), resulting in an adjusted diagonal area of ($0.72 \times 0.31 = 0.225$ in^2).

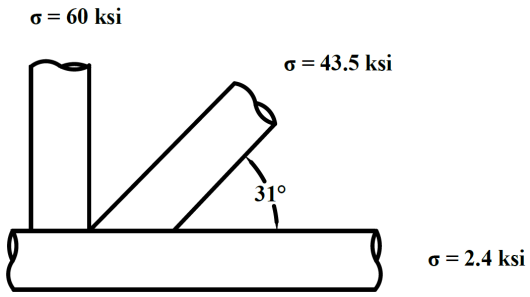

Figure 3.12: Mohr's Circle Stress Calculation to Size Diagonal Elements

Solving the truss using incremental loading of 0.25 kips for a range of α angles gives the critical load *Ft* (Figure 3.13), causing truss failure according to criteria in Section 3.3.2.

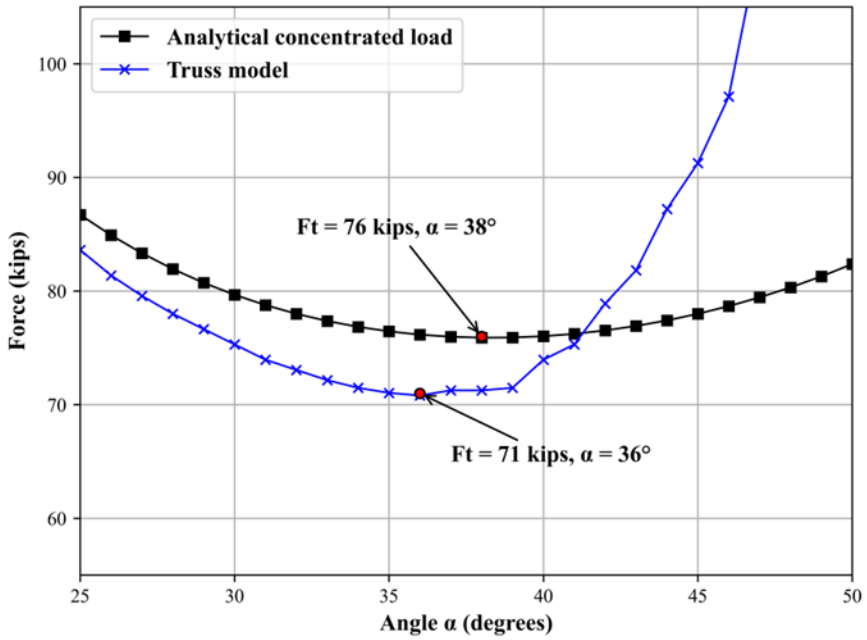

Figure 3.13: Critical Capacity Using the Truss Analogy Model

The results in Figure 3.13 show the efficiency of the proposed truss analogy model for predicting ultimate capacity and capturing barrier behavior. The analytical model of the concentrated load showed a similar loading pattern to the truss model, with differences at angles above 41° for the two models attributed to the discrete nature of the truss. The truss model predicted the barrier capacity as 71 kips compared to 76 kips predicted by the analytical model. Although the truss model is less conservative by approximately 7% of capacity increment, the concentrated loading pattern did not represent distributed vehicular loading, and the predicted value remained below the limit obtained by the analytical model of the distributed load (98 kips). In addition, the capacity increment of the truss model may be attributed to the diagonal members in the truss. Although these members stabilize the truss and prevent unstable failure mechanisms, they allow load transfer beyond the concrete resistance. Nevertheless, the results are promising for further refinement of the currently proposed model and procedure.

3.4.4 Finite Element Analysis by Abaqus

The final analysis method applied FEA using the implicit solver Abaqus. The model assembly consisted of the barrier (concrete) and the reinforcement (steel), shown in Figure 3.14, and the concrete material was modeled using the concrete damage plasticity model (Jankowiak & Łodygowski, 2005), as shown in Figure 3.15(a). The steel material was modeled bilinearly with a post-yielding modulus of 5% of the initial modulus, as shown in Figure 3.15(b). The concrete elements had solid sections with an 8-node linear brick element type (C3D8R). For the model mesh, the largest concrete element had dimensions of 2.4×2.4×1.6 inches (60×60×40 mm), totaling 5044 solid elements. The steel elements were modeled as beam elements with profiles corresponding to values in Table 3.1, and the barrier boundary conditions were fixed by restraining the translational degrees of freedom of the concrete elements at the base.

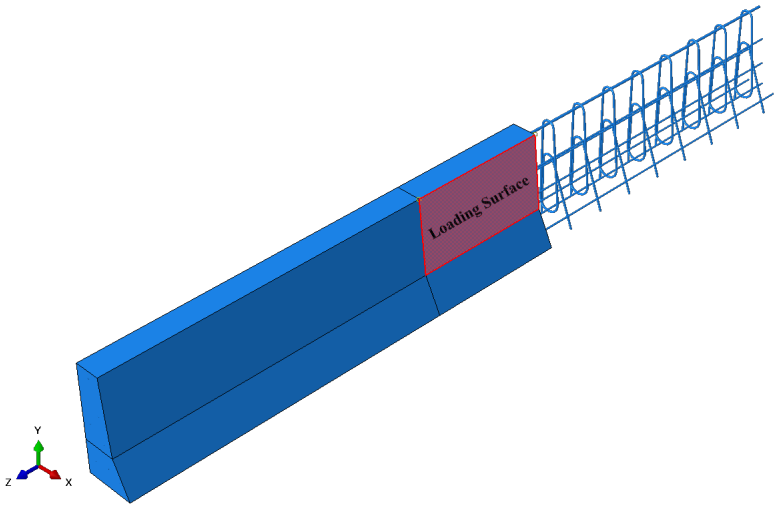

Figure 3.14: Abaqus FEA Model of the Case Study

The analysis was nonlinear static Riks with loading defined as a pressure applied at the loading surface (Figure 3.14). The loading surface represents the area that contacts an impacting vehicle in a real crash scenario. The surface length was 3.5 ft with a width that extended down until reaching discontinuity in barrier height (22 in.), and the target pressure was 250 psi, which is equvalent to a target load of 231 kips when considering the area of pressure application.

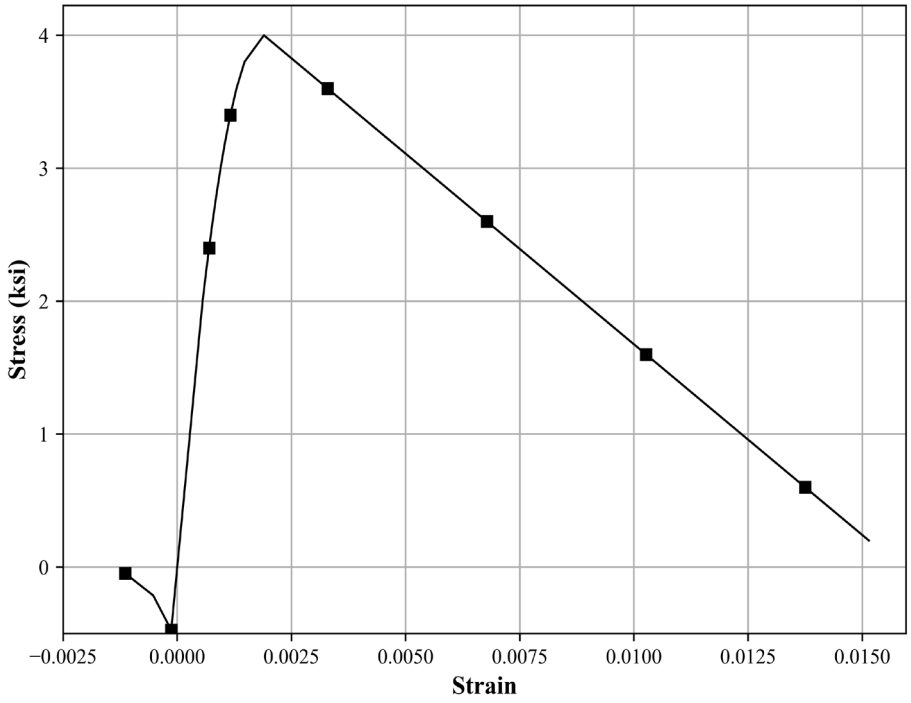

(a)

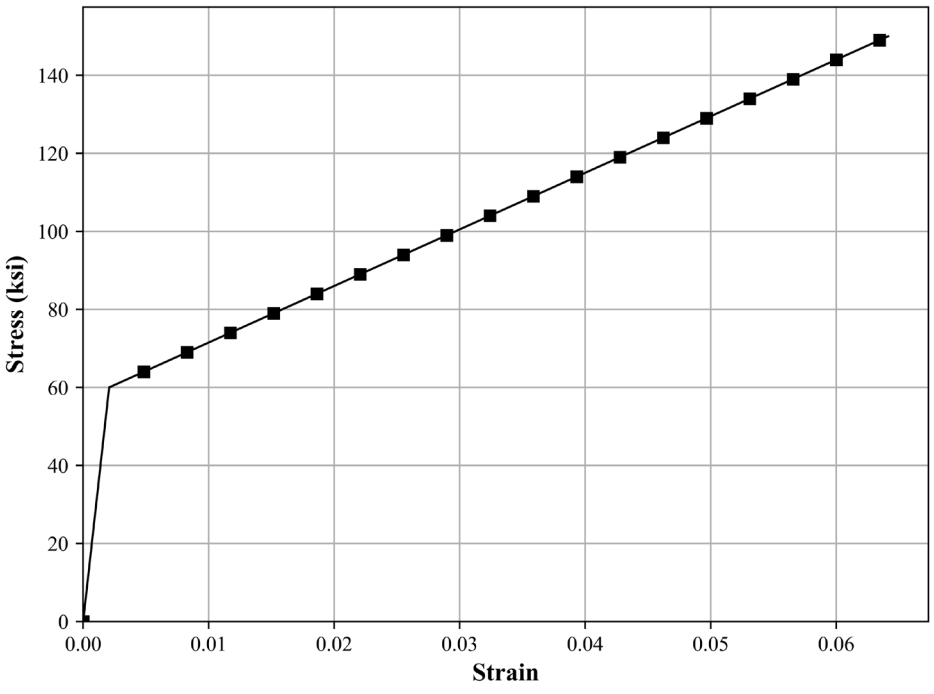

(b)

Figure 3.15: Material Models: (a) Concrete, (b) Steel

The analysis predicted a proportionality factor of 0.55 of the target load (231 kips), resulting in a peak capacity of 0.55×231 = 127 kips, as shown in Figure 3.16. This result is about 30% higher than the analytical solution for the distributed load shown in Figure 3.10 (98 kips). The reason for such a difference is attributed to the strain hardening in steel that was modeled in Abaqus which starts after a capacity of about 90 kips. The YLA assumes elastic-perfectly plastic behavior of steel. This behavior was not considered in the numerical modeling to avoid numerical instability in the solution. Excluding the strain hardening contribution, it can be shown that the FEA and the analytical YLA are in a very good agreement, 90 kips compared to 98 kips.

The displacement in Figure 3.16 was measured at a node at the middle-upper edge of the loading surface (middle of the barrier).

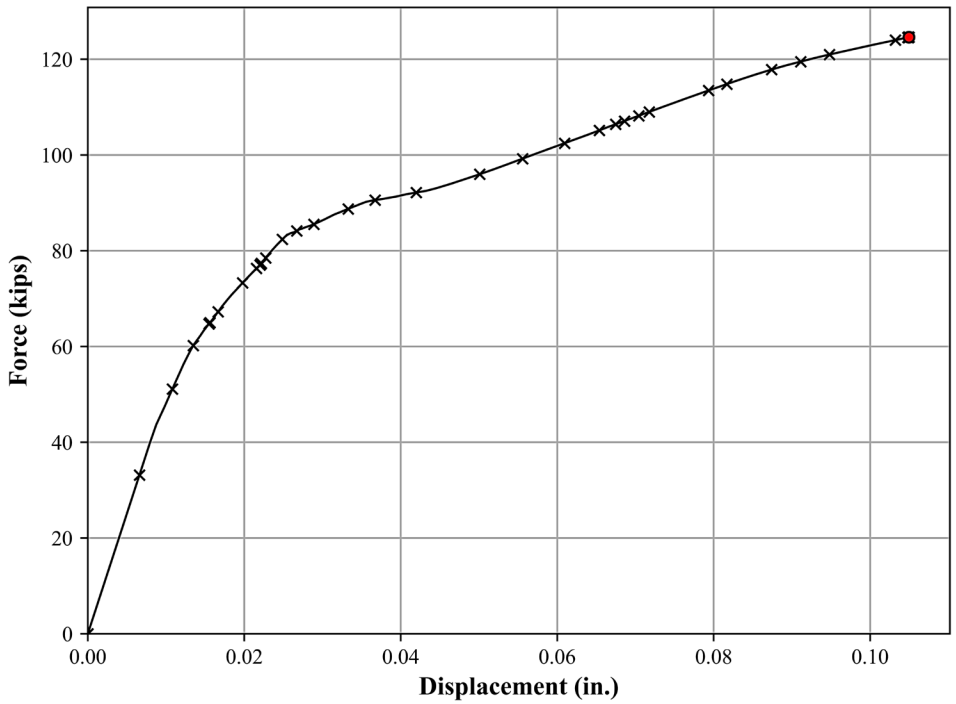

Figure 3.16: FEA Load-Displacement Response of the Barrier

Figure 3.17(a) shows the stress contour map of the barrier reinforcement at peak capacity; the figure legend displays psi units. The formation of yield lines is apparent in the figure when the points of highest stress in each stirrup connect. According to measurements in the figure, angle α

was calculated as 31°. Although the model shows that yielding occurred primarily in the vertical stirrups as in the truss analogy model, at ultimate capacity of the barrier, top segments of the stirrups did not reach complete yielding within the FEA model. This result could be due to complete failure of the concrete material, which prevented further load resistance, as shown in Figure 3.17(b). This result also justifies the lower capacity compared to the analytical solution of the distributed load (98 vs. 127 kips) since the analytical solution considers yielding of the entire line. The deformations shown in Figure 3.17 are magnified by 50.

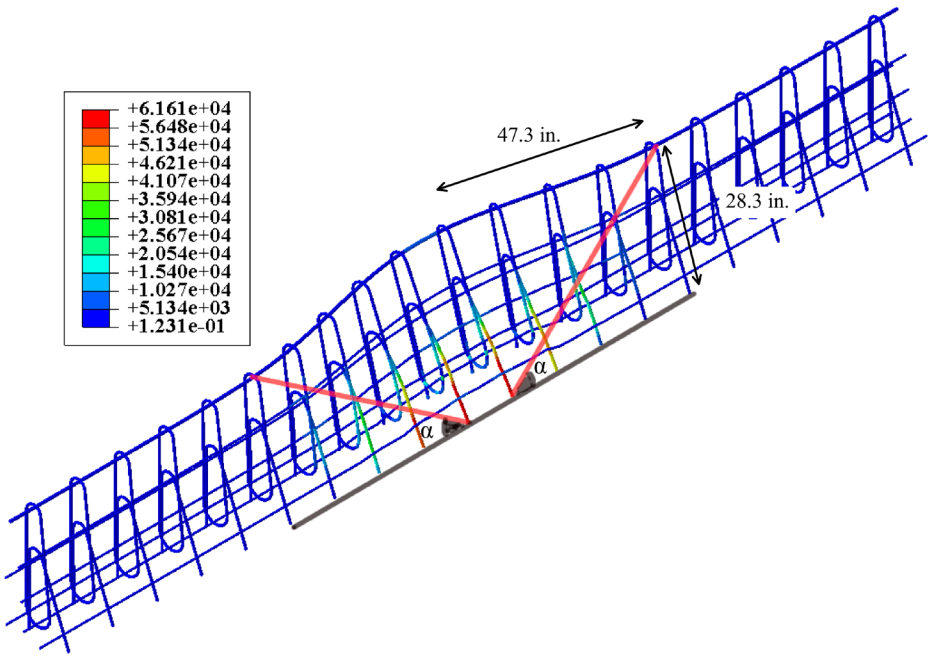

(a)

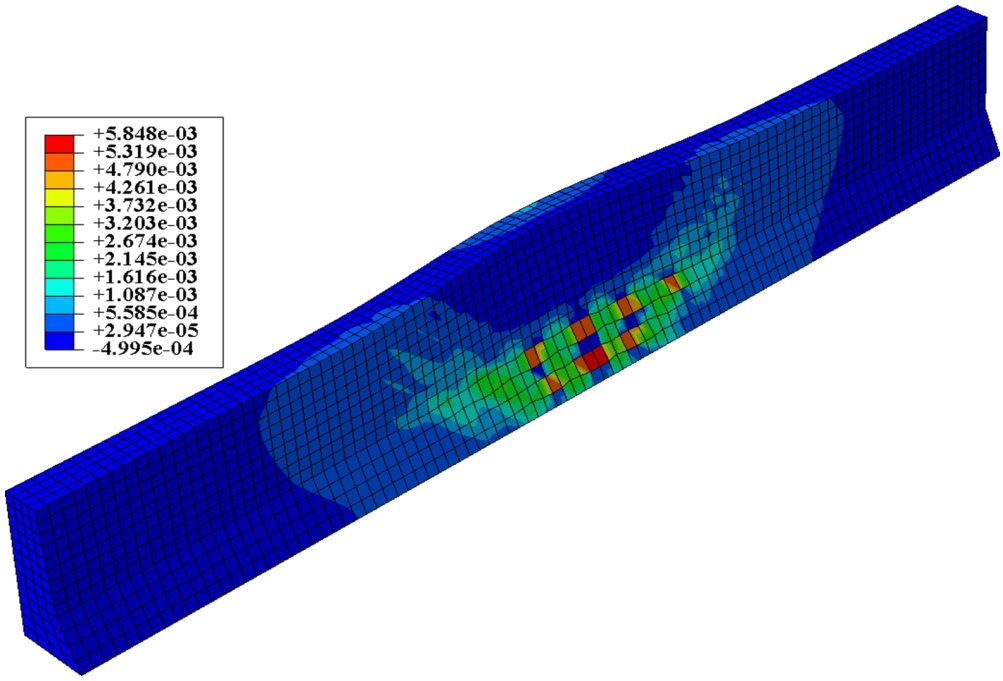

(b)

Figure 3.17: (a) Stress Profile in the Barrier Reinforcement; (b) Maximum Absolute Principal Strain in the Concrete

3.5 Conclusion and Recommendations

This chapter discussed the current AASHTO YLA procedure and the disadvantages of this procedure in terms of capacity underestimation. An alternative rigorous YLA methodology based on the V-shaped failure pattern was derived, and the procedure for implementing this methodology was explained. Furthermore, an innovative truss analogy model was proposed as a new technique for obtaining the transverse capacity of RC barriers by tracking the yielding of certain members along anticipated yield lines. To verify the presented methodologies, a case study of a Jersey-shaped RC barrier was analyzed for the ultimate transverse capacity, and a comparison of the obtained capacities was made, resulting in the following conclusions:

1. The current AASHTO YLA underestimated the barrier transverse capacity by more than 50% compared to the detailed YLA and the FEA.
2. The proposed YLA accurately obtained the barrier capacity under various transverse loading patterns with perfect agreement between the capacity obtained by this method and the FEA.
3. The proposed truss analogy captured the ultimate resistance of the barrier when subjected to a transverse concentrated load with acceptable agreement to the analytical solution for the same loading pattern; only a slight overestimation of the capacity was observed. This model could be further refined to more accurately represent the barrier and potentially obtain the capacity under different loading patterns.
4. Based on results in this study, a distinction in the structural adequacy criterion should be made between the barrier load resistance and its geometrical adequacy for vehicle redirection for a specific TL.

Chapter 4: Assessment of Sub-Standard Concrete Barriers

Many concrete barriers currently used to protect bridge piers from colliding vehicles do not meet AAHSTO requirements of a minimum height of 42 in. and resistance to a TL-5 crash event. Although alone these sub-standard barriers inadequately protect bridge piers against VCF, recent research has proven that their intervention in vehicle-pier collisions helps reduce the severity of crash effects and subsequent VCF demand on bridge piers. Therefore, comprehensive understanding of the behavior of sub-standard barriers during high-level crash events is essential for guiding efficient, cost-effective upgrades to these barriers. This study investigated the behavior of a sub-standard barrier subjected to TL-4 and TL-5 collision events using a matrix of dynamic finite element simulations via the FEA program, LS-DYNA. The study considered various boundary conditions of the barrier, including energy dissipation, velocity reduction, contact force absorption, and lateral displacement. Results showed that the maximum energy dissipation and velocity reduction were 45% and 30%, respectively, and the highest contact force demand and maximum lateral displacement were 131 kips and 31 in., respectively.

4.1 Finite Element Modeling

4.1.1 Single-Unit Truck

The finite element model of the SUT vehicle used in this study, a Ford F800, is shown in Figure 4.1(a). The model was developed by the FHWA at the National Crash Analysis Center (NCAC) and downloaded from the National Transportation Research Center, Inc. (NTRCI, 2005). The model was modified to comply with current MASH specifications for TL-4, such as increasing the vehicle inertial weight from 17.5 to 22 kips and increasing the impact velocity from 50 to 56 mph. Additional mass was obtained via a ballast concealed within the cargo area directly behind the truck cab, as shown in Figure 4.1(b). The height of the center of gravity (CG) of the ballast was 67 in. The modified model contained 154 parts, 35,000 deformable elements (96% shell elements), 2.5% solid elements, and approximately 1.5% beam elements. An accelerometer was located at the CG coordinates to measure kinetic properties of the vehicle during the crash.

Figure 4.1: (a) Ford F800 SUT Finite Element Model, (b) Added Mass in Cargo Area

4.1.2 Tractor Semi-Trailer

The TST finite element model used in this study was a simulation of a GMC 1991 truck used in Miele et al. (2010) and shown in Figure 4.2(a). The total inertial weight was 81 kips, including the added ballast shown in Figure 4.2(b) with a CG height of 6.4 ft (1950 mm). The only modification was the impact velocity, which was decreased from 52.8 to 50 mph to comply with current MASH TL-5 conditions. The model contained 583 parts, 375,540 deformable elements (80% shell elements), 20% solid elements, and a negligible percentage of beam elements. An accelerometer was placed at the CG coordinates to measure kinetic properties of the vehicle during the crash.

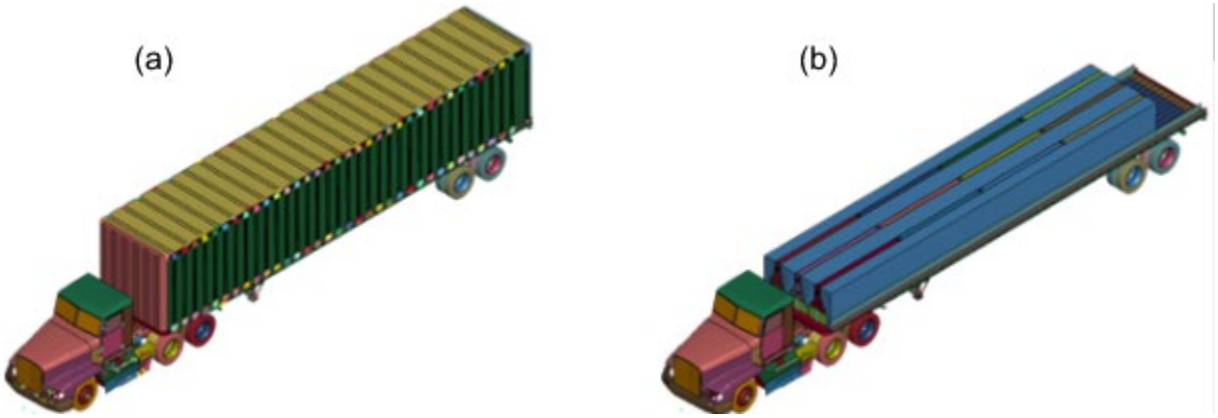

Figure 4.2: (a) GMC 1991 TST Finite Element Model, (b) Ballast Load

4.1.3 Sub-Standard Jersey-Shaped Barrier

KDOT provided the barrier model design used in this study (Figure 3.9). The barrier model contained a concrete parapet, transverse stirrups, and longitudinal bars. The parapet was modeled using a constant stress solid element section and the continuous surface cap model (CSCM) for the material (Livermore, 2017). The steel reinforcement was beam sections with Hughes-Liu element formulation and the piecewise linear plasticity material model (LS-DYNA MAT_024), and the reinforcement was constrained within the concrete using a Lagrange-in-solid constraint. The CSCM concrete material model considers strain rate effects.

A single concrete element was modeled and subjected to tensile and compressive displacement-controlled loading at different rates to validate the behavior of the concrete material model. The ratio of concrete dynamic strength to static strength was compared to experimental studies by Ross et al. (1995) for the tensile behavior and Bischoff and Perry (1995) for the compressive behavior. Results showed that the default values accurately capture the concrete response up to a rate of 1 strain per second, after which the model underestimates the concrete strength. Therefore, further calibration of tensile and compressive strain rate parameters (n_c and n_t) from LS-DYNA (Livermore, 2017) and Murray (2007) was necessary to adjust the behavior at high strain rates. The concrete stress strain curves generated at various strain rates are plotted in Figure 4.3(a) to illustrate the effect of the strain rate. Figure 4.3(b) shows that the two banded ranges from experimental scattered data points reported by Ross et al. (1995) and Bischoff and Perry (1995) enclosed the present tension and compression curves after calibration.

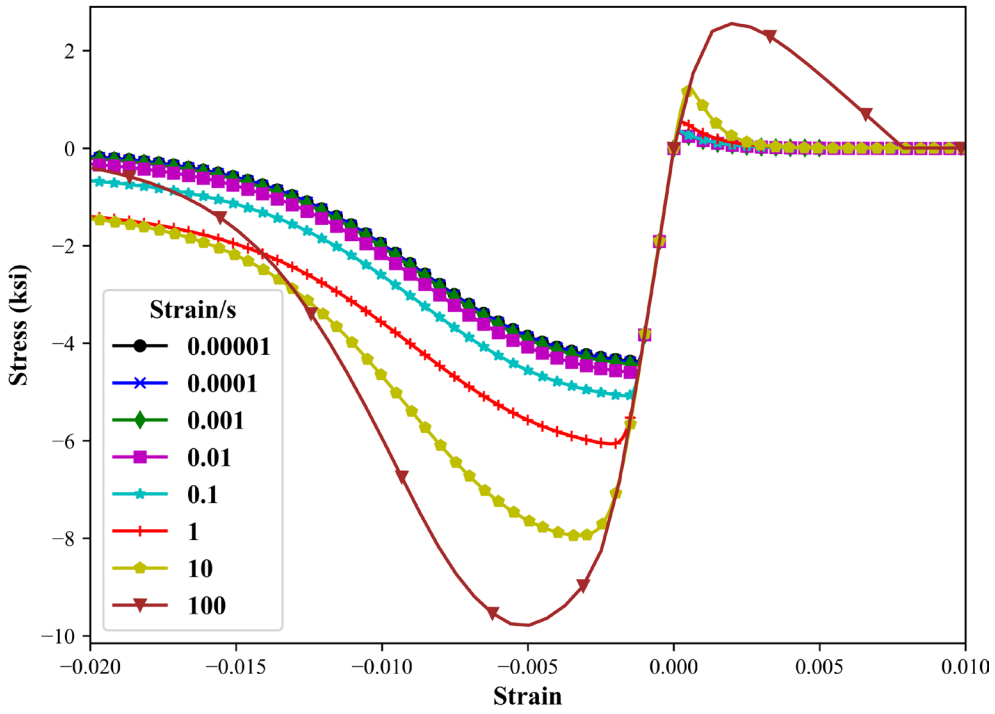

(a)

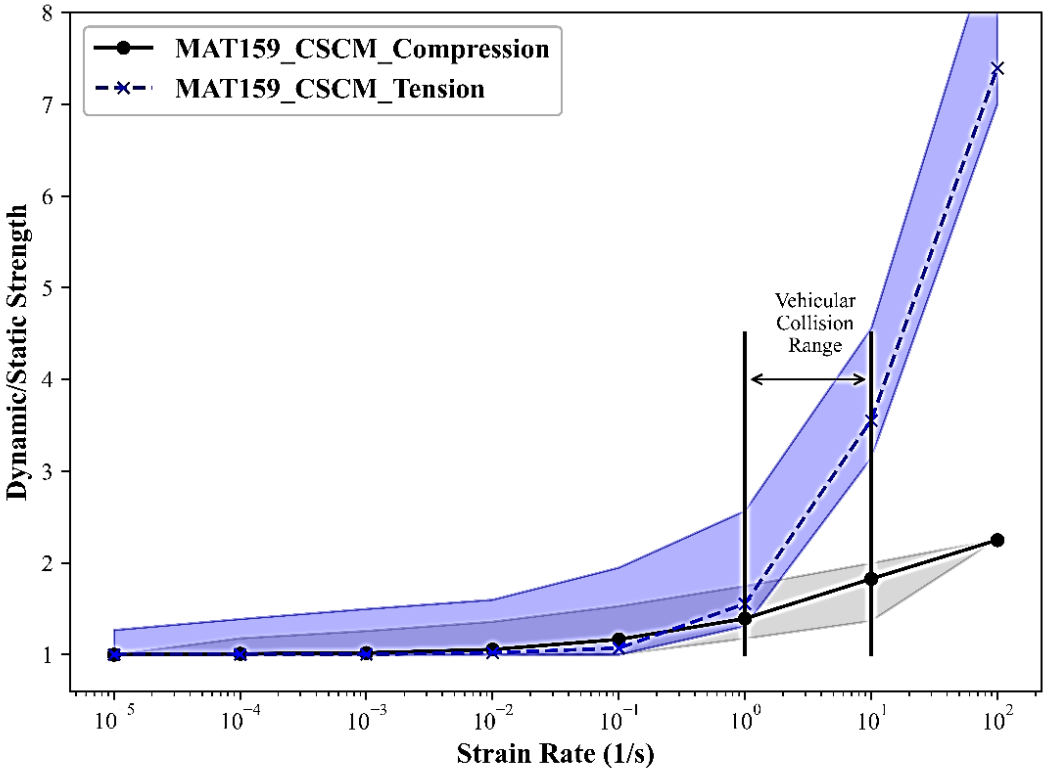

(b)

Figure 4.3: Concrete Material Model: (a) Strain Rate Effects, (b) Model Calibration for Strain Rate

This study also tested a steel coupon in tension to validate the steel material model. The resulting constitutive relationship was then idealized and used to simulate the coupon in LS-DYNA. Figure 4.4 shows that complete matching in the constitutive behavior was obtained, and Table 4.1 lists the properties of the barrier materials used in the LS-DYNA simulations.

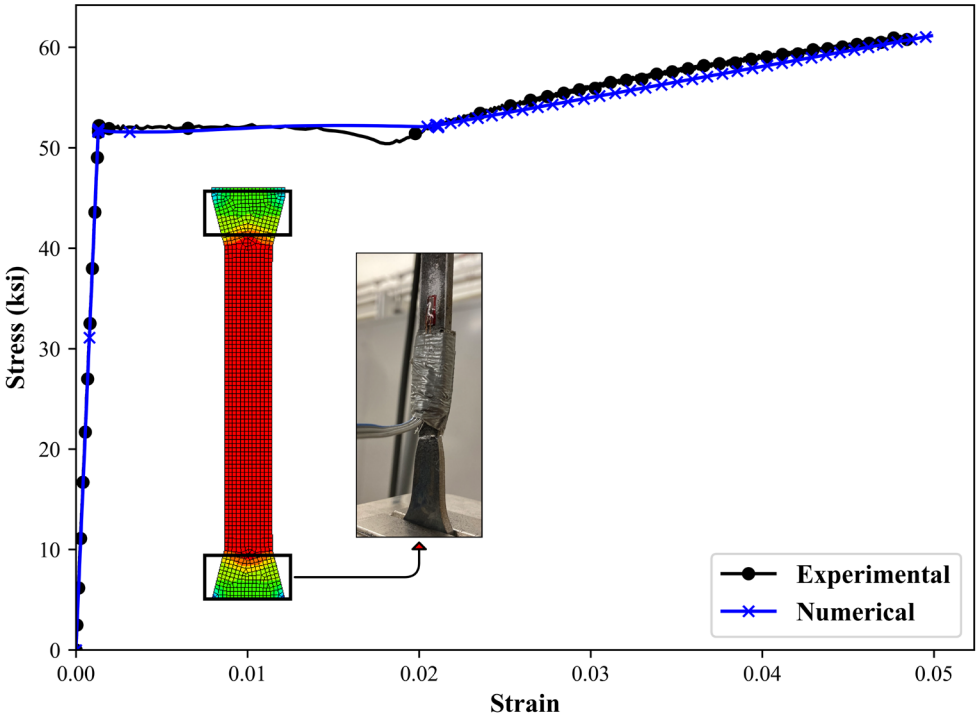

Figure 4.4: Validation of Steel Material

Table 4.1: Materials Properties

Properties	Concrete	Steel
LS-DYNA model	* MAT_159	* MAT_024
Density (lb/ft^3)	152	489
Elastic modulus (ksi)	3,626	30,000
Poisson's ratio	0.19	0.3
Compressive/Yield strength (ksi)	4	60

Two boundary conditions were considered for the barrier to cover possible construction scenarios. The fixed boundary condition was achieved by fixing all the degrees of freedom of the dowels at the pavement level, as shown in Figure 4.5(a), while the free boundary condition, which represents portable concrete barriers (PCBs), modeled the barrier as one continuous unit (Figure 4.5(b)) segmented into 12.5 ft (3.8 m) units (Figure 4.5(c)). Connection details between the segments for typical barriers in Kansas were provided by KDOT, and these connections were simulated by modeling rebar hooks with a rigid solid pin, as shown in Figure 4.5(c).

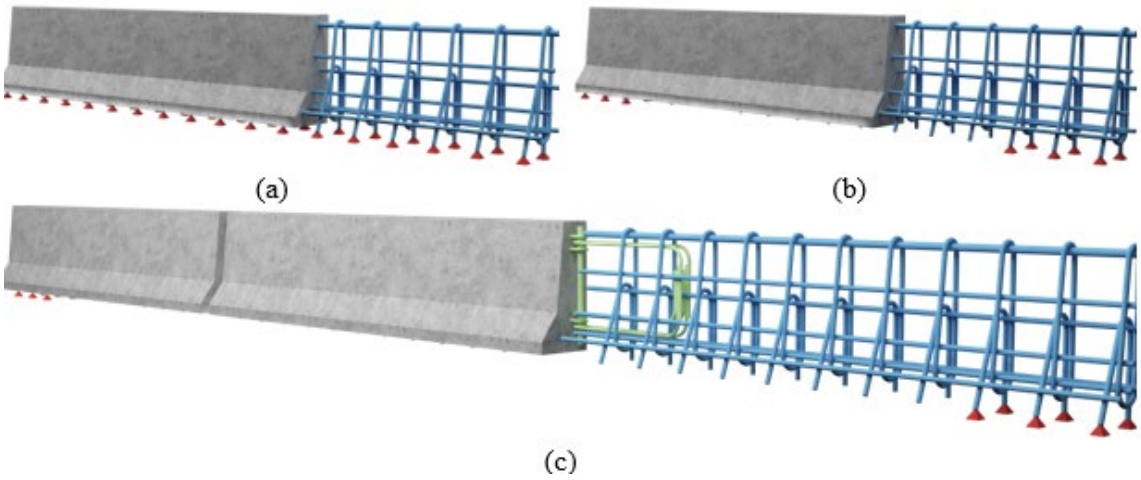

Figure 4.5: Modeling Barrier Boundary Condition: (a) Fixed, (b) Free, (c) Segmented

Pin-to-hook connectivity was accomplished using the CONSTRAINED_JOINT_ REVOLUTE option in LS-DYNA. Dowels measuring 3.25 ft from each end of the free barriers were fixed at the pavement level to provide edge anchorage, as in Rosenbaugh et al. (2007). The barrier was free to displace without friction between its bottom face and the ground to reflect the criticality of lateral displacement. The location of the first impact point between the vehicle and the barrier corresponded to the location of the critical impact point (CIP), or the location that maximizes the risk of barrier failure. The barrier length and CIP in this study were 148 ft and 24.6 ft, respectively, according to Sheikh et al. (2011). The segmented barrier was slightly longer than 148 ft due to the connection distance between the segments.

4.2 Model Validation and Solution Verification

The models were validated by comparing the results of the simulation to experimental testing results and existing simulations in the literature (model-to-model validation). FEA results were verified by examining the system energy balance and energy conservation.

4.2.1 Experimental-Numerical Validation

To verify the simulation reliability and validate the numerical model, the barrier used for the experimental crash event in Sheikh et al. (2011) was modeled and assigned the materials properties listed in Section 4.1.3. Figure 4.6 portrays the crash sequence at certain time steps (phenomenological events) for the Sheikh et al. (2011) study and the TL-4 model in this study.

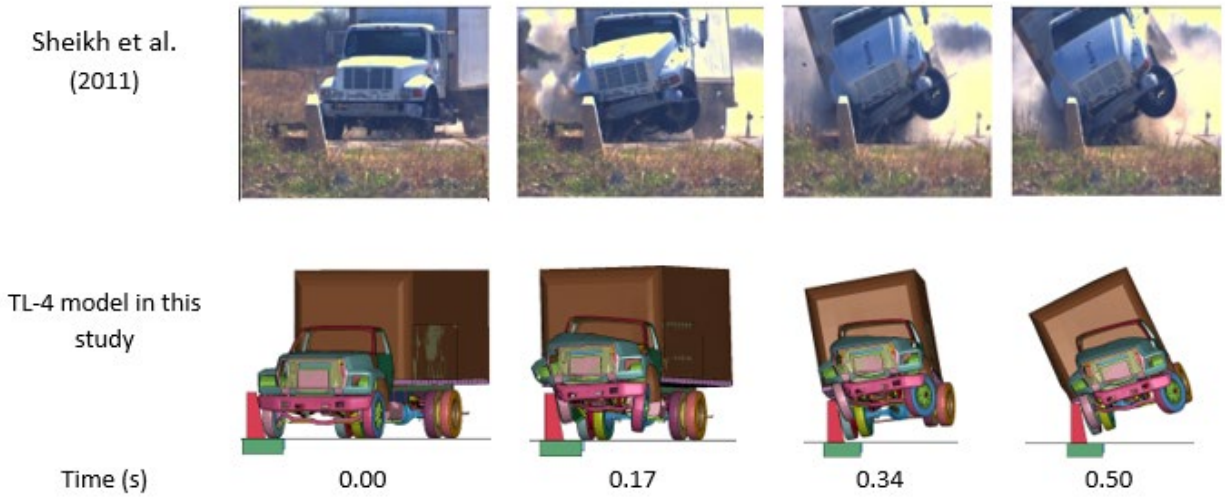

Figure 4.6: Comparison of Crash Simulation Sequence to Experimental TL-4 Crash

As shown in Figure 4.6, the vehicle behavior in this study was qualitatively identical to the experimental crash event at various time steps except that, in the experiment, the front wheel stayed in contact with the barrier due to high friction. This behavior was not fully captured in the present simulation. The friction value between the tires and the barrier was 0.75, as recommended by Trajkovski et al. (2018), and friction between the truck body and the barrier was 0.20, as in Cao et al. (2020). To further validate the simulation, the moving average acceleration of 50 ms at the CG reported in the experimental crash was plotted against the numerical simulation, as shown in Figure 4.7. Perfect matching was observed until the rear wheels hit, followed by a slight difference in the

recorded acceleration that may be attributed to the various characteristics of mass distribution in both vehicles. A model-to-model comparison was also made against numerical simulations of the experimental crash event by Cao et al. (2020). Notably, the vehicle mass in the Cao et al. (2020) simulation was not upgraded to meet current MASH requirements.

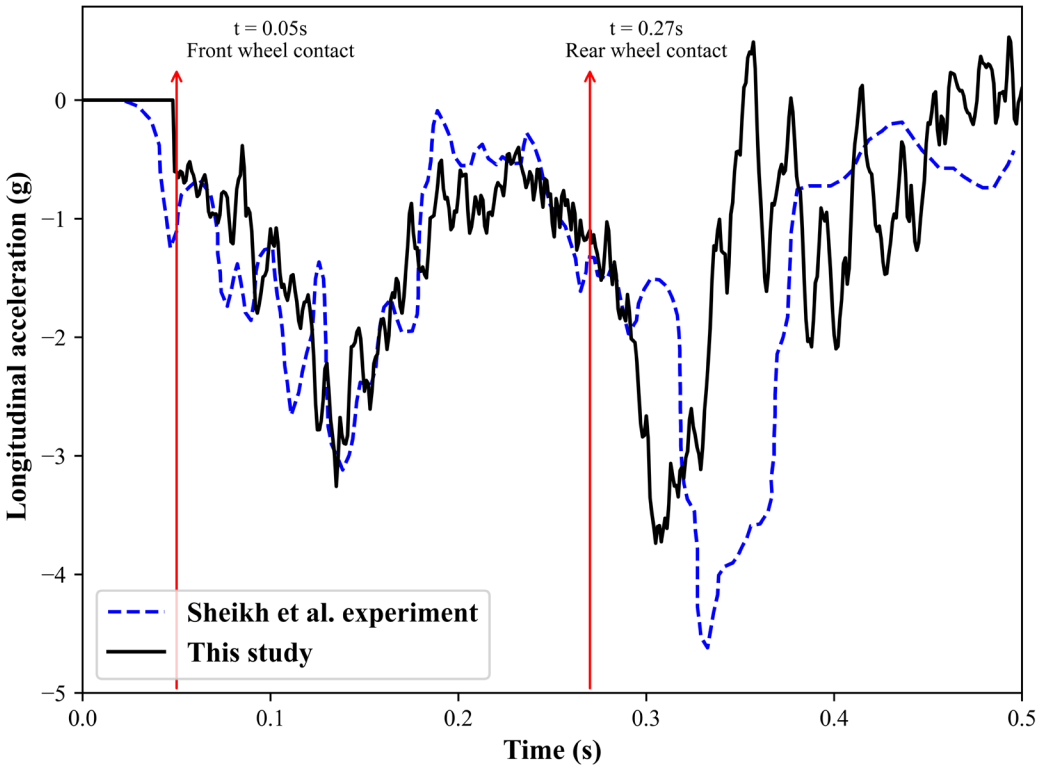

Figure 4.7: Acceleration Readings at CG

The contact force resulting from the impact between the vehicle and the barrier for the simulation is shown in Figure 4.8. The comparison in the figure shows high consistency at the beginning of the crash event when the bumper and the front wheels hit the barrier, followed by a difference in acceleration values and time of impact at the middle segment (time = 0.1–0.15 s) due to differences in vehicular mass. Results of this study demonstrated higher contact force with rear impact (approximately 700 kN compared to 500 kN in Cao et al. (2020)), or the contact between the cargo area and the barrier. This contact was avoided in the Cao et al. (2020) simulation due to lighter gravitational force, which allowed the cargo area to pass above the barrier. In general, this

simulation accurately captured the peak forces and overall crash behavior. This study also simulated the barrier under a TL-4 crash event, and the resulting barrier damage was compared to the experimental test for the same barrier, as reported by Bullard et al. (2010).

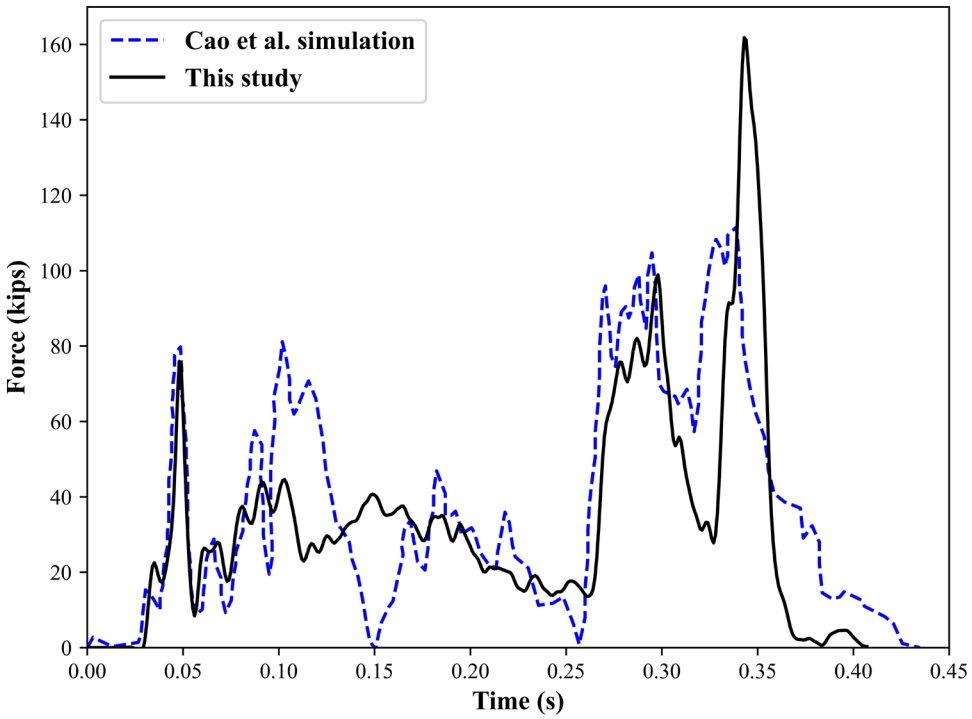

Figure 4.8: Comparison of Model-to-Model Contact Force Results

Damage on the simulated barrier was presented as effective plastic strain, or the plastic component of the rate of deformation tensor, in LS-DYNA, as shown in Figure 4.9. The results indicate high consistency in the damage locations throughout the barrier.

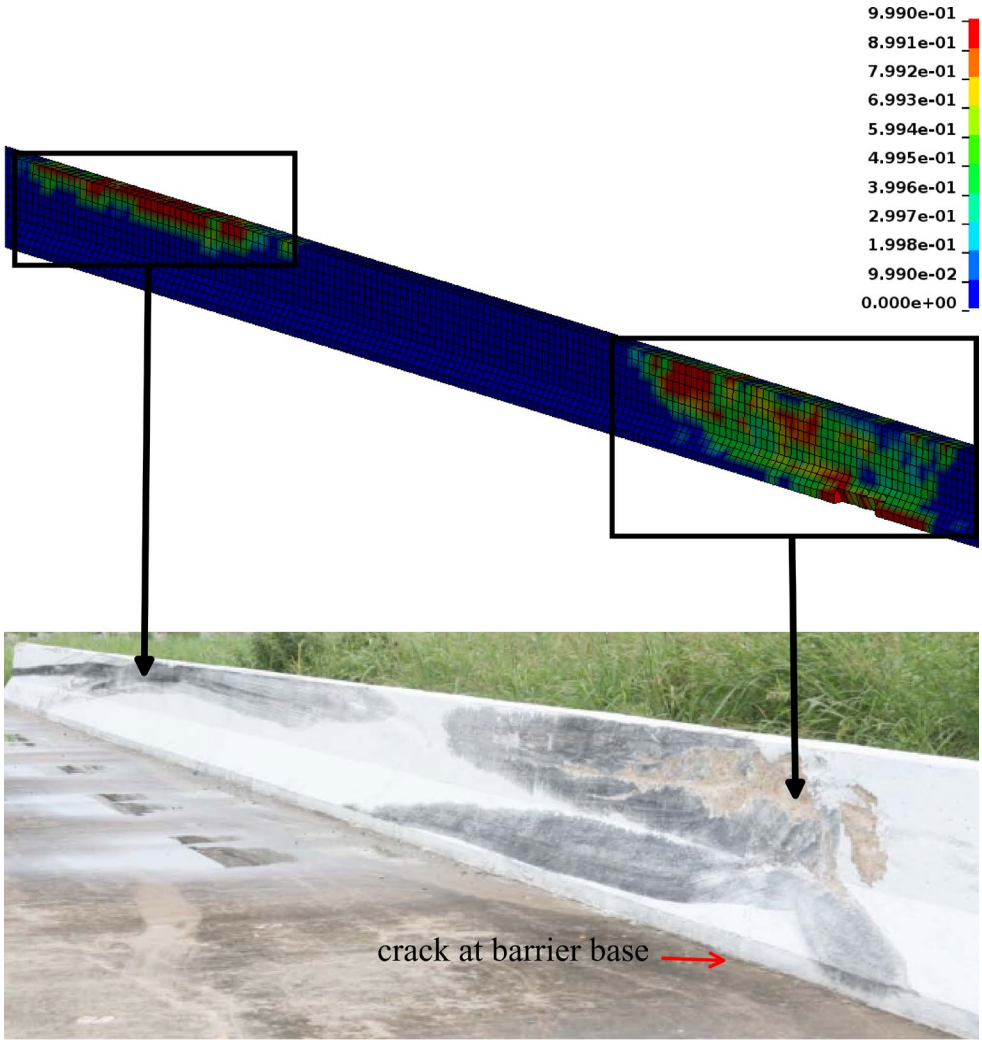

Figure 4.9: Experimental versus Numerical Damage in the Barrier
Source: Bullard et al. (2010)

4.2.2 Solution Verification

According to Consolazio et al. (2003), monitoring energy components is essential for identifying model errors and numerical defects in impact simulations. The energy monitoring used to verify this model verified energy conservation in the numerical simulation throughout the crash event. The total energy (TE) in a mechanical system exists as kinetic energy (KE), internal energy (IE), hourglass energy (HGE), damping energy (DE), sliding energy (SE), and rigid wall energy (RWE). At every time step during the event, the TE should be equal to the IE in the system (kinetic and/or internal) plus the external work (W). HGE is a fictitious form of energy that describes the energy consumed to distort the elements. The ratio of HGE to the TE indicates whether a

simulation is affected by artificial numerical effects; this ratio should be close to zero for an adequate mesh (Consolazio et al., 2003).

Equation 4.1 provides the energy conservation in a simulated system. Dividing the left-hand side of Equation 4.1 by its right-hand side gives the energy ratio, as shown in Equation 4.2. This ratio was near unity, indicating the conservation of energy throughout the simulated event.

$$\underbrace{KE + IE + HGE + DE + SE + RWE}_{Total\ Energy\ (TE)} = \underbrace{KE_{inititial} + IE_{initial}}_{Initial\ Energy} + \underbrace{W}_{External\ Work}$$

Equation 4.1

$$Energy\ ratio = \frac{Total\ Energy\ (TE)}{Initial\ Energy + External\ Work}$$

Equation 4.2

Figure 4.10(a) shows the conservation of various energy components in TL-4 simulations. As shown, the vehicle starts with a kinetic energy of $KE_{initial} = \frac{1}{2}mv^2 = 3.2$ Mega Joules (MJ), where m is the model mass 22 kips (10,000 kg) and v is the initial velocity 56 mph (25,000 mm/s), respectively. Once the impact event started, the KE transformed to IE, SE, and minimally HGE, DE, and RWE. Figure 4.10(b) shows an approximate 8% loss in the energy ratio at 0.3–0.4 s and then a return to ratio unity. This difference may be due to the high impact between the barrier and the rear wheels of the vehicle that occurred during this time interval. Since the performance of the sub-standard barrier was also evaluated under TL-5 crash events, model accuracy of the TL-5 crash event was essential.

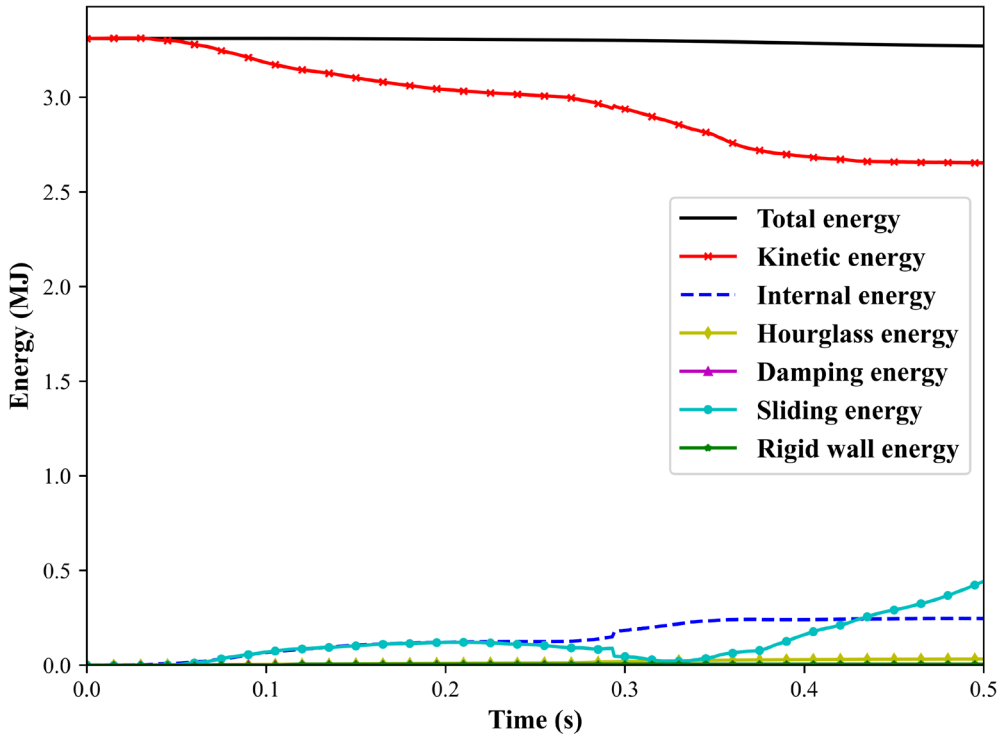

(a)

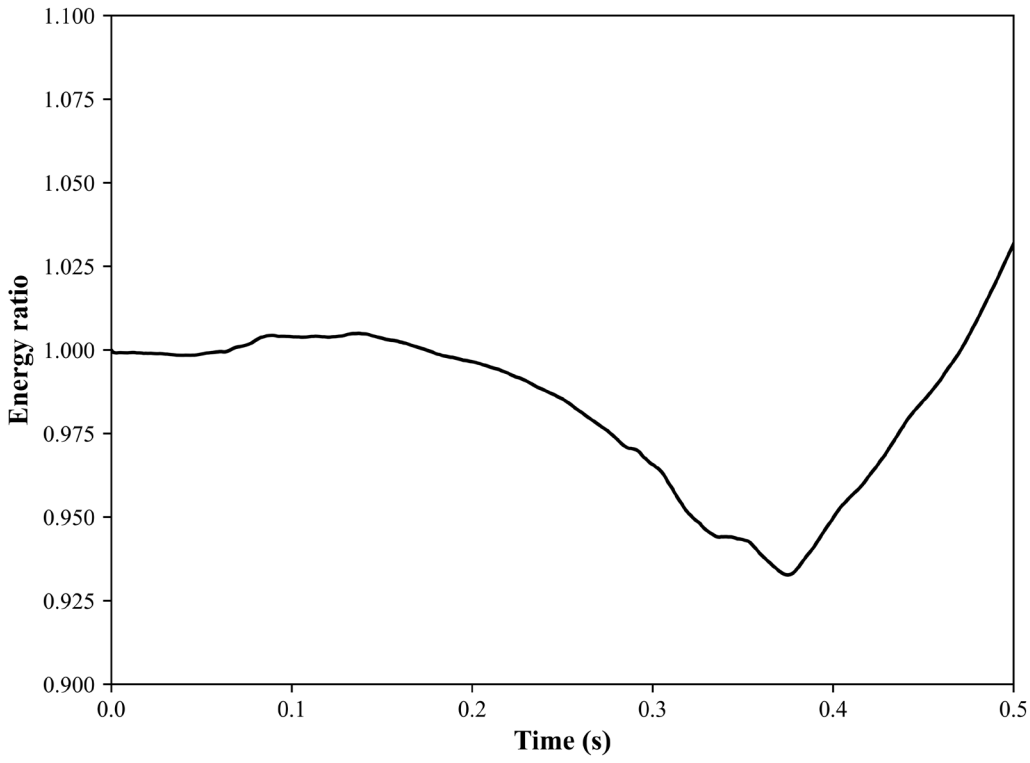

(b)

Figure 4.10: TL-4 Validation by Energy Balance: (a) Energy Components, (b) Energy Ratio

Figure 4.11(a) shows the conservation of energy components in a TL-5 simulation, where the initial kinetic energy is $KE_{initial} = \frac{1}{2}mv^2 = 9.1\ MJ$, m is the model mass 81 kips (36,700 kg), and v is the initial velocity 50 mph (22,250 mm/s), respectively. As shown in Figure 4.11(b), the energy ratio for the simulation was near unity throughout the crash event. Mass scaling was utilized to improve the overall time-step; this mass, which was reflected in the energy calculations, caused $KE_{initial}$ to be slightly higher than 3.2 and 9.1 MJ for TL-4 and TL-5, respectively. Finally, the ratio of HGE to TE in both events was less than 1%, which is a negligible value that proves the absence of numerical instabilities that may affect the results of this study.

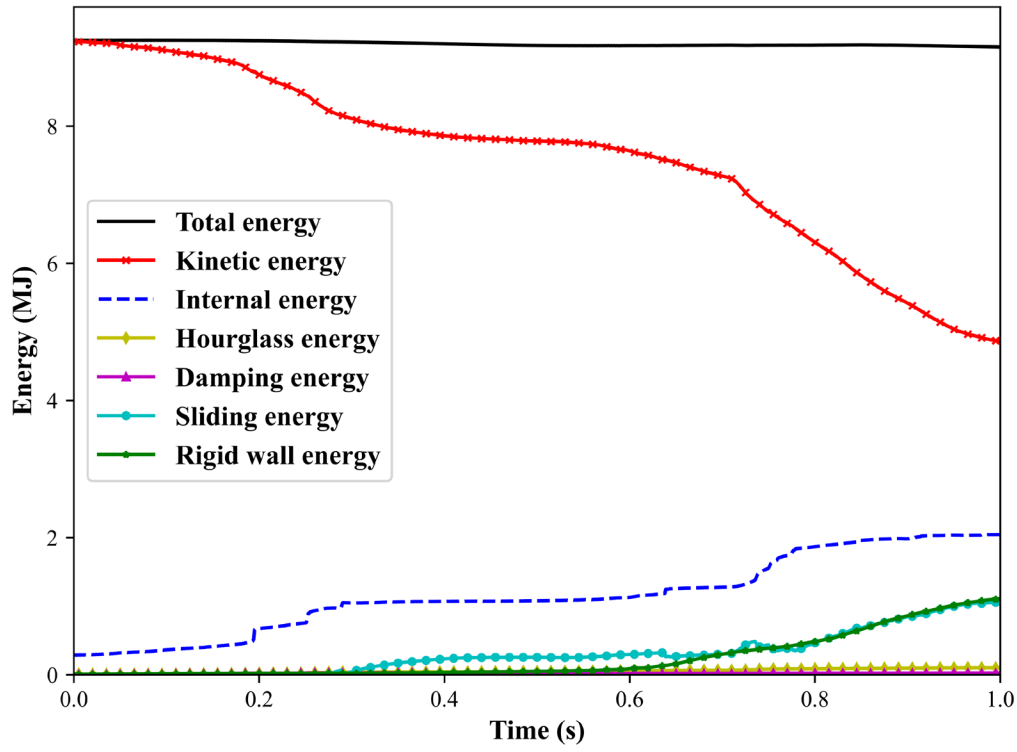

(a)

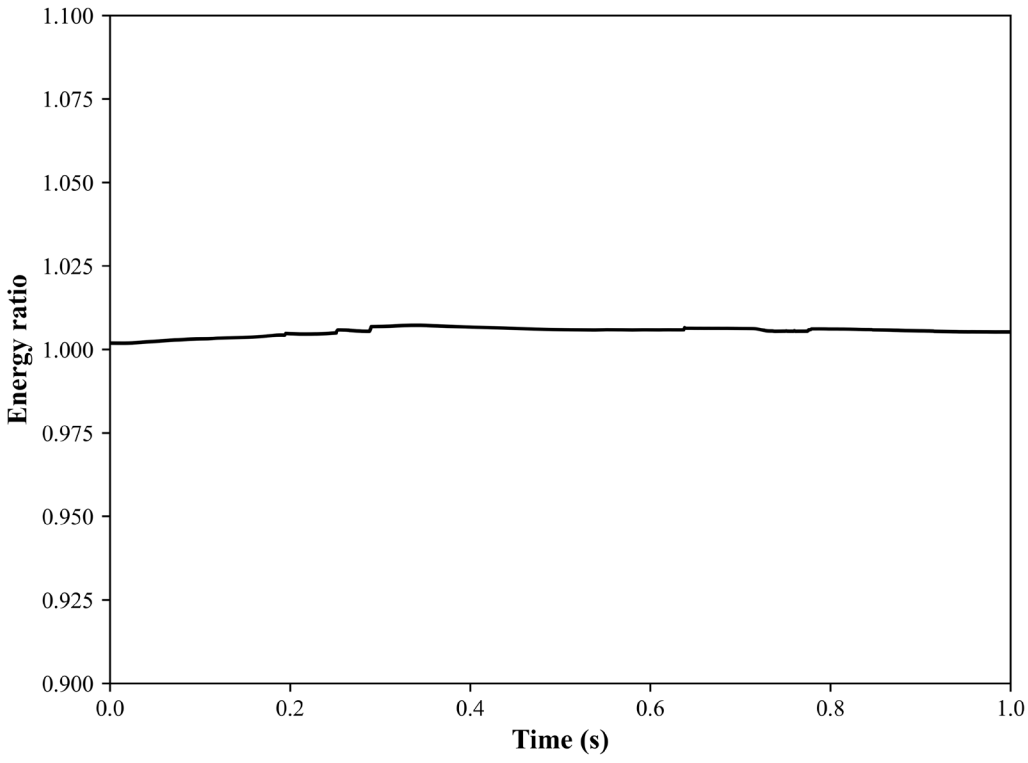

(b)

Figure 4.11: TL-5 Validation by Energy Balance: (a) Energy Components, (b) Energy Ratio

4.3 Analysis Results and Discussion

4.3.1 Energy Dissipation

Figures 4.12(a) and (b) show the performance of a sub-standard barrier for dissipating impact energy; thereby reducing the vehicle KE and developing IE during TL-4 and TL-5 crash events, respectively. For a TL-4 crash event, Figure 4.12(a) shows that the boundary condition only minimally affected the barrier's reduction of the KE. As shown, fixed and segmented barriers varied only slightly and reduced the KE by approximately 20% and 22.7%, respectively (approximately 3.3 to 2.65 and 3.3 to 2.55 MJ). Free barriers caused less reduction (approximately 16.4%, 3.3–2.77 MJ). The minimal KE reduction and slight difference between various boundary conditions may be due to decreased engagement of the barrier with the impacting vehicle. In other words, the vehicle body was small and traveled at high velocity, causing the vehicle to overturn and roll over the barrier before a complete barrier response was observed. Therefore, energy reduction primarily depends on the initial response of the barrier immediately after impact. Barrier behavior related to boundary conditions was observed in the TL-5 crash event, shown in Figure 4.12(b).

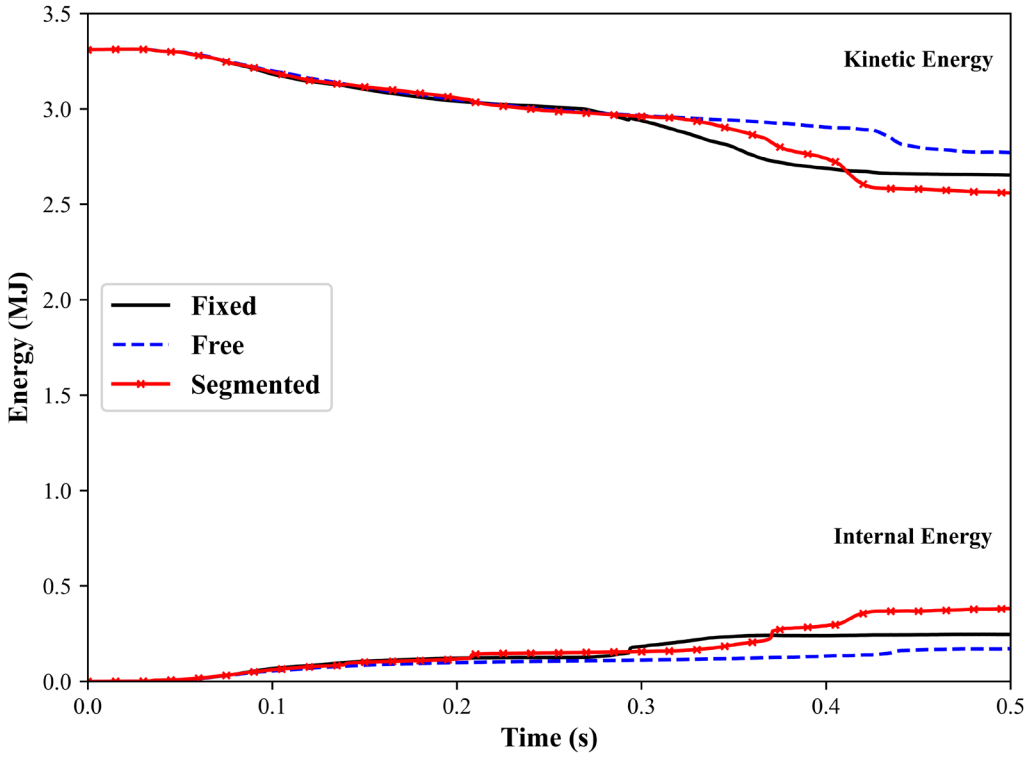

(a)

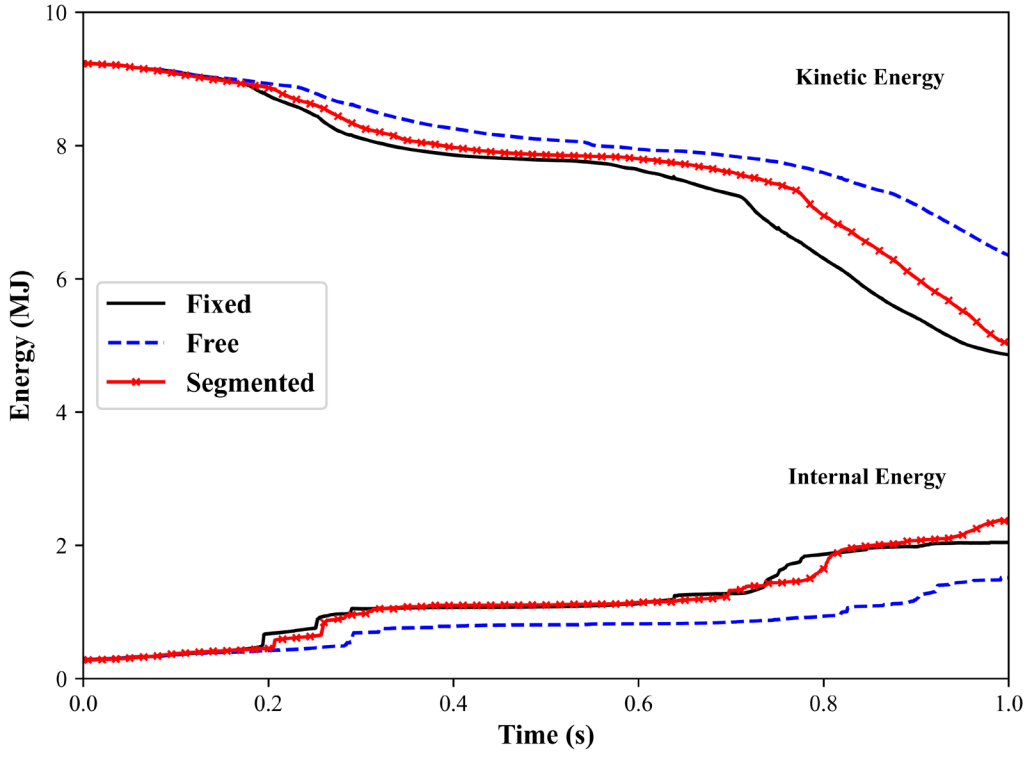

(b)

Figure 4:12: Dissipation of Impact Energy During (a) TL-4, (b) TL-5 Crash Events

Results showed that fixed and segmented barriers behaved similarly; both reduced the vehicle KE by approximately 45% (approximately 9.2–5.20 MJ) compared to approximately 30% for the free barrier. However, a higher percentage of KE reduction was associated with the TL-5 crash due to increased engagement of the barrier during the crash because the TL-5 vehicle was larger and traveled at less velocity. Finally, the free boundary condition in both test levels reduced the KE least, potentially due to the high deformability of the free barriers compared to the fixed barriers. Although segmented barriers share the deformability feature with free barriers, they have rigid connections between the segments that increase barrier stiffness and absorb more energy. All KE reductions were accompanied by increased IE as a form of energy conservation previously shown in Figure 4.10 and Figure 4.11.

4.3.2 Velocity and Acceleration Reduction

Figures 4.13(a) and (b) show the performance of the sub-standard barrier for reducing the vehicle's impact velocity during TL-4 and TL-5 crash events. Results showed that fixed and segmented barriers reduced the initial velocity by approximately 17% (56–46.6 mph), while free barriers caused a 14% reduction during the TL-4 event (Figure 4.13(a)). Conversely, the initial velocity decreased by approximately 30% (50–35 mph) for fixed and segmented barriers and approximately 22% by free barriers during the TL-5 event (Figure 4.13(b)). A similar trend was observed for energy dissipation due to stiffness from the dowels and side connections of fixed and segmented barriers, respectively. Because acceleration is the derivative of velocity, barrier reduction of vehicle acceleration reflected similar reduction behavior. Graphs showing such trends are not included for brevity.

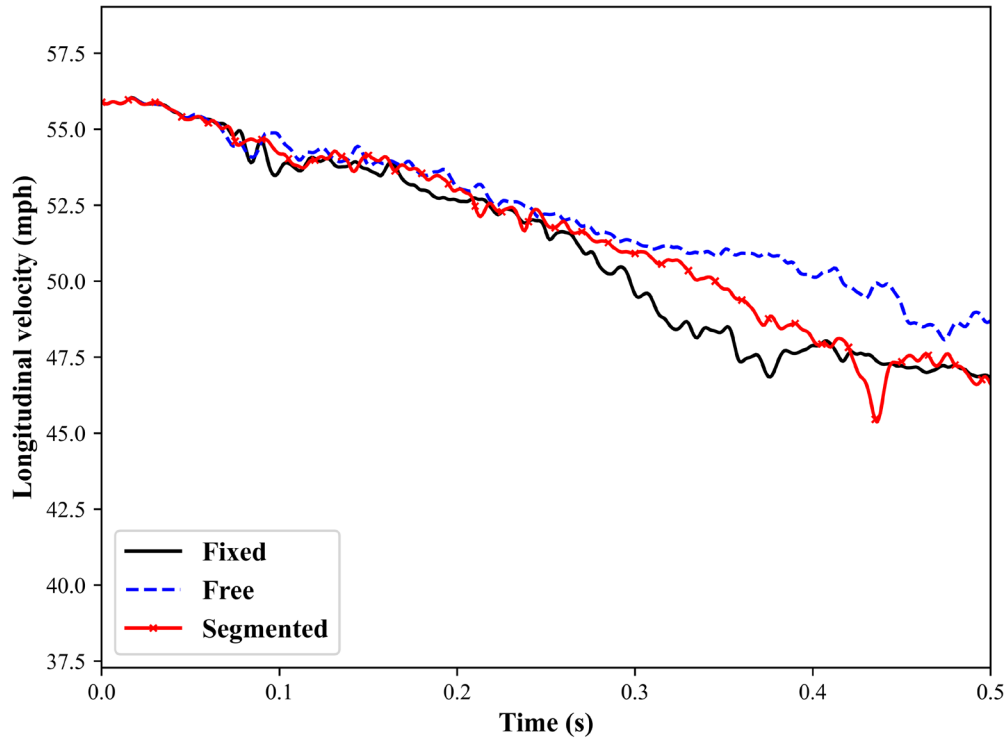

(a)

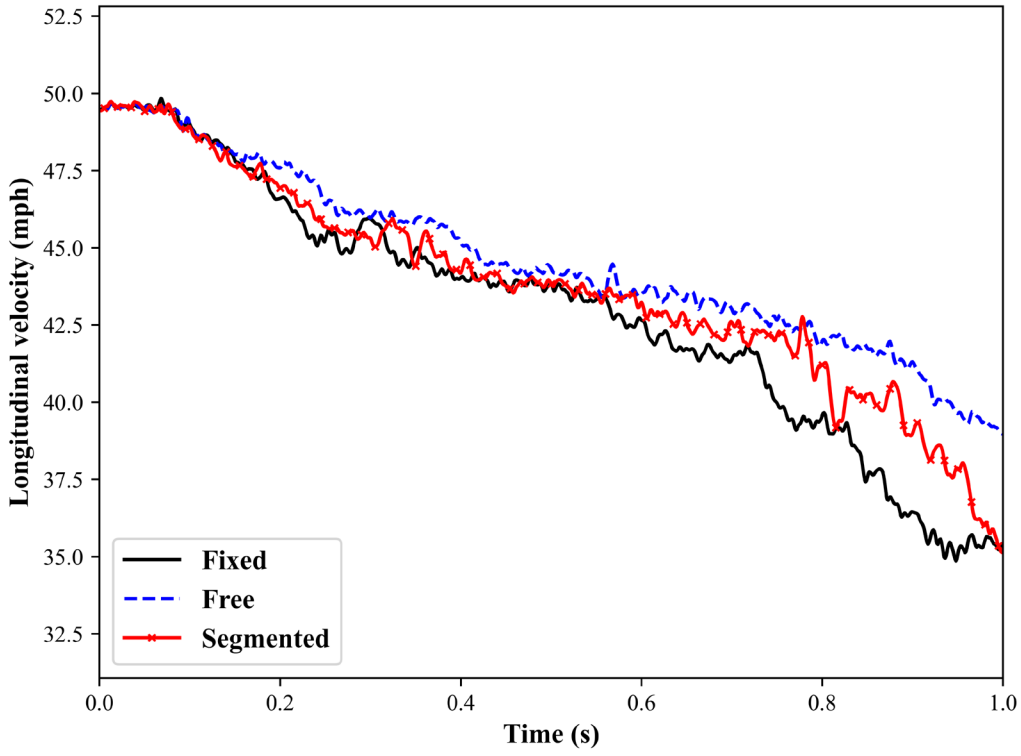

(b)

Figure 4.13: Impact Velocity Reduction During (a) TL-4, (b) TL-5 Crash Events

4.3.3 Lateral Displacement

The displacement history of each node at the upper back edge of the barrier was extracted, and the maximum displacement value for each node location was recorded to obtain the maximum displacement profile along the barrier. Negative displacements (toward the vehicle side) were neglected and recorded as zero. The reported locations of maximum displacement were associated with a CIP of 24.6 ft, as discussed in Section 4.1.3. Although the impact point in a real crash event is unpredictable, results of this study suggest that the location of maximum displacement along the barrier is relative to the CIP location. Therefore, engineers would benefit from knowing the possible location of maximum barrier lateral displacement along the barrier length with respect to the impact point, as shown in Figures 4.14–4.16, which prove that boundary condition significantly influences the maximum lateral displacement value and location.

As shown in Figure 4.14, the maximum lateral displacement for the fixed barrier was approximately 0.32 and 1.5 in. for TL-4 and TL-5 crashes, respectively, and the location of maximum lateral displacement was approximately 33 ft and 24 ft (11 and 8 m) from the edge of the barrier in TL-4 and TL-5 crashes, respectively (11.5 and 1.65 ft from the CIP location). For TL-4 crashes, the 36 ft location was affected by the first contact of the front bumper/wheel, followed by a similar peak when the rear wheels hit the barrier. For the TL-5 event, maximum displacement occurred at the 26 ft location due to rear wheel impact that occurred late in the crash.

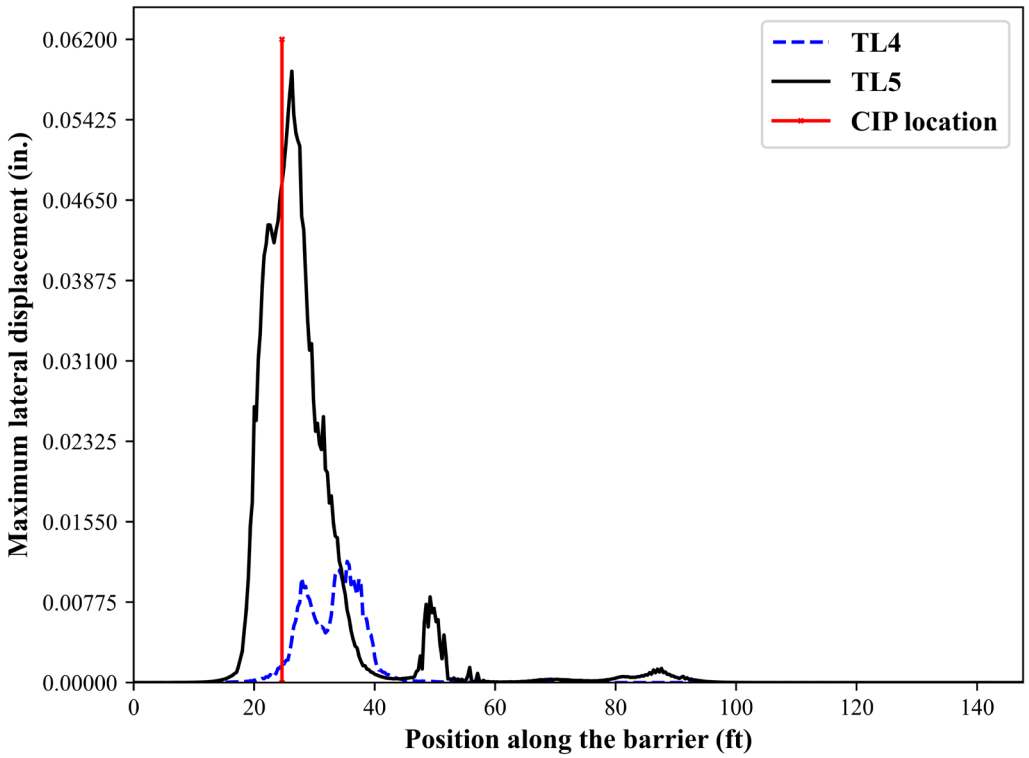

Figure 4.14: Lateral Displacement Profile along the Fixed Barrier

According to study results, free barriers experienced more lateral displacement than fixed barriers, with approximately 31.5 and 22.8 in. for TL-4 and TL-5 crashes, respectively, as shown in Figure 4.15. The location of maximum lateral displacement for both test levels was similar, with 36.4 and 37.7 ft (11.8 and 13 ft from the CIP) for TL-4 and TL-5 crashes, respectively. As expected, the nodal time histories showed that lateral displacement continued to increase as the crashing vehicle remained in contact with the barrier due to the free boundary condition that allows the barrier to deform.

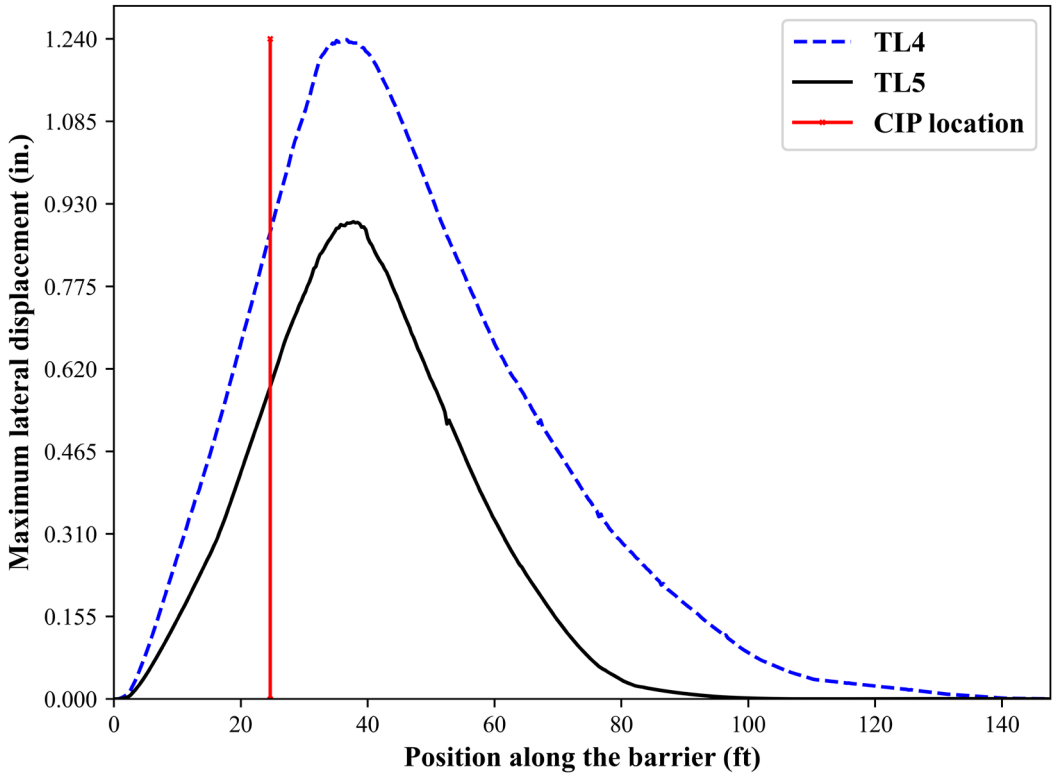

Figure 4.15: Lateral Displacement Profile along the Free Barrier

Lateral displacement results from the segmented barriers were between fixed and free barriers, with 15.7 and 11.8 in. for TL-4 and TL-5 crashes, respectively. The gridlines in Figure 4.16 represent the barrier segments. As shown in the figure, because the first segment included fixed dowels at the end of the segment, maximum displacement occurred at the beginning of the second segment (12.8 ft) during the TL-4 crash. Another peak occurred within the third segment due to the rear wheel hit, but this hit produced less displacement. The location of maximum lateral displacement was closer than the first impact point (12.8 ft compared to 26 ft) due to segmentation of the barrier, which allowed a door-like displacement mechanism at the first connection between segments. The same behavior was observed for the TL-5 crash event except for a significant rear wheel hit within the third segment (at 31.5 ft) that produced higher displacement than at the beginning of the second segment.

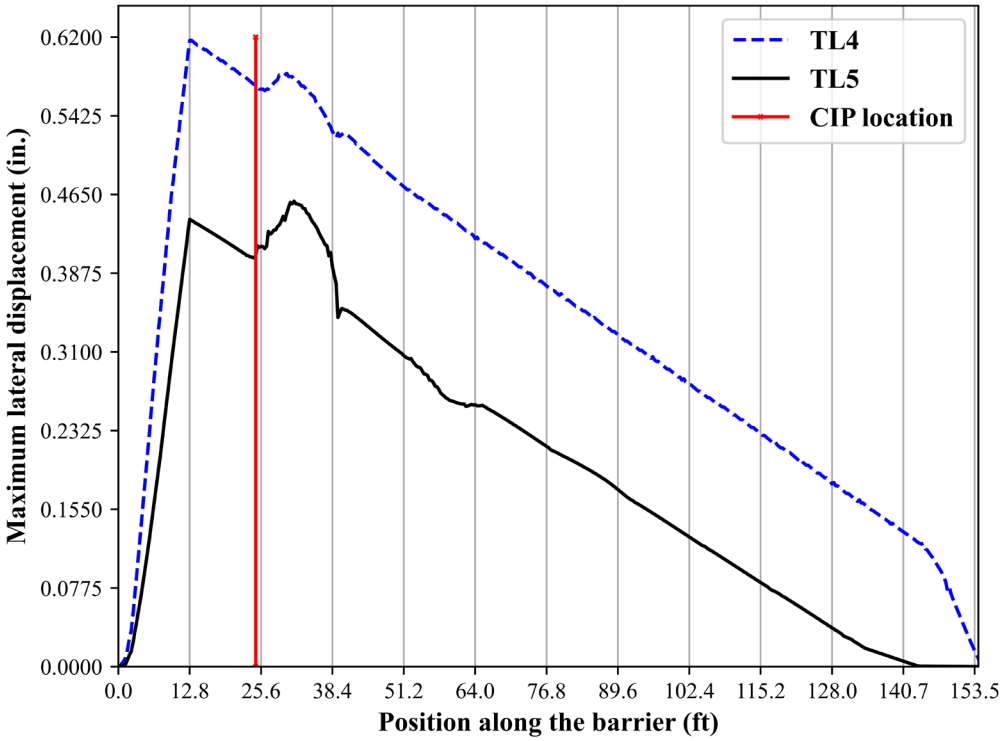

Figure 4.16: Lateral Displacement Profile Along the Segmented Barrier

The reported displacements were a result of a TL-4 crash event that lasted 0.5 s and a TL-5 event that lasted 1.0 s. Although longer simulations are informative, they are hard to achieve due to computational costs and model instability as the crash progresses. However, the selected durations were sufficient to extract the QoI in this study.

4.3.4 Contact Force

The barrier lateral contact force due to an impact event occurs perpendicular to the face of the barrier and is summed over all nodes involved in the contact. In other words, the barrier lateral contact force represents the force demand due to contact with an impacting vehicle. This analysis helps to quantify the VCF and design barriers that are structurally capable of meeting the required demand. AASHTO (2020) describes this force as the transverse force (F_t). However, the contact force described in this section is a result of dynamic simulations, while the design forces of traffic barriers in AASHTO (2020) are static forces. Previous studies such as El-Tawil et al. (2005), Zhou et al. (2017), and Roy et al. (2021) have estimated the ESF to represent the peak impact force

(PIF). The transverse VCF in this study was filtered using an SAE 60-Hz filter that removes force spikes that occur over a very short duration due to high-frequency numerical noise (SAE, 1995; Cao et al., 2020).

Figures 4.17(a) and (b) show the lateral contact force exerted on the sub-standard barrier during TL-4 and TL-5 crash events, respectively. Analysis of the contact force was categorized as two main events. The first event occurred when the front wheel/bumper hit the barrier, and the second event corresponded to the rear wheel hit. As shown in Figure 4.17(a), the boundary condition was minimally influential on the value of the force resulting from first contact during a TL-4 event. The barrier was subjected to 67.5, 57.3, and 66.3 kips in fixed, free, and segmented barriers, respectively. This slight difference was attributed to increased stiffness from the fixed barriers. Although the same results were expected for the second event, the deformability of the free and segmented barriers caused the vehicle to maintain lower elevation during impact, resulting in contact of the rear step bar and the barrier and a subsequent spike in contact force for the free and segmented boundary conditions. Figure 4.17(a) also shows increased deformation of the step bar in the segmented barrier compared to the fixed barrier, which caused the force spikes. Because this phenomenon is vehicle-dependent and may not occur with other crashing vehicles with identical inertial characteristics but higher CG, these spikes were reasonably excluded from the comparison. Therefore, the fixed and segmented barriers resulted in approximately the same contact force peaks of 69.7 kips, while the free barriers had contact force peaks of 33.72 kips.

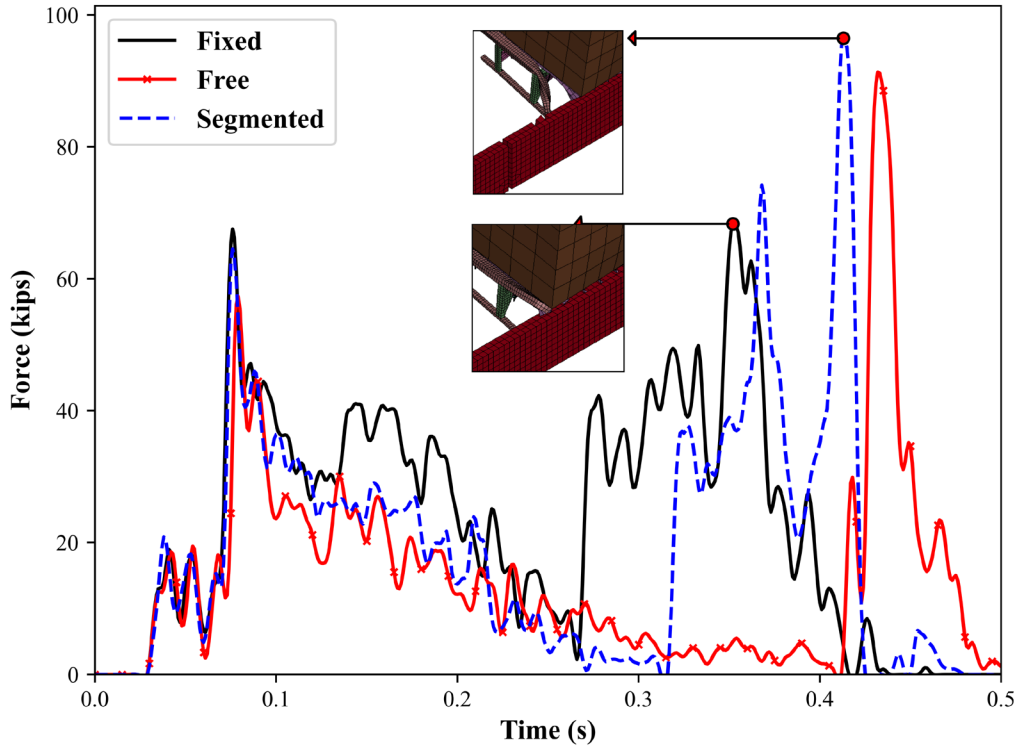

(a)

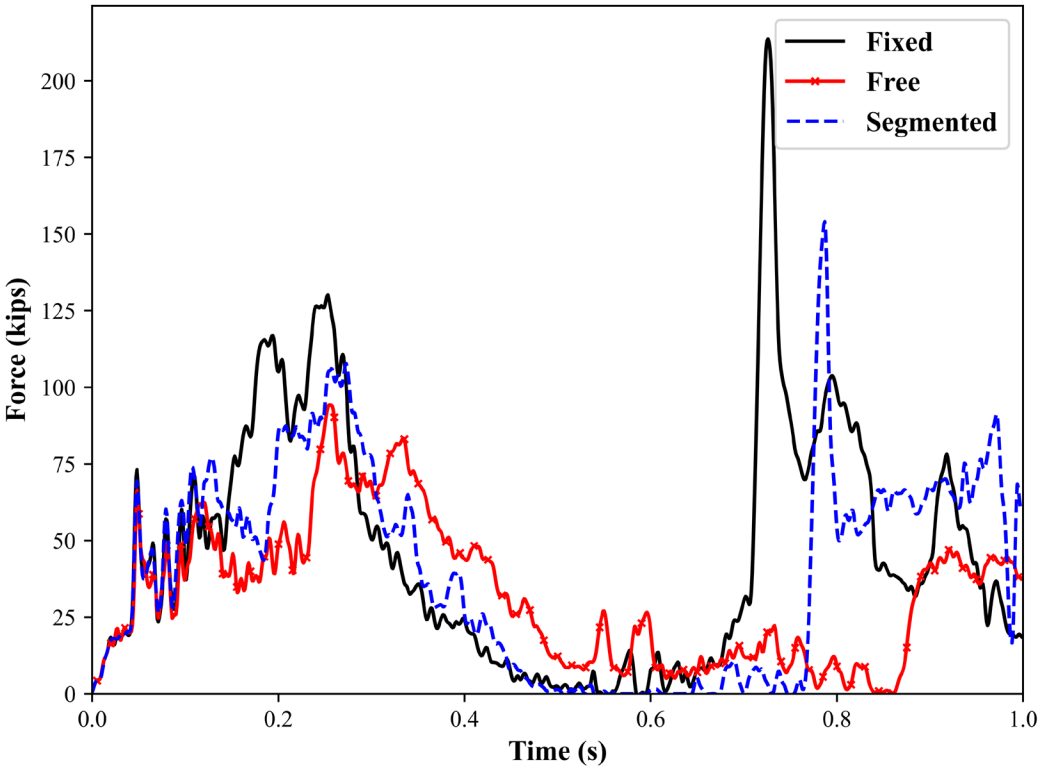

(b)

Figure 4.17: Lateral VCF During (a) TL-4, (b) TL-5 Crash Events

As shown in Figure 4.17(b), similar contact force behavior with different force magnitudes occurred in TL-5 crash events. Fixed, free, and segmented barriers were subjected to 130.4, 94.5, and 108 kips, respectively, during the first contact. Since the TST vehicle had higher CG elevation than the SUT, the second contact resulted in expected forces according to unique boundary conditions. Fixed, free, and segmented barriers experienced peak forces of 213.6, 47.2, and 154 kips, respectively, indicating the increased influence of the boundary condition for TL-5 crashes compared to TL-4 crashes. Finally, results showed that the more flexibility was available, the longer it took for the second impact event to occur for both test levels.

4.3.5 Structural Adequacy

The structural adequacy evaluation criteria summarized in MASH emphasize the ability of the test article (sub-standard barrier) to contain and redirect the vehicle or bring it to a controlled stop. Also, the impacting vehicle should not penetrate or override the installation with acceptable controlled lateral displacement in the test article. Simulations in this study showed that fixed, free, and segmented barriers subjected to TL-4 and TL-5 crash events redirected the impacting vehicle with no penetration but some overriding/rollover at later stages of the impact event. The lateral displacements were controlled for fixed barriers during a TL-4 crash, but excessive displacements were observed for all other cases. Therefore, determination of the effectiveness of sub-standard barriers to protect bridge piers depends primarily on the location of the pier behind the barrier. AASHTO (2020) specifies a minimum distance of 3.25 ft between the top edge of the traffic face of the barrier and the face of the protected pier, meaning that possible contact can occur between the cargo of the impacting vehicle and the pier when there is a tendency of overriding the barrier and the pier is close to the barrier. In addition, excessive displacements, especially in free boundary conditions, may reach the piers located behind the barrier, causing another source of loading due to contact with the deformed barrier. To further investigate the effectiveness of sub-standard barriers as protection for bridge piers against VCF, the next section presents a case study of a pier system subjected to a TL-4 crash event.

4.4 Case Study

This section compares the behavior of a sub-standard barrier to a standard barrier for a TL-4 crash event. Future research should include higher test levels, such as TL-5. A pier system of an existing bridge provided by KDOT was modeled and placed behind barriers in two TL-4 crash events. The first event included the sub-standard barrier in this study, while the other event included the standard TL-4 barrier tested in Sheikh et al. (2011). Because the behavior of the segmented boundary condition in terms of the QoI was between fixed and free, only the two extreme boundary conditions were considered in the case study. The distance between the face of the pier and the traffic face of the barrier was 3.25 ft, as per AASHTO. The center of the first pier corresponded to the location of the maximum lateral displacement depending on the boundary condition, as discussed in Section 4.3.3. The study then compared the effectiveness of each barrier for protecting the piers in terms of damage induced on the piers and the resulting contact force.

The numerical model of the pier system shown in Figure 4.18 contained the same material properties discussed in Section 4.1.3. The translational stiffness transverse to the bridge orientation and the torsional stiffnesses were obtained from the steel girders and deck slab, as represented by translational and rotational springs in Figure 4.18. Calculations of the translational and rotational springs stiffnesses are shown in Figure 4.19 and Equations 4.3–4.8. Since the translational stiffness in the direction of the bridge orientation was very high, rollers were placed across the depth of the pier beam to restrict motion in that direction. The base of the piers was fixed to model the pier piles and the stiff foundations. Only the dead load calculated from the tributary length of the bridge was uniformly applied as a surface load on the pier beam. The duration of the simulations was increased to 0.8 s to cover potential damage at advanced stages in the crash event. Damage induced on the barriers and the piers was investigated using the effective plastic strain fringe in LS-DYNA.

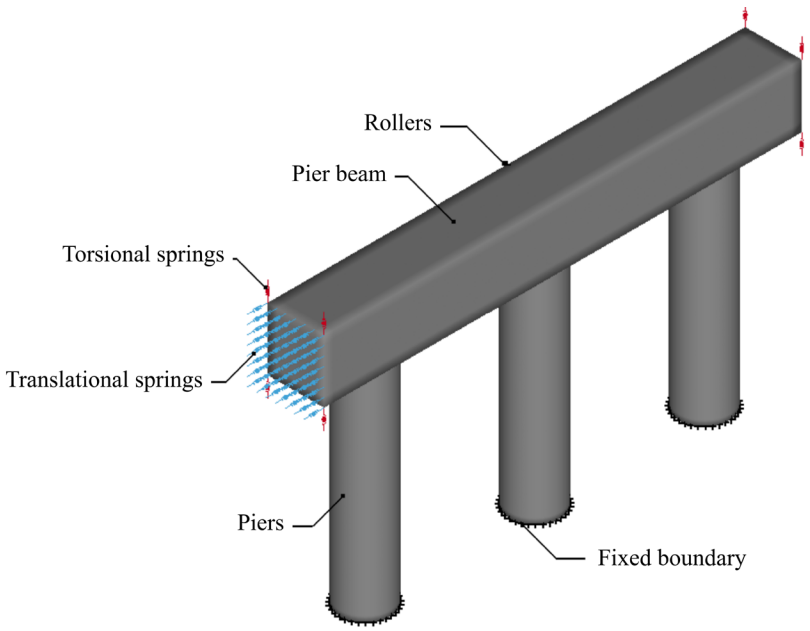

Figure 4.18: Numerical Model of the Pier System

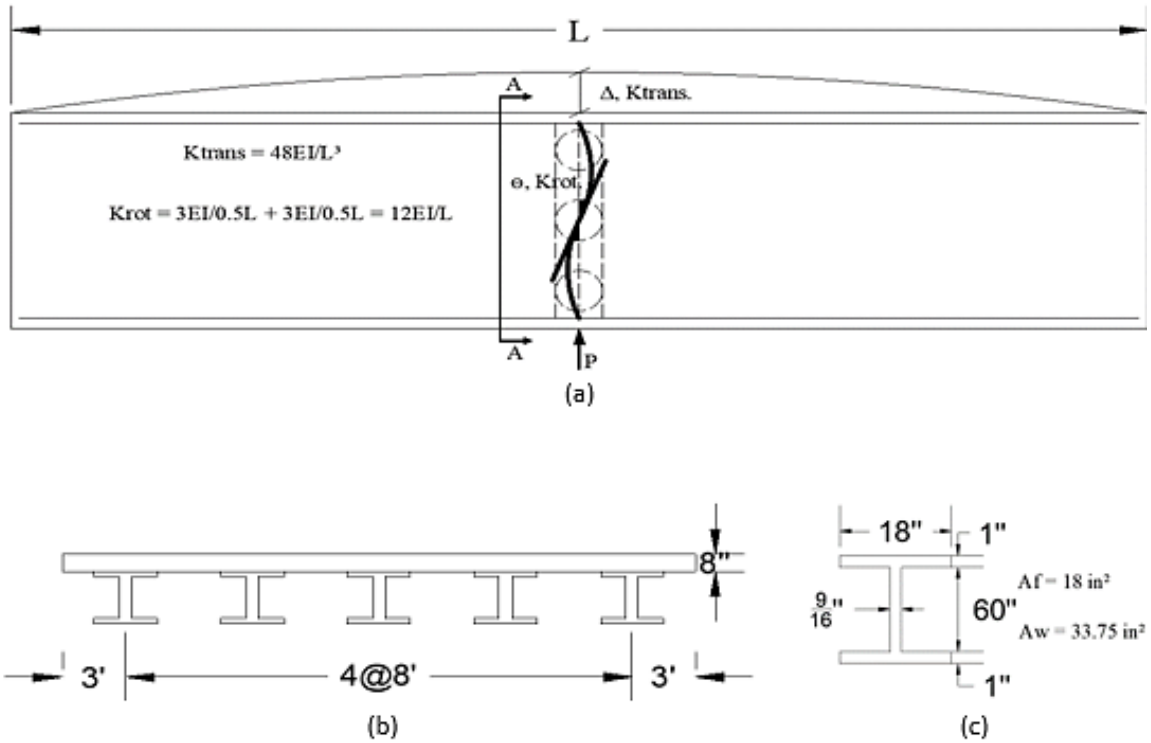

Figure 4.19: Stiffness Calculations for Numerical Model: (a) Bridge Layout, (b) Section A-A, (c) Girder Detail

$$E_c = 57\sqrt{4000} = 3605\ ksi$$

Equation 4.3

$$I_c = \frac{8 \times 456^3}{12} = 63212544\ in^4$$

Equation 4.4

$$I_s = \left(\frac{18^3}{12} \times 10 + 4 \times 18 \times 96^2 + 4 \times 18 \times 192^2 + 2 \times 33.75 \times 96^2 + 2 \times 33.75 \times 192^2\right) = 6433020\ in^4$$

Equation 4.5

$$EI = EI_c + EI_c = 3605 \times 63212544 + 29000 \times 6433020 = 4.144 \times 10^{11}\ k.in^2$$

Equation 4.6

$$K_{trans} = \frac{48 \times 4.144 \times 10^{11}}{3720^3} = 386.4\,\frac{k}{in}$$

Equation 4.7

$$K_{rot} = \frac{12 \times 4.144 \times 10^{11}}{3720} = 1.33 \times 10^9\ \frac{k.in}{rad}$$

Equation 4.8

As shown in Figure 4.20, the sub-standard barrier for fixed barriers (Figure 4.20(a)) was heavily damaged at the beginning of the crash event, causing the vehicle's cargo to approach the first pier. This contact was avoided for the standard barrier, shown in Figure 4.20(b). At a later stage in the event, as the vehicle tended to roll over the barriers, the last pier was hit by the vehicle in both barriers.

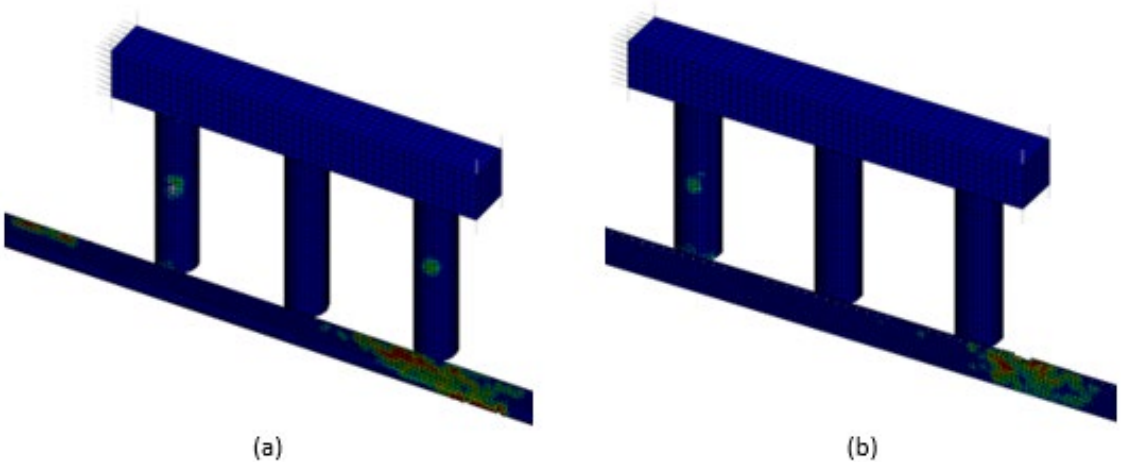

Figure 4.20: Damage to Piers Protected by (a) Fixed Sub-Standard Barrier, (b) Fixed Standard Barrier

VCF demand on the pier system with fixed barriers is shown in Figure 4.21. According to the figure, approximately 157.3 kips were applied to the first pier when protected by the sub-standard barrier when the contact was avoided in the case of the standard one. Approximately 269.6 kips were applied to the third pier for both barriers.

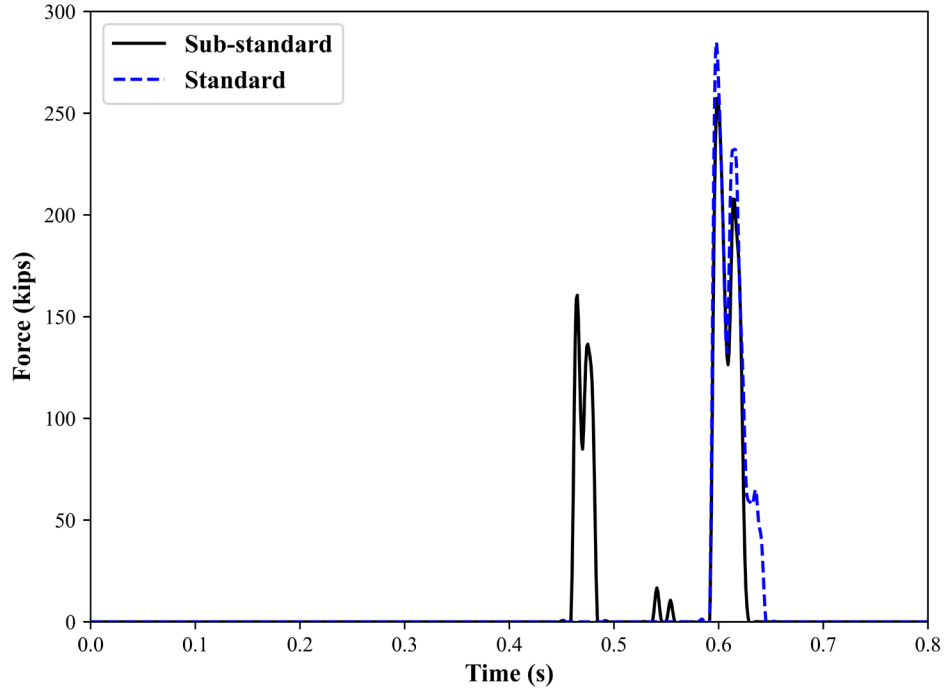

Figure 4.21: VCF on Bridge Piers Protected by Fixed Barriers

For the free boundary condition, both barriers deformed during the crash, and the vehicle was able to reach the first pier, as shown in Figures 4.22(a) and (b). However, the standard barrier decreased the damage on the middle pier. The VCF was approximately 180 kips in the first pier for both barriers and 269.7 and 168.6 kips in the middle pier with the sub-standard and the standard barriers, respectively (Figure 4.23). The vehicle model was not shown in Figures 4.20 and 4.22 to allow better observation of the damage of the elements under consideration.

The previous VCF values of the piers were obtained from a TL-4 crash event. Based on the findings in this case study, the sub-standard barrier should transfer higher VCF values to piers during a TL-5 crash event. However, when a standard TL-5 barrier is used, the vehicle may clear the pier system with minimal VCF transferred to the piers, which supports the current requirements of AASHTO (2020) specifications. Although the sub-standard barrier is not structurally adequate to solely protect bridge piers and allow them to withstand a VCF of 600 kips as per AASHTO (2020) specifications, the sub-standard barriers considerably reduce the required demand on the pier and allow feasible retrofitting solutions for aging bridge infrastructures.

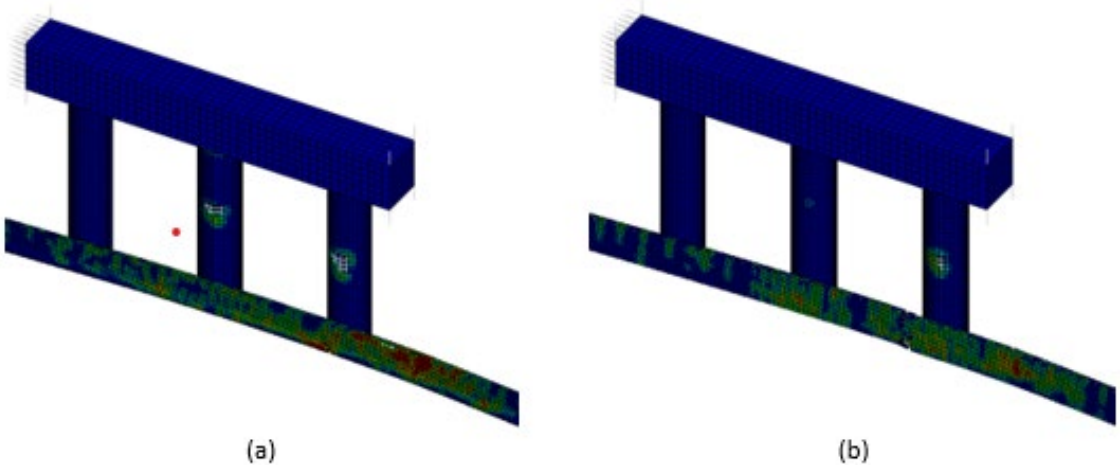

Figure 4.22: Damage to Piers Protected by (a) Free Sub-Standard Barrier, (b) Free Standard Barrier

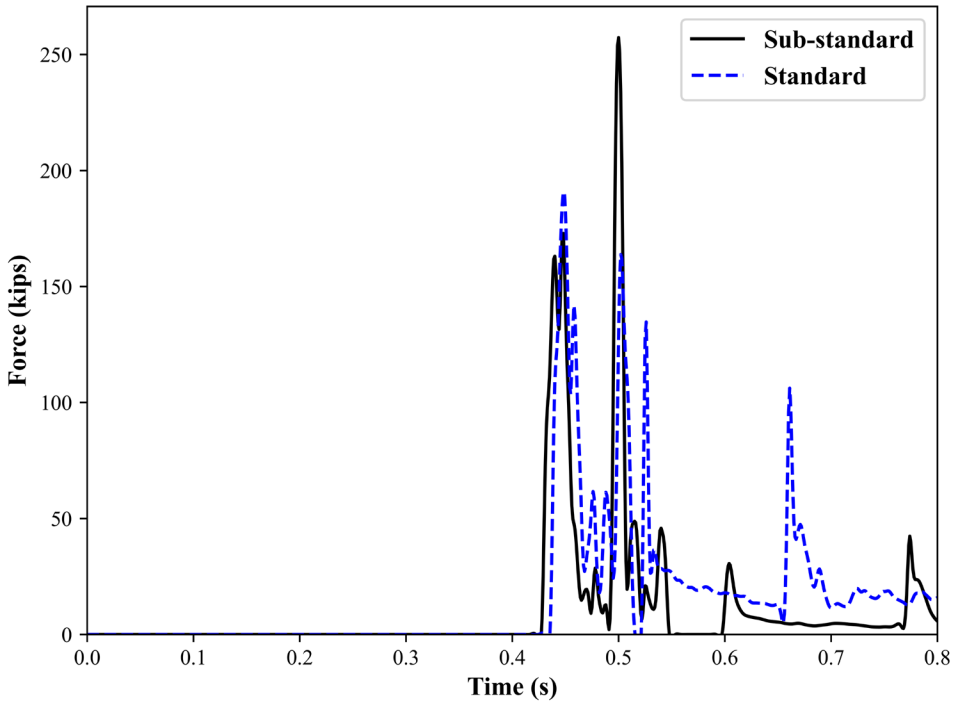

Figure 4.23: VCF on Bridge Piers Protected by Free Barriers

The peak VCF experienced in the TL-4 crash event was approximately 1200 kN, or 45% of the currently required ESF. This percentage is expected to be higher with a TL-5 crash event, but a reduction in AASHTO's requirements might still exist, which may offer some flexibility for engineers and decision makers in the highway industry.

4.5 Conclusions and Recommendations

In this study, common sub-standard barriers were examined to investigate their ability to lessen the level of impact damage and protect bridge piers from VCF. An extensive and detailed simulation matrix revealed decreased kinetic energy, velocity of the impacting vehicle, lateral displacement, and contact force demand on the barrier. A case study of a pier system was also simulated to compare a sub-standard barrier to a standard barrier to determine barrier effectiveness at reducing the impact effect on piers during a TL-4 crash event. The following conclusions were drawn:

1. The base boundary condition of the barriers significantly influences specific performance parameters. For example, the fixed base boundary

condition more efficiently reduces lateral displacement than the free base boundary condition, but it increases the contact force demand on the barrier and is less economically efficient.

2. For both test levels, the sub-standard barrier redirected the impacting vehicle without complete penetration. However, some overriding and rolling over occurred at later stages of the crash event. According to MASH, this type of barrier is structurally inadequate for TL-4 and TL-5 crash events.
3. As an intervening structure, structural inadequacy does not imply the inability to absorb impact forces. Based on the findings, this study recommends that AASHTO specifications accept sub-standard barriers as one level of protection for reducing the required lateral resistance of bridge piers to withstand VCF.
4. Future research should extend the current study to include bridge piers during TL-5 crash events for a more comprehensive understanding of critical VCF transfer to bridge piers with sub-standard barriers. Also, varying the distance between the pier face and the traffic face of the barrier would increase the evaluation accuracy of the recommended clear distance to minimize VCF on bridge piers.

Chapter 5: Estimation of Vehicular Collision Force on Bridge Piers with Sub-Standard Barriers

Critical infrastructures, such as bridges, should be able to resist extreme loading events. Among the potential hazardous events, vehicle collisions are becoming increasingly common. Modern AASHTO bridge design specifications require a limit state to account for VCF when bridge piers are within the clear zone defined by AASHTO (2020). AASHTO specifies two methods to address this limit state: (1) provide an intervening structure that can absorb the VCF and/or redirect the colliding vehicle, or (2) design the piers to resist a lateral load equivalent to 600 kips. Many aging bridges that were designed prior to recognizing the VCF as a limit state fail to meet modern specifications because either the piers were designed to resist a lower lateral load than the specified limit or the installed intervening concrete barrier is not standard and therefore not qualified to protect piers against VCF.

This paper introduces a new approach to address the requirements of modern standards. The approach is based on the blended contribution of a sub-standard barrier and the under-designed bridge pier in terms of VCF requirements, as well as a matrix of dynamic simulations using LS-DYNA to consider various crash scenarios. Results showed that a sub-standard barrier can decrease the estimated VCF by approximately 25%, leaving 75% to be resisted by the existing pier.

5.1 Simulation Matrix and Study Phases

The simulation matrix in this study consisted of a variety of parameters. For example, the SUT traveled at 56 mph to represent a TL-4 crash event, as described in Section 4.1.1, while the TST traveled at 50 mph to represent a TL-5 crash event, as described in Section 4.1.2. Two barrier boundary conditions were also considered; the fixed base barrier represented fixed installation by extending vertical reinforcing bars into the pavement along with free base barriers, such as PCBs. The barrier segment length was assumed to be 100 ft to comply with an experimental study by the NCHRP for a similar barrier type (Bullard et al., 2010) and the barrier model described in Section 4.1.3. The vehicles were directed to attack the barrier at an angle of 15° according to MASH guidelines (Table 2.1) for TL-4 and TL-5 crash events. AASHTO (2020) provisions recommend

that VCF be applied on bridge piers at a maximum angle of 15°, but this study expanded the simulation matrix to include a 25° angle of attack. Although this modified angle is unlikely to occur, especially under bridges, the simulation of steep angles is beneficial for load demand comparisons of piers relative to AASHTO's maximum angle.

This study also considered three pier locations along the barrier length to investigate the least desired position that attracts the highest contact force. Since dynamic simulations demand high computational costs and significant time and to keep the simulation matrix reasonable and achievable, the variation in pier location along the barrier's transverse direction was not considered in this study. Only the case that represented the worst loading scenario on the pier (located directly behind the barrier) was considered. Therefore, the pier position along the barrier's transverse direction was set to zero. The first vehicle-barrier contact point was 7 ft from the barrier edge, and the three positions of the pier were 3, 5, and 7 ft from the first vehicle-barrier contact point along the barrier length. The parameters of the simulation matrix are shown in Table 5.1.

Table 5.1: Simulation Matrix Parameters

Vehicle type	SUT				TST			
Barrier boundary	Fixed		Free		Fixed		Free	
Barrier segment length (ft)	100							
Angle of vehicle attack	15°	25°	15°	25°	15°	25°	15°	25°
Pier location with respect to the barrier edge (ft)	10		10		10		10	
	12		12		12		12	
	14		14		14		14	

In the first phase of the study, the simulation matrix was composed of 24 simulations. A simulation with the name [SUT_Fixed_100_15_10] represented a crash event involving an SUT vehicle impacting a fixed base and a 100-ft long barrier at an angle of 15° with a pier behind the barrier located 10 ft from the barrier's edge (Figure 5.1). The objective of this phase was to determine the critical dynamic impact force (DIF) based on a proposed ESF to account for the

VCF for a sub-standard barrier. In the second phase, the obtained ESF was applied laterally to obtain the internal forces in the pier, which were then compared to the pier's actual capacity.

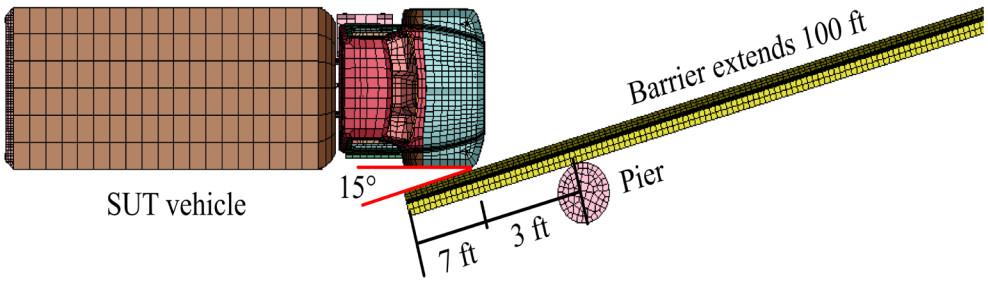

Figure 5.1: Simulation Matrix Parameters

5.2 Phase 1: Modeling and Results

5.2.1 Under-Designed Pier

5.2.1.1 Geometry and Materials

The pier models in this study were designed according to KDOT, with a length of 18.5 ft and a cross-section, as shown in Figure 5.2(a). The same material models used for the barrier were used in the pier model. All rebars were explicitly modeled as beam elements, and the concrete was modeled as solid elements. The reinforcement was constrained within the concrete barrier using a Lagrange-in-solid constraint. Parameters for the models were taken from LS_DYNA (Livermore, 2017), and details on the concrete-material model validation and calibration were taken from Agrawal et al. (2018). The concrete and steel properties used in the simulations are shown in Table 4.1.

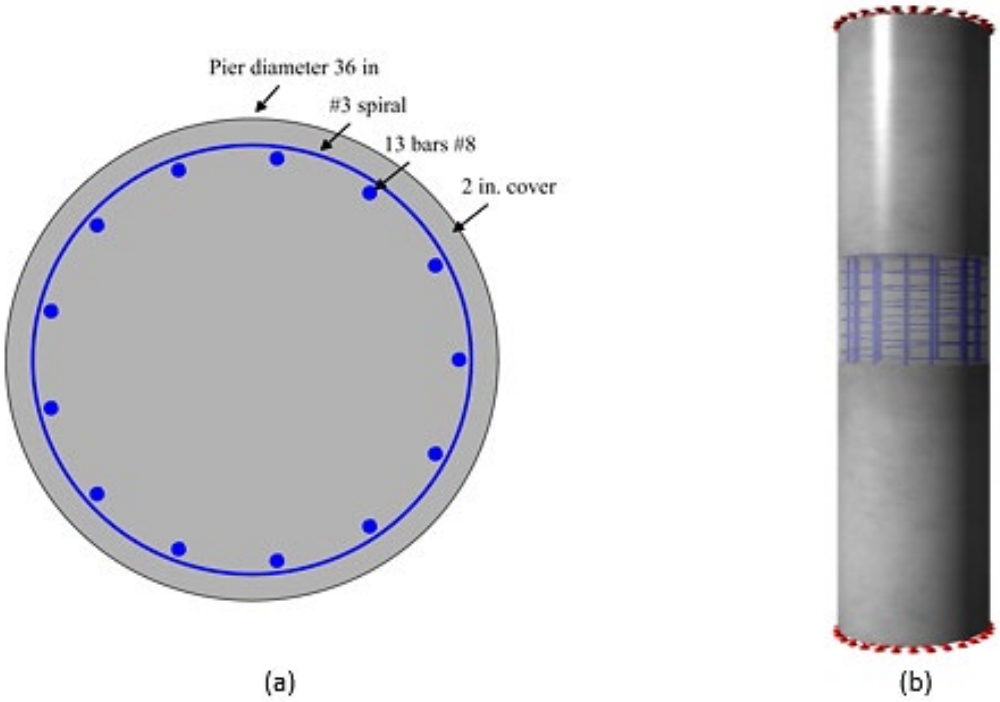

Figure 5.2: (a) Pier Cross-Section and Details, (b) Boundary Condition

5.2.1.2 Boundary Conditions

This study considered two boundary conditions for the barrier. First, the fixed base boundary was achieved by fixing all the dowel nodes at the base level, as shown in Figure 4.5(a), while in the free base boundary, only dowels within 3 ft (1 m) of the barrier edges were fixed to provide barrier anchorage, as shown in Figure 4.5(b). The pier was fixed on both ends to achieve maximum stiffness and attract higher contact force, as shown in Figure 5.2(b).

5.2.1.3 Standard Requirements

The barrier was considered sub-standard because its clear height was 32 in., which was less than the 42 in. specified by AASHTO (2020). The pier was subjected to an ESF of 600 kips as suggested by AASHTO (2017). The provisions require that the ESF be applied 2.0–5.0 ft from the ground level (Figure 5.3). The end moments and shears for the fixed-fixed boundary shown in Figure 5.3 were found using Equations 5.1–5.4 and calculated in Table 5.2.

$$M_{ab} = \frac{Pab^2}{L^2}$$

Equation 5.1

$$V_{ab} = \frac{Pb^2(3a + b)}{L^3}$$

Equation 5.2

$$M_{ba} = \frac{Pba^2}{L^2}$$

Equation 5.3

$$V_{ba} = \frac{Pa^2(a + 3b)}{L^3}$$

Equation 5.4

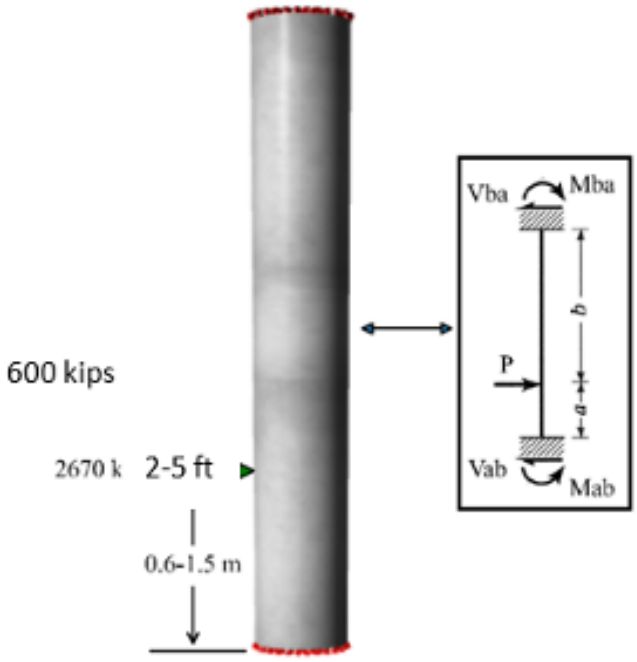

Figure 5.3: End Forces in the Pier

Table 5.2: Internal Forces in the Pier (Figure 5.3) Due to 600 kips VCF

a (Figure 5.3)	Moment		Shear	
	End	Kip.ft	End	Kips
2 ft	Mab	954.57	Vab	580.48
	Mba	115.70	Vba	19.52
5 ft	Mab	1597.52	Vab	492.21
	Mba	591.67	Vba	107.79

The capacity of the pier section was calculated using KDOT Column Expert software to adapt the model developed by Rasheed and Abouelleil (2015) and provide a shear-moment capacity interaction diagram at a specific axial force. The user interface and input parameters used in the software for the pier are shown in Figure 5.4.

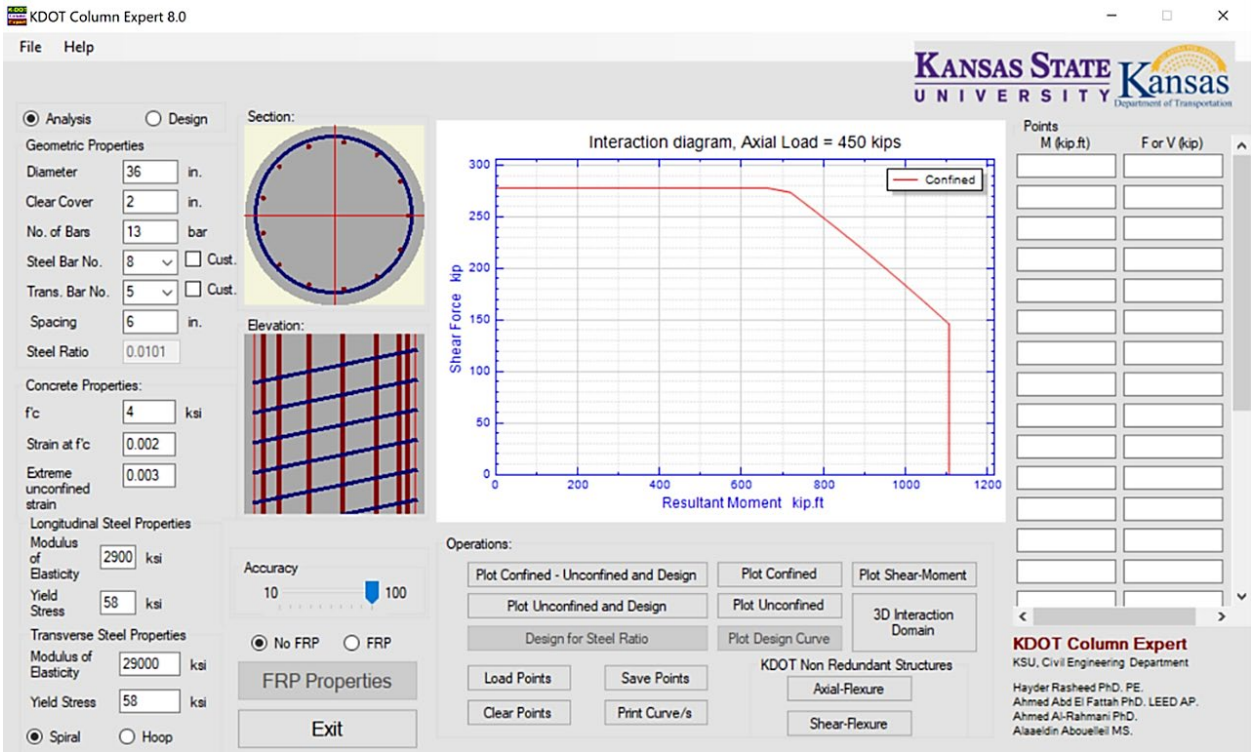

Figure 5.4: KDOT Column Expert User Interface and Input Parameters

The capacity of the pier section was calculated with the pier subjected to an axial load comprised of dead load effects from the bridge beam, girders, and the deck. The dead load calculations were based on the tributary length of the bridge segment above the pier beam, a length that was equal to half the distance to the abutments from each side for a bridge with a single pier line, or the length was equal to half the distance to the abutment plus half the distance to the next pier for the exterior piers line for the bridge shown in Figure 2.1. In addition, a tributary length of 124.6 ft resulted in an approximated axial load of 450 kips, assuming a two-pier transfer beam. The capacity interaction diagram for the pier under the given estimated axial loading (Figure 5.5) shows that the pier would not resist the 600 kips ESF suggested by AASHTO, making it an under-designed pier.

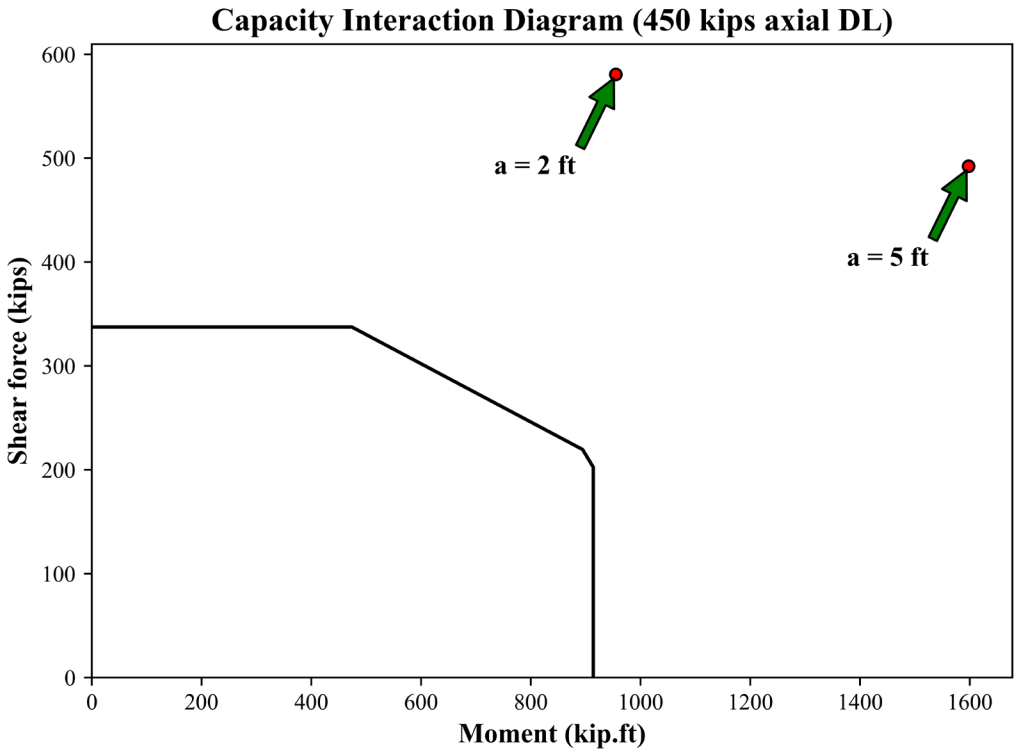

Figure 5.5: Capacity Interaction Diagram for the Pier

5.2.2 Simulation Results

In this study, the contact force demand on the pier behind the barrier was a result of vehicle-pier contact and barrier-pier contact. The vehicle-barrier contact was not reported because it did not influence the load demand on the pier. Figures 5.6(a)–(d) show the results of the SUT vehicle when attacking fixed and free barriers at angles of 15° and 25°. The results are summarized in Table 5.3. The results showed that the barrier boundary did not significantly influence the DIF. The similarity of the PIF and the critical location of the pier in both boundary conditions in the two angles of attack could be due to direct engagement of the pier in the impact because of the close distance between the pier and the first contact point. If the pier had been further from the contact point, higher forces would have been absorbed by the barrier, yielding lower contact forces for the pier. However, the intent of this study was to place the pier in the critical location to resist higher impact forces rather than investigate the effect of barrier boundary conditions on contact force absorption.

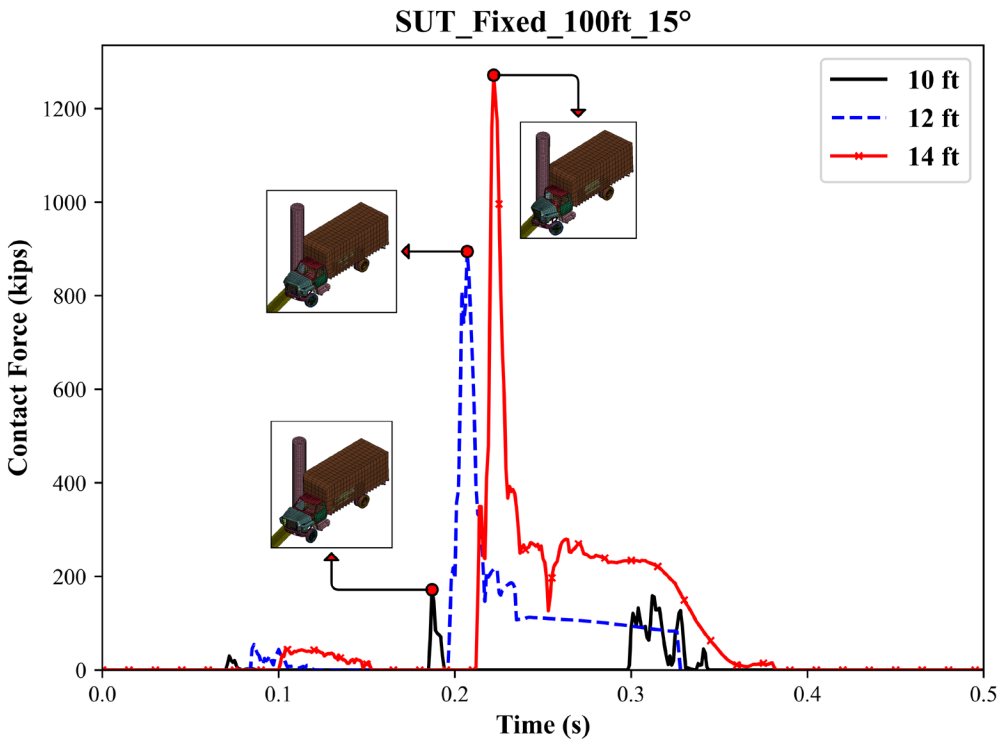

(a)

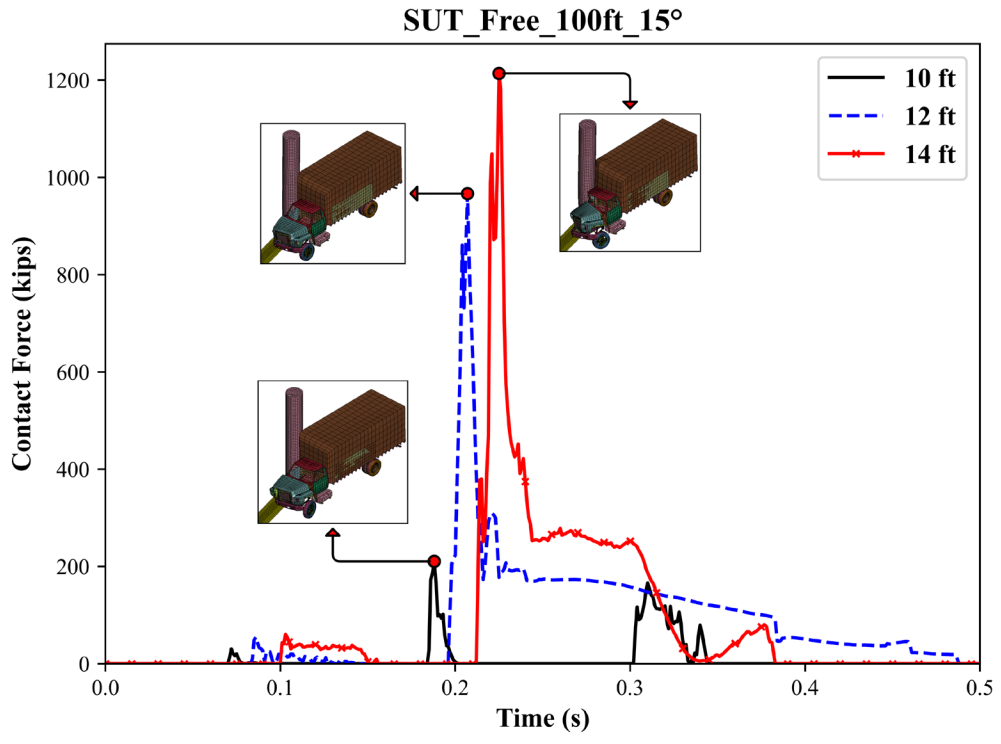

(b)

Figure 5.6: Dynamic Impact Force from TL-4 Vehicle at: (a) Fixed Barrier at 15°; (b) Free Barrier at 15°; (c) Fixed Barrier at 25°; (d) Free Barrier at 25°

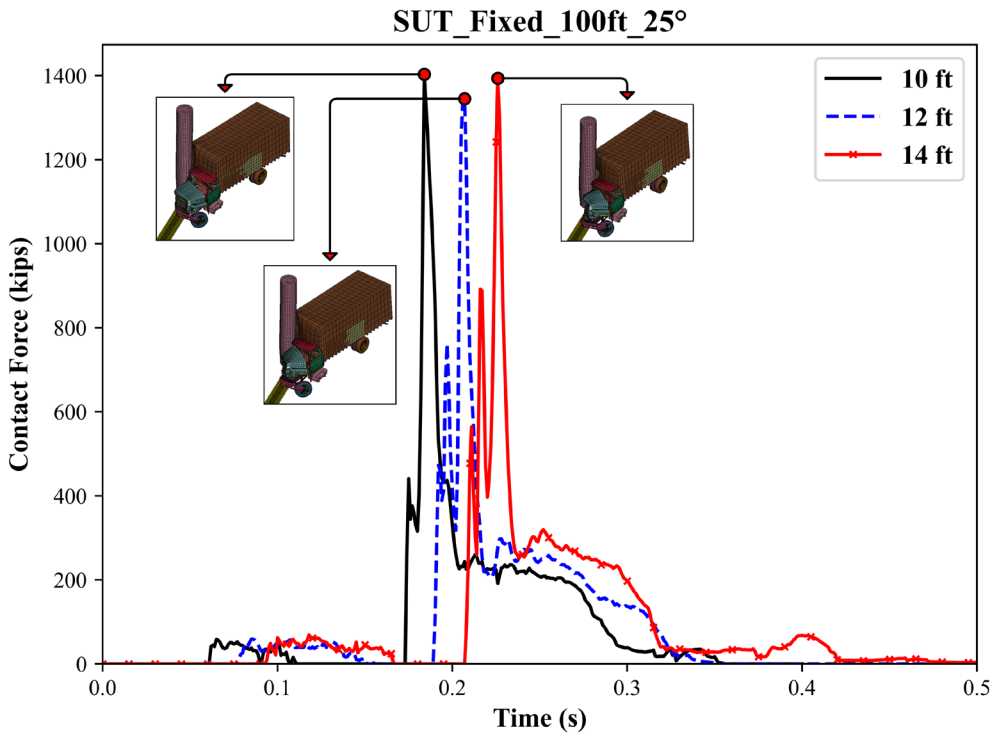

(c)

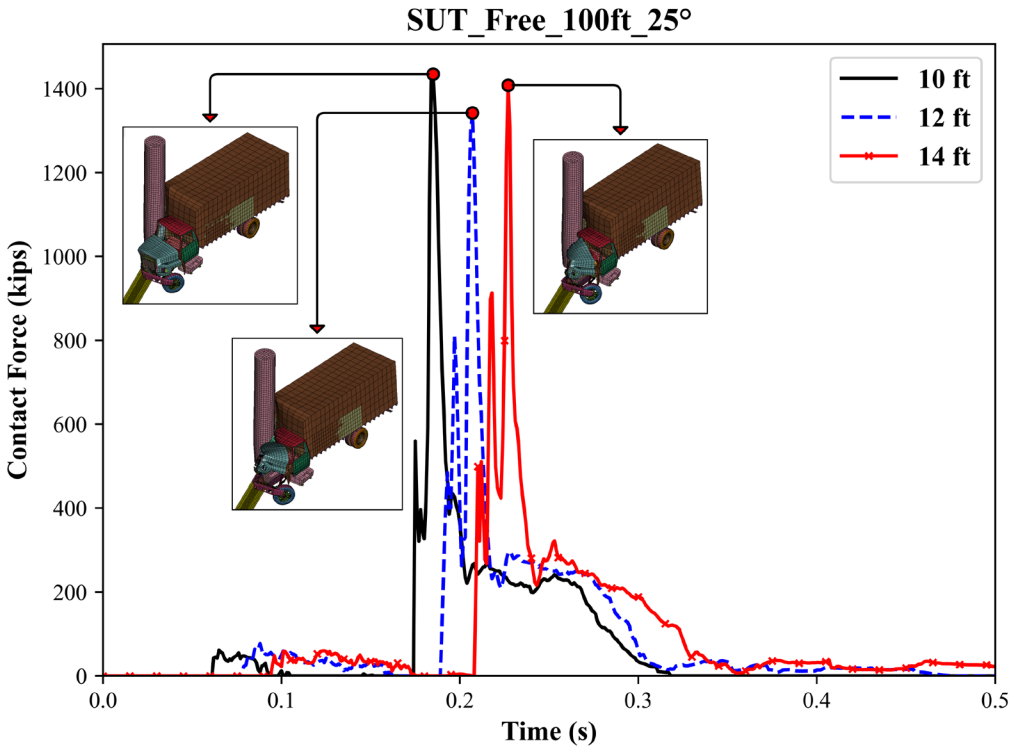

(d)

Figure 5.6 (continued): Dynamic Impact Force from TL-4 Vehicle at: (a) Fixed Barrier at 15°; (b) Free Barrier at 15°; (c) Fixed Barrier at 25°; (d) Free Barrier at 25°

As expected, impact force increased when the angle of attack was 25° because the impacting vehicle tended to penetrate the barrier rather than deviate and regain stability. For the TST vehicle, Figures 5.7(a) and (b) reflect a similar trend to the SUT regarding the effect of boundary condition on the DIF when the angle of attack is 15° with a slightly higher PIF when the barrier has a free base.

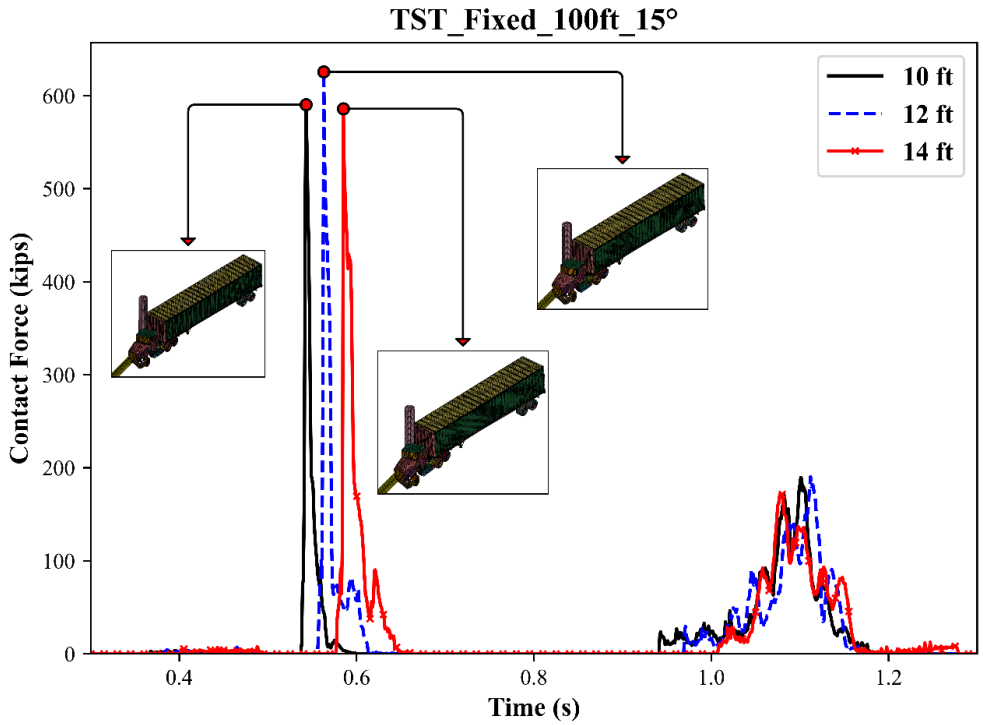

(a)

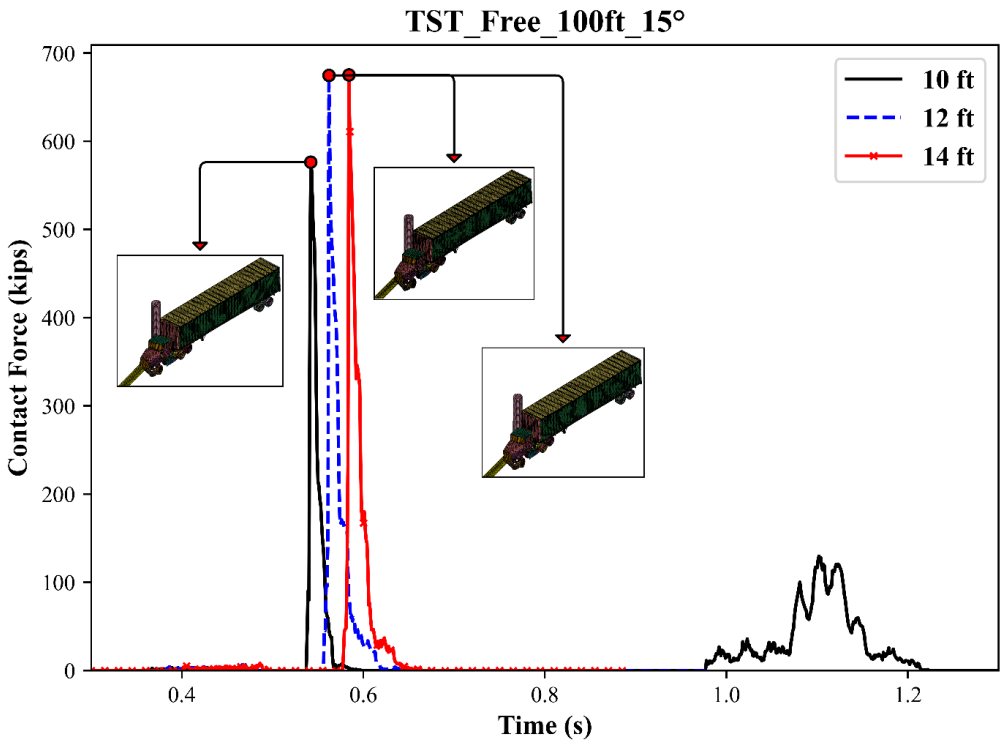

(b)

Figure 5.7: Dynamic Impact Force from a TL-5 Vehicle: (a) TST Fixed Barrier at 15°; (b) TST Free Barrier at 15°; (c) TST Fixed Barrier at 25°; (d) TST Free Barrier at 25°

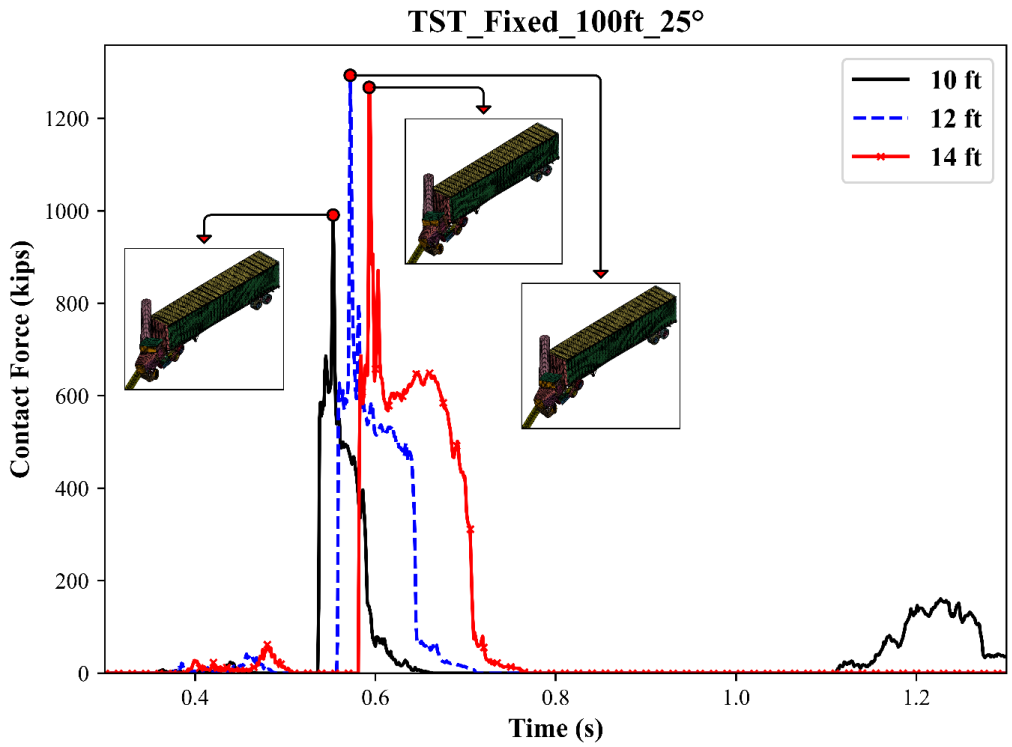

(c)

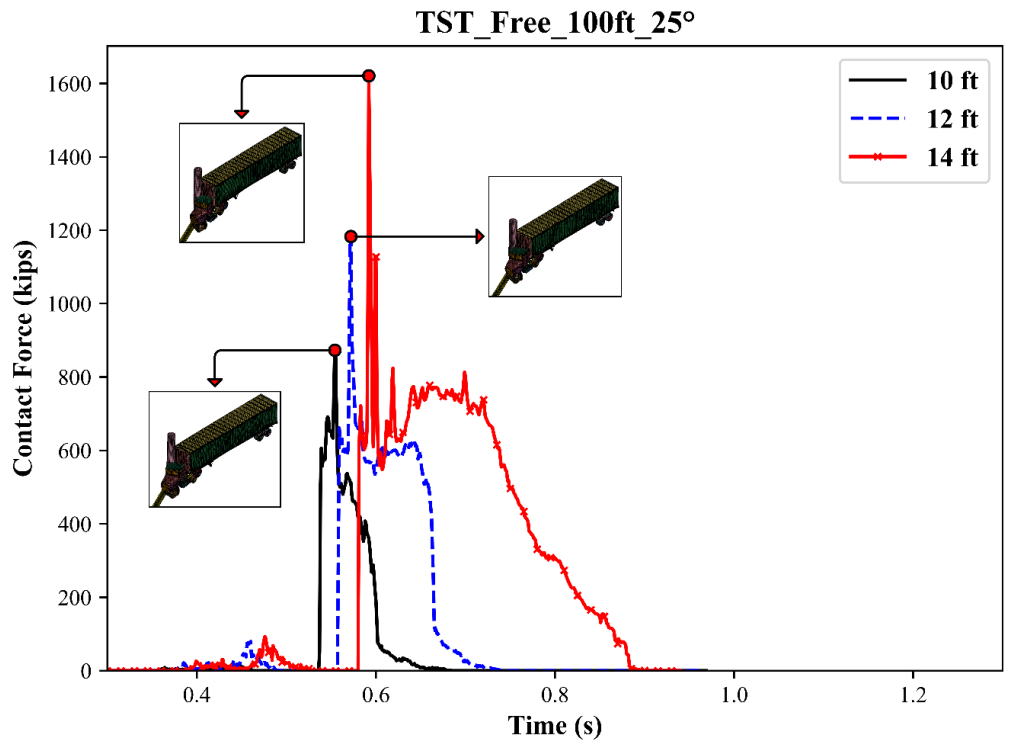

(d)

Figure 5.7 (continued): Dynamic Impact Force from a TL-5 Vehicle: (a) TST Fixed Barrier at 15°; (b) TST Free Barrier at 15°; (c) TST Fixed Barrier at 25°; (d) TST Free Barrier at 25°

For the 25° angle of attack, the effect of the boundary conditions was more influential, and the free base barriers produced higher contact forces, potentially due to decreased energy absorption capacity of the free barrier, which resulted in higher forces transferred to the pier. The PIF for each simulation is reported in Table 5.3.

Table 5.3: Simulation Matrix PIF

Vehicle type	SUT				TST			
Barrier boundary	Fixed		Free		Fixed		Free	
Barrier segment length (ft)	100							
Angle of vehicle attack	15°	25°	15°	25°	15°	25°	15°	25°
Critical pier location	14	10	14	10	12	12	14	14
PIF (kips)	1272	1404	1214	1435	626	1294	675	1621

5.2.3 Dynamic Impact Force versus Equivalent Static Force

Accurate estimation of the applied loads is essential for analyzing and designing structural elements, especially for dynamic loads that have high fluctuation of load values during loading. Existing research and guidelines suggest an ESF to simplify the analysis and design process. The method of reflecting the dynamic effect via the estimated ESF depends on the type of dynamic load. For example, highway sign structures subjected to wind loading are analyzed and designed by applying an estimated static pressure equivalent to the wind load. However, the dynamic nature of the wind is reflected by amplifying the applied static pressure using a dynamic amplification factor (DAF) that is a function of the dynamic properties of the structure (Al Shboul et al., 2021). The same concept applies when applying seismic loads that are dynamic in nature using the equivalent static method or the response spectrum (Salahat & Martinez-Vazquez, 2015).

Sharma et al. (2012) showed that dynamic shear force applied to piers from VCF is greater than the static forces and varies depending on the impact scenario. Previous studies have evaluated the VCF on structural elements to quantify a conservative ESF for analysis and design and to determine the impact capacity of the structural member subjected to collision. For example, Roy

et al. (2021) conducted a state-of-the-art review of studies on the damage induced on bridge piers due to VCF, and several models for obtaining the ESF from VCF were summarized. The current study focused on three models to analyze and compare and eventually adopt one model to use in this study.

5.2.3.1 Model 1: Modified Global ESF

Model 1 is a modified version of the model presented by Zhou et al. (2017). The original model to determine the global equivalent static force (GESF) is given in Equation 5.5.

$$GESF = \frac{\int_0^t p(i)di}{t}$$

Equation 5.5

Where $p(i)$ is the force at instant i and t is the impact duration.

The modification to this model was the elimination of instances when contact between the vehicle and the pier were lost (i.e., points of zero contact force), consequently producing a new time history that included the effective impact time. The contact forces were then averaged over the continuous period of contact. Figure 5.8 shows an original and modified contact force graph, where the ESF is the integration of the filled area divided by the effective impact time.

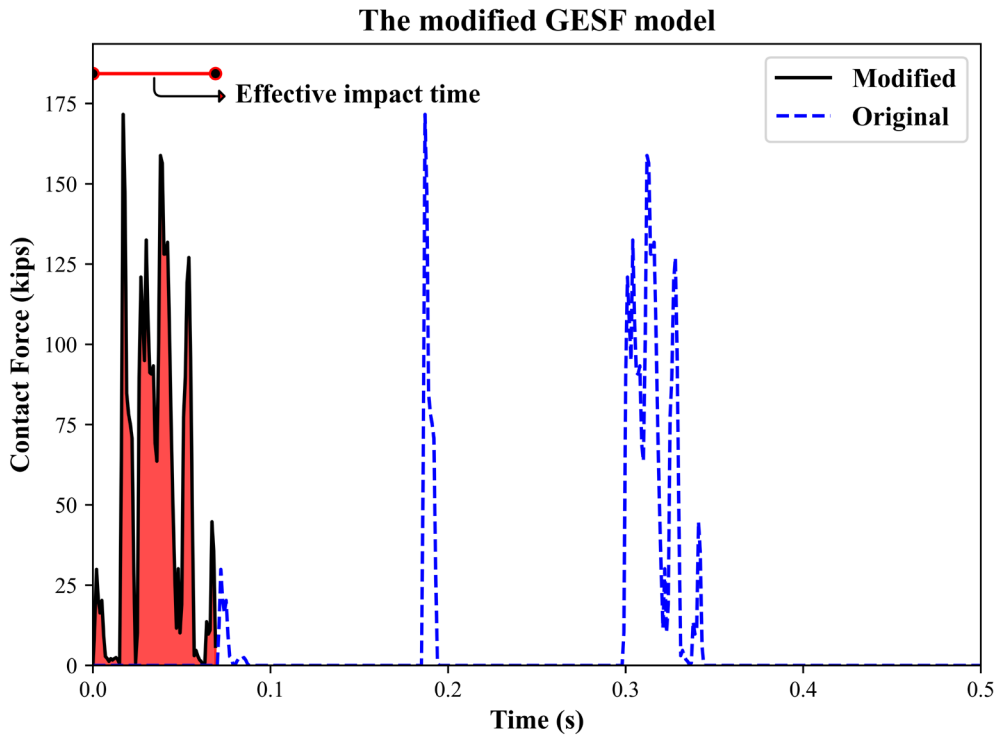

Figure 5.8: ESF Averaged over the Effective Impact Time Based on Model 1

5.2.3.2 Model 2: Local ESF

Zhou and Li (2018) initially presented Model 2 (Equation 5.6), which is based on the average DIF in the local zone of the PIF over a 50-ms time window centered at the PIF point to obtain the local equivalent static force (LESF), as shown in Figure 5.9.

$$LESF = \frac{\int_{tp-25}^{tp+25} p(i)di}{50}$$

Equation 5.6

Where $p(i)$ is the force at instant i and tp is the time corresponding to the PIF.

The ESF is the integration of the filled area divided by 50-ms.

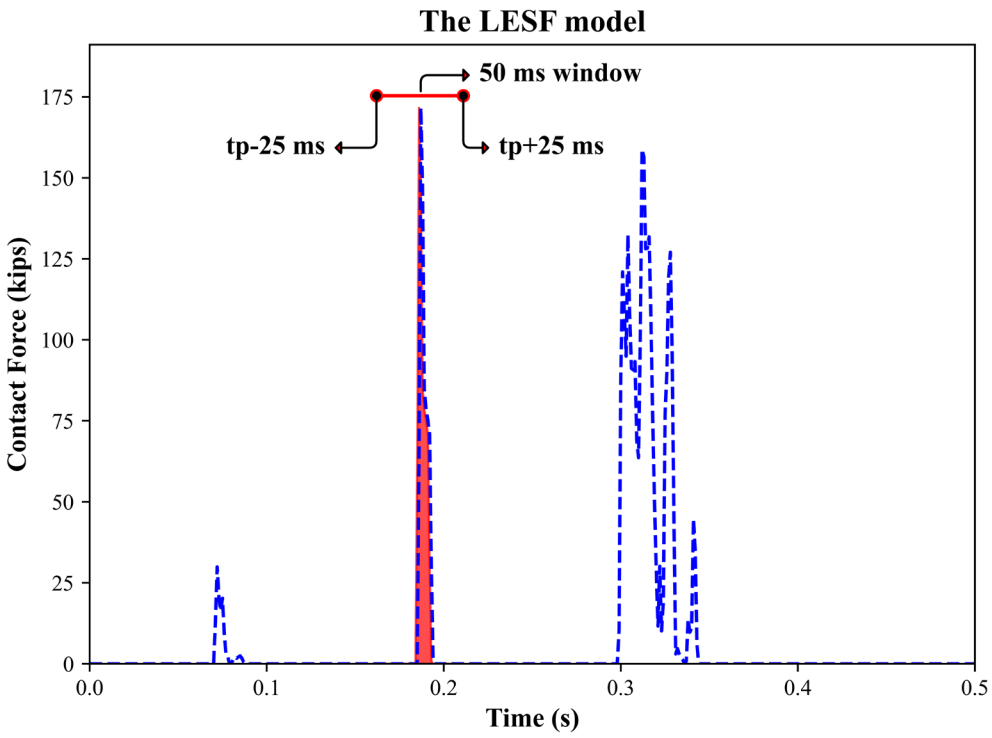

Figure 5.9: ESF Averaged over 50-ms Window Based on Model 2

Although this model reduces the effect of non-critical impact instances, the 50-ms time window allows non-critical instances that significantly reduce the ESF (Figure 5.9). Therefore, Abdelkarim and ElGawady (2017) suggested a model that considered the peak of a 25-ms moving average, which this study adopted but changed the averaging window to 50 ms.

5.2.3.3 Model 3: Peak of Fifty Millisecond Moving Average

Model 3, Peak of Fifty Millisecond Moving Average (PFMSA), captures the PIF throughout the impact time history. As shown in Figure 5.9 the model attributes less influence to DIF over very short durations (0.18–0.2 s) and higher influence to the contacts acting over longer durations (0.3–0.35 s). Figure 5.10 compares contact forces of the original time history obtained from simulations and Model 3, where the ESF is the PFMSA. Results of the three models are summarized in Table 5.4. As shown in the table, Model 1 significantly reduced the PIF in almost all the simulations, while the results of Models 2 and 3 yielded close values in the ESF. Therefore, the ESF obtained from Model 3 was used in Phase 2 of this study.

Since the boundary conditions did not significantly influence the PIF, a uniform ESF was selected to govern both boundaries. The selected ESFs for the SUT attacking at 15° and 25° were 450 and 472 kips, respectively. For the TST, the selected ESFs were 169 and 753 kips for 15° and 25°, respectively. Because AASHTO specifications require the VCF to act in a direction of 0–15°, a comparison of the proposed values for this angle of attack to the current standard of 600 kips yielded a reduction of 25% and 72% for the SUT and TST, respectively.

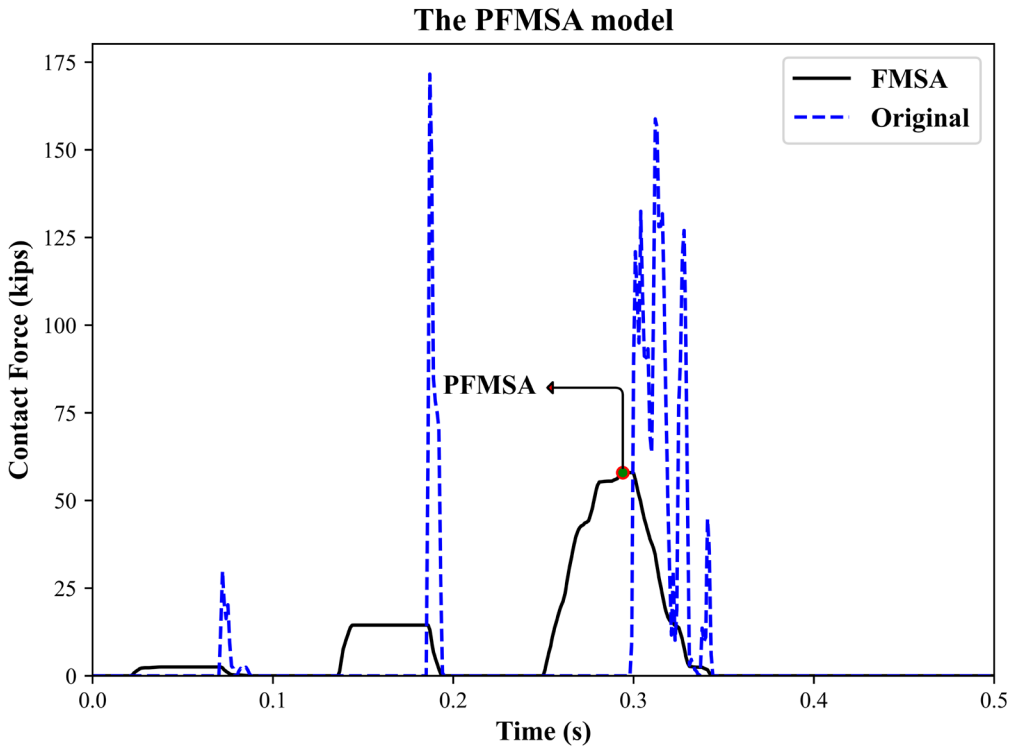

Figure 5.10: ESF as Peak of 50-ms Moving Average Based on Model 3

Table 5.4: ESF for the Three Models

Vehicle type	SUT				TST			
Barrier boundary	Fixed		Free		Fixed		Free	
Barrier segment length (ft)	100							
Angle of vehicle attack	15°	25°	15°	25°	15°	25°	15°	25°
PIF (kips)	1272	1404	1214	1435	626	1294	675	1621
ESF1 (kips)	177.4	172.2	178.3	203	45.8	261	49.3	333.7
ESF2 (kips)	328.1	428.3	377	413.5	152.8	500	161.3	539
ESF3 (kips)	407.8	454.5	450	463.1	173	677.2	174.6	758
ESF1/PIF	0.14	0.12	0.15	0.14	0.07	0.20	0.07	0.21
ESF2/PIF	0.26	0.31	0.31	0.30	0.24	0.39	0.24	0.33
ESF3/PIF	0.32	0.33	0.37	0.33	0.28	0.52	0.26	0.47

5.3 Phase 2: Application of the Modified VCF

Phase 2 of this study focused on the location of the first impact point between the colliding vehicle and the pier using dynamic analysis. Based on this location, the ESF proposed in the previous section was applied, and internal forces in the pier were compared to the pier capacity. Figures 5.11(a) and (b) show two simulations of the SUT corresponding to 15° and 25° angles of attack, respectively. As shown, the location of the first impact point was approximately 4 ft from the ground. For the TST simulations, this location reached up to 13.5 ft from the ground, as shown in Figures 5.11(c) and (d) for 15° and 25°, respectively. Table 5.5 shows the end moments and shears for the ESF at the locations in Figure 5.11 for the corresponding simulations.

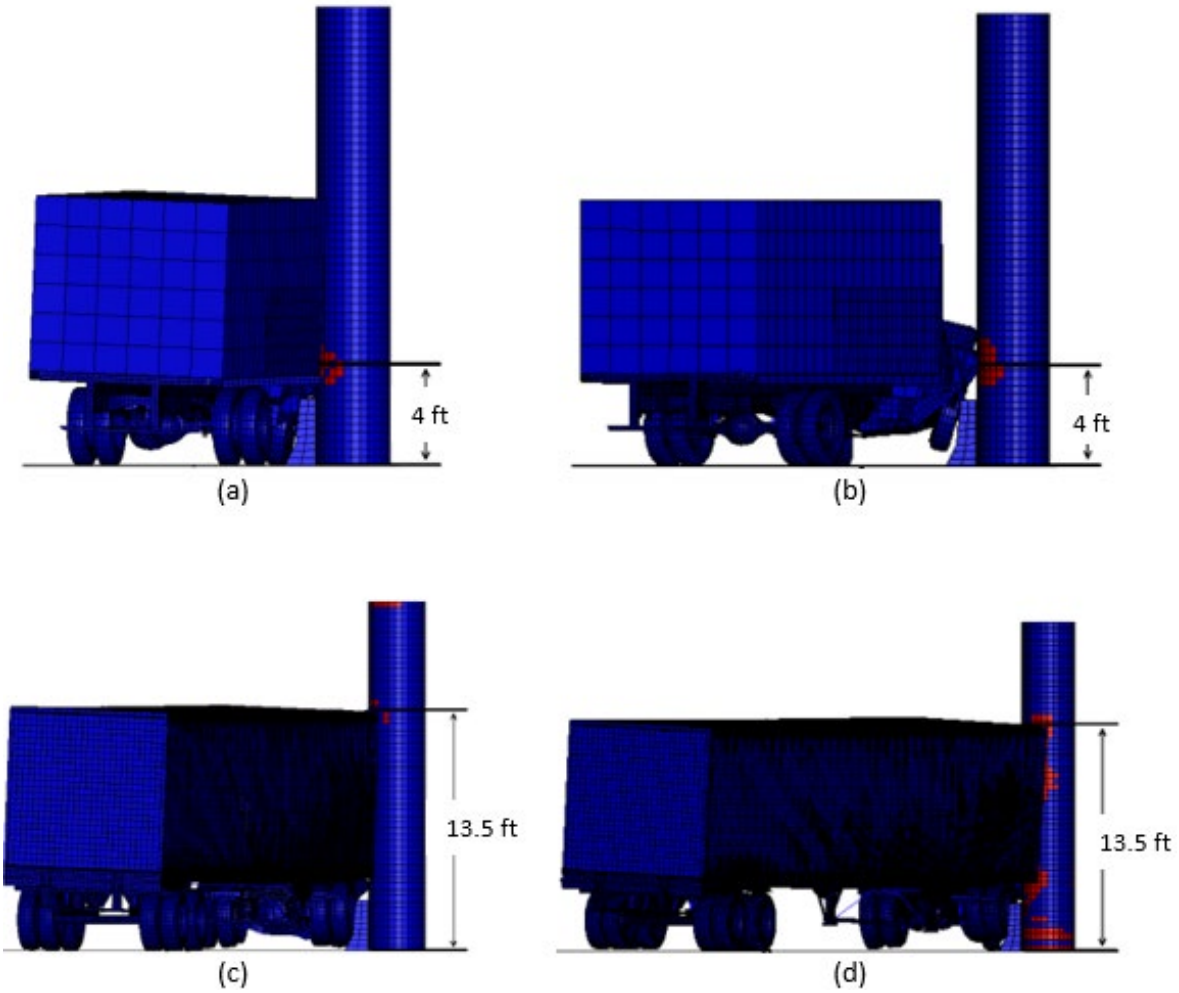

Figure 5.11: Locations of ESF Application: (a) SUT at 15°; (b) SUT at 25°; (c) TST at 15°; (d) TST at 25°

Table 5.5: Critical Internal Forces for the Proposed ESF

Vehicle	Angle	ESF (kips)	a (ft)	Moment (kip.ft)		Shear (kips)	
				Mab	Mba	Vab	Vba
SUT	15°	450	4	1105.7	305	396	54
	25°	463.1	4	1138	314	407.5	55.6
TST	15°	174.6	13.5	172.2	464.8	31.4	143.2
	25°	758	13.5	747.5	2018.2	136.2	621.8

Shear and moment diagrams revealed that the critical shear and moment at one of the pier ends was the critical internal shear and moment in the pier. These values were included in the capacity interaction diagram shown in Figure 5.12.

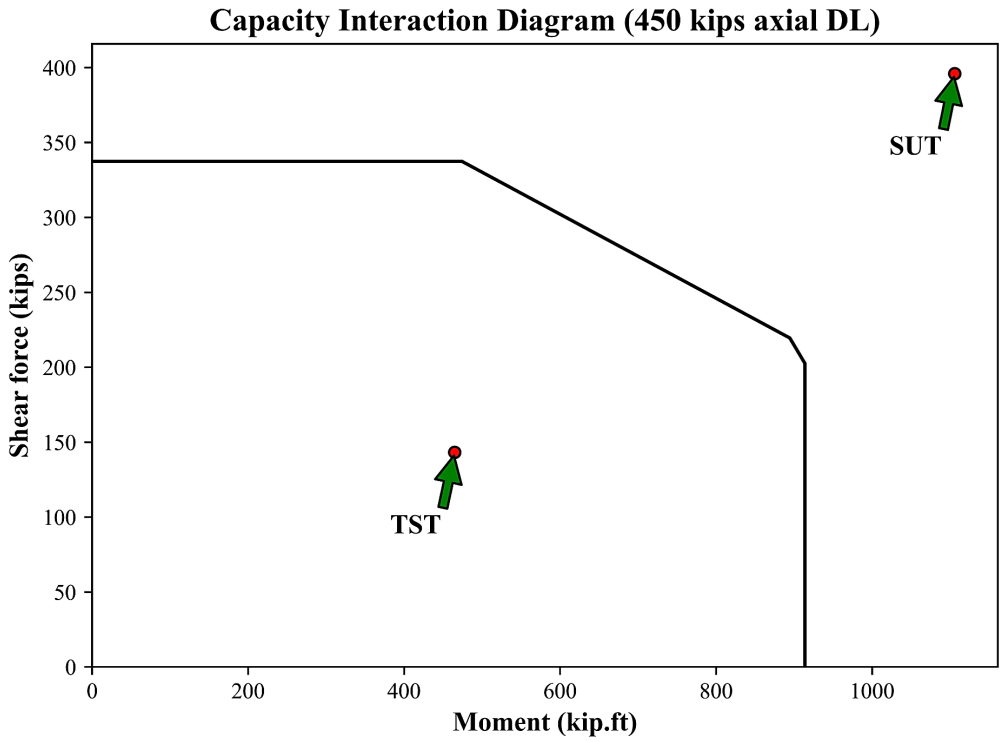

(a)

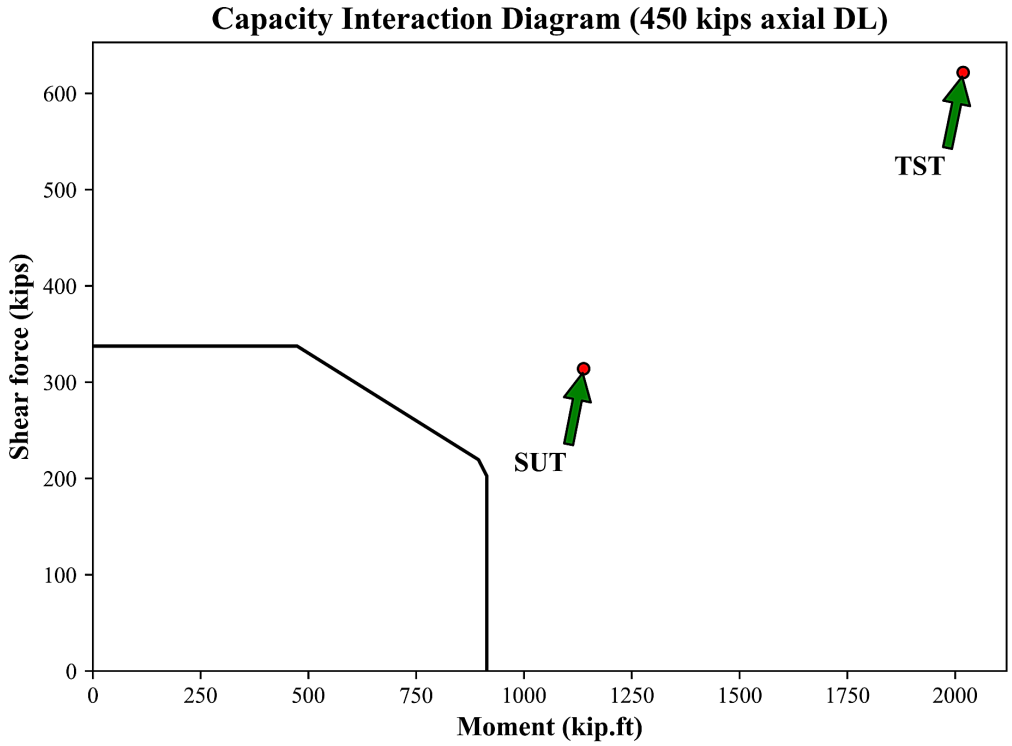

(b)

Figure 5.12: Pier Adequacy with Proposed VCF: (a) 15° Angle of Attack, (b) 25° Angle of Attack

As shown in Figure 5.12, when the angle of attack was 15°, the pier resisted internal forces produced by the impact of the TST. However, the SUT vehicle produced high shear values beyond the capacity of the pier, potentially because the mass concealed in the back of the SUT vehicle directly impacted the pier, consequently producing high inertial forces. Although the TST vehicle was used to describe TL-5 crash events, designers should be aware that impacts with lumped masses in vehicles traveling at high speeds yield high shear demands when the crash event happens. When the angle of attack was 25°, the pier failed to meet the shear and moment demands caused by the impact, even with sub-standard barriers, meaning strengthening techniques should be applied to upgrade the pier capacity against VCF. However, attacks at this angle are unlikely to occur, as previously discussed.

5.4 Conclusion

This study conducted a comprehensive dynamic finite element parametric study to assess the effect of sub-standard barriers as intervening structures to reduce VCF on bridge piers. The main parameters of the study were type of colliding vehicle, angle of attack, boundary conditions of the intervening sub-standard barrier, and pier location along the barrier length. A specific sub-standard barrier and pier design were implemented from KDOT drawings for this parametric study. Results showed that the pier was deficient under the required AASHTO ESF to address the VCF, but the parametric simulations resulted in a range of DIF time histories. By extracting the PIF from these time histories and converting them into ESF values, the proposed reduction in VCF was evaluated. For the angle of attack specified by AASHTO, the TL-5 crash scenario was within the interaction capacity of the examined pier design; however, the TL-4 crash scenario exceeded the capacity. Extending the angle of attack to 25° showed that the TL-4 and the TL-5 cases required bridge pier strengthening. In addition, the center of the impact force for the SUT was within the range of heights adopted by AASHTO but not within range for the TST where the center of the impact occurred at a much higher height. Therefore, some of these important findings related to the ESF reduction and the location of its application should be included in future editions of AASHTO bridge design specifications to reduce demand on piers with sub-standard barriers.

Chapter 6: Conclusions and Recommendations

The aim of this research was to assess the performance of sub-standard RC barriers as protection for bridge piers against VCF and quantify their reduction of the ESF that piers must resist. Several objectives were established for this research. The first objective was to explore current methodologies to obtain the lateral capacity of RC barriers and propose accurate methods to predict the actual transverse capacity of RC barriers. Subsequent investigation showed that the current AASHTO procedure of YLA significantly underestimates the transverse capacity of RC barriers. This study also developed a detailed YLA procedure and a truss technique as alternative methodologies for estimating the transverse capacity of RC barriers. A case study of a sub-standard barrier was analyzed using these methods and verified against FEA using Abaqus. Results showed agreement between the FEA and the proposed methods, and the AASHTO YLA was shown to underestimate the capacity of the sub-standard barrier by approximately 50%.

The second objective of this study was to assess the performance of sub-standard barriers as bridge pier protection to comprehensively understand barrier behavior during high TL crash events (TL-4 and TL-5). An extensive and detailed simulation matrix was conducted for various QoI, including kinetic energy, velocity of the impacting vehicle, lateral displacement, and contact force demand on the sub-standard barrier. Results confirmed that the sub-standard barrier was disqualified because the vehicle rolled over. However, in both TLs, the sub-standard barrier redirected the impacting vehicle without penetration. The results also showed that the base boundary condition of the barrier significantly influences important performance parameters such as the contact force and the lateral displacement. For example, compared to the free-base boundary condition, the fixed-base boundary condition more efficiently reduces lateral displacement and increases the contact force demand on the barrier, but it is less economically efficient.

The third objective of this research was to assess the effect of sub-standard barriers for reducing VCF on bridge piers. A bridge pier that inadequately addressed VCF under the required AASHTO ESF was applied to a simulation matrix to obtain a range of DIF time histories. After obtaining the ESF from these time histories, the proposed reduction in VCF was at least 25%.

The following recommendations are based on the results of this research:

1. A distinction in the structural adequacy criterion must be made between the barrier's load resistance and its geometrical adequacy for vehicle redirection because sub-standard barriers can structurally withstand impact loads of high TLs. However, failure of the sub-standard barrier to satisfy the structural adequacy criterion is due to the barrier's geometrical inability to redirect the impacting vehicle.
2. AASHTO specifications accept sub-standard barriers as protection because they reduce the required ESF of bridge piers to withstand VCF.
3. Consideration should be given to the location of the ESF application point. Dynamic simulations showed that, with sub-standard barriers, the PIF location was within the range of heights adopted by AASHTO for the SUT. However, for the TST, the centroid location of the impact occurred at a much higher height due to impact with the trailer.

The presented research in each chapter is supported by a published article by the author, and the reader is encouraged to refer to these references for any additional information (Salahat et al. 2023, 2024, 2025).

References

Abdelkarim, O. I., & ElGawady, M. A. (2017). Performance of bridge piers under vehicle collision. *Engineering Structures*, *140*, 337–352. https://doi.org/10.1016/j.engstruct.2017.02.054

ACI Committee 318. (2014). *Building code requirements for structural concrete and commentary* (ACI 318-14). American Concrete Institute.

Agrawal, A. K., El-Tawil, S., Cao, R., Xu, X., Chen, X., & Wong, W. (2018). *A performance-based approach for loading definition of heavy vehicle impact events* (Report No. FHWA-HIF-18-062). Federal Highway Administration. https://rosap.ntl.bts.gov/view/dot/38226

Alberson, D. C., Williams, W. F., & Menges, W. L. (2005). *Testing and evaluation of the Florida F shape bridge rail with reduced deck thickness* (Report No. FHWA/TX-05/9-8132-3). Texas Transportation Institute. https://rosap.ntl.bts.gov/view/dot/86544

Al Shboul, K. W., Rasheed, H. A., & Alshareef, H. A. (2021). Intelligent approach for accurately predicting fatigue damage in overhead highway sign structures. *Structures*, *34*, 3453–3463. https://doi.org/10.1016/j.istruc.2021.09.090

American Association of State Highway and Transportation Officials (AASHTO). (1998). *AASHTO LRFD bridge design specifications: SI units* (2nd ed.).

American Association of State Highway and Transportation Officials (AASHTO). (2016). *Manual for assessing safety hardware* (2nd ed.).

American Association of State Highway and Transportation Officials (AASHTO). (2017). *LRFD bridge design specifications* (8th ed.).

American Association of State Highway and Transportation Officials (AASHTO). (2020). *AASHTO LRFD bridge design specifications* (9th ed.).

Atahan, A. O. (2009). Effect of permanent jersey-shaped concrete barrier height on heavy vehicle post-impact stability. *International Journal of Heavy Vehicle Systems*, *16*(1), 243–257. https://doi.org/10.1504/IJHVS.2009.023863

Bischoff, P. H., & Perry, S. H. (1995). Impact behavior of plain concrete loaded in uniaxial compression. *Journal of Engineering Mechanics*, *121*(6), 685–693. https://doi.org/10.1061/(ASCE)0733-9399(1995)121:6(685)

Bullard, D. L., Jr., Bligh, R. P., Menges, W. L., & Haug, R. R. (2010). *Volume 1: Evaluation of existing roadside safety hardware using updated criteria—Technical report* (NCHRP Web-Only Document 157). Transportation Research Board. https://doi.org/10.17226/22938

Buth, C. E., Brackin. M. S., Williams, W. F., & Fry, G. T. (2011). *Collision loads on bridge piers: Phase 2. Report of guidelines for designing bridge piers and abutments for vehicle collisions* (Report No. FHWA/TX-11/9-4973-2). Texas Transportation Institute.

Buth, C. E., Williams, W. F., Brackin, M. S., Lord, D., Geedipally, S. R., & Abu-Odeh, A. Y. (2010). *Analysis of large truck collisions with bridge piers: Phase 1. Report of guidelines for designing bridge piers and abutments for vehicle collisions* (Report No. FHWA-TX-10/9-4973-1). Texas Transportation Institute. https://rosap.ntl.bts.gov/view/dot/18040

Cao, R., Agrawal, A. K., El-Tawil, S., & Wong, W. (2020). Numerical studies on concrete barriers subject to MASH truck impact. *Journal of Bridge Engineering*, *25*(7), Article 04020035. https://doi.org/10.1061/(ASCE)BE.1943-5592.0001570

Consolazio, G. R., Chung, J. H., & Gurley, K. R. (2003). Impact simulation and full scale crash testing of a low profile concrete work zone barrier. *Computers & Structures*, *81*(13), 1359–1374. https://doi.org/10.1016/S0045-7949(03)00058-0

El-Tawil, S., Severino, E., & Fonseca, P. (2005). Vehicle collision with bridge piers. *Journal of Bridge Engineering*, *10*(3), 345–353. https://doi.org/10.1061/(ASCE)1084-0702(2005)10:3(345)

Federal Highway Administration (FHWA). (2022). *National bridge inventory*. Retrieved August 11, 2021, from https://www.fhwa.dot.gov/bridge/nbi/ascii2022.cfm

Google Maps. (n.d.). KS-177 Interstate 70 (S-W) [39.062, -96.5385]. Retrieved May 1, 2023, from https://maps.app.goo.gl/oxf2raqboqKtpXfU7

Harik, I. E., Shaaban, A. M., Gesund, H., Valli, G. Y. S., & Wang, S. T. (1990). United States bridge failures, 1951–1988. *Journal of Performance of Constructed Facilities*, *4*(4), 272–277. https://doi.org/10.1061/(ASCE)0887-3828(1990)4:4(272)

Hirsch, T. J. (1978). *Analytical evaluation of Texas bridge rails to contain buses and trucks* (Report No. FHWA/TX78-230-2). Texas Transportation Institute. https://library.ctr.utexas.edu/hostedpdfs/tti/230-2.pdf

Itoh, Y., Liu, C., & Kusama, R. (2007). Modeling and simulation of collisions of heavy trucks with concrete barriers. *Journal of Transportation Engineering*, *133*(8), 462–468. https://doi.org/10.1061/(ASCE)0733-947X(2007)133:8(462)

Jankowiak, T., & Łodygowski, T. (2005). Identification of parameters of concrete damage plasticity constitutive model. *Foundations of Civil and Environmental Engineering*, *6*, 53–69. https://www.researchgate.net/publication/228525599

Jeon, S.-J., Choi, M.-S., & Kim, Y.-J. (2008). Ultimate strength of concrete barrier by the yield line theory. *International Journal of Concrete Structures and Materials*, *2*(1), 57–62. https://doi.org/10.4334/IJCSM.2008.2.1.057

Livermore Software Technology Corporation. (2017). *LS-DYNA® keyword user's manual* (LS-DYNA R10.0).

Loken, A. E., Steelman, J. S., Rosenbaugh, S. K., Faller, R. K., & Holt, J. M. (2021). Comparison of modified yield-line and punching shear capacities for concrete traffic barriers and bridge rails. *Transportation Research Record: Journal of the Transportation Research Board*, *2675*(12), 689–701. https://doi.org/10.1177/03611981211031222

Miele, C. R., Plaxico, C., Stephens, D., & Simunovic, S. (2010). *U26: Enhanced finite element analysis crash model of tractor-trailers (Phase C)*. National Transportation Research Center, Inc. https://rosap.ntl.bts.gov/view/dot/18333

Murray, Y. D. (2007). *Users manual for LS-DYNA concrete material model 159* (Report No. FHWA-HRT-05-062). Federal Highway Administration. https://rosap.ntl.bts.gov/view/dot/38730

National Transportation Research Center, Inc. (NTRCI). (2005). *F800 single unit truck FEM model for crash simulations with LS-DYNA*. Retrieved February 9, 2022, from https://thyme.ornl.gov/FHWA/F800WebPage/downloads/downloads.html

Nemec, N. (2013, July 18). *Designing bridges for vehicular collisions* [Webinar slides]. Texas Department of Transportation. https://ftp.txdot.gov/pub/txdot-info/brg/071813-webinar/nemec.pdf

Rasheed, H., & Abouelleil, A. (2015). *KDOT column expert: Ultimate shear capacity of circular columns using the simplified modified compression field theory* (Report No. MATC-KSU: 262). Kansas State University.

Rosenbaugh, S., Sicking, D. L., & Faller, R. K. (2007). *Development of a TL-5 vertical faced concrete median barrier incorporating head ejection criteria* (Report No. TRP-03-194-07). Midwest Roadside Safety Facility. https://rosap.ntl.bts.gov/view/dot/39293

Ross, C. A., Tedesco, J. W., & Kuennen, S. T. (1995). Effects of strain rate on concrete strength. *ACI Materials Journal*, *92*(1), 37–47. https://doi.org/10.14359/1175

Ross, H. E., Jr., Sicking, D. L., Zimmer, R. A., & Michie, J. D. (1993). *Recommended procedures for the safety performance evaluation of highway features* (NCHRP Report No. 350). Transportation Research Board.

Roy, S., Unobe, I., & Sorensen, A. D. (2021). Vehicle-impact damage of reinforced concrete bridge piers: A state-of-the art review. *Journal of Performance of Constructed Facilities*, *35*(5), Article 03121001. https://doi.org/10.1061/(ASCE)CF.1943-5509.0001613

SAE J211-1. (1995, March). *Instrumentation for impact test—Part 1—Electronic instrumentation*. SAE International. https://doi.org/10.4271/J211/1_199503

Salahat, F. H., Jones, C. A., & Rasheed, H. A. (2023). Estimation of vehicular collision force on bridge piers in the presence of sub-standard intervening concrete barriers. *Transportation Research Record: Journal of the Transportation Research Board*, *2677*(7), 326–339. https://doi.org/10.1177/03611981231152463

Salahat, F. H., Jones, C. A., & Rasheed, H. A. (2024). Assessment of substandard concrete barriers as protective structures to bridge piers against vehicular collision force. *Journal of Bridge Engineering*, *29*(7). https://doi.org/10.1061/JBENF2.BEENG-6624

Salahat, F. H., & Martinez-Vazquez, P. (2015). Seismic effects on structures located in the region of Palestine: A critical review on international building regulations. *International Journal of Civil and Structural Engineering*, *2*(1), 42–46. http://journals.theired.org/assets/pdf/20150423_120351.pdf

Salahat, F. H., Rasheed, H. A., Jones, C. A., & Klugh, I. (2025). Improved yield line analysis and innovative methodology to evaluate the capacity of RC barriers subjected to vehicular collision force. *Infrastructures*, *10*(4), 81. https://doi.org/10.3390/infrastructures10040081

Sennah, K., Tropynina, E., Ibrahim, Z., & Hedjazi, S. (2018). Structural qualification of a developed GFRP-reinforced concrete bridge barrier using ultimate load testing. *International Journal of Concrete Structures and Materials*, *12*, Article 63. https://doi.org/10.1186/s40069-018-0284-1

Sharma, H., Hurlebaus, S., & Gardoni, P. (2012). Performance-based response evaluation of reinforced concrete columns subject to vehicle impact. *International Journal of Impact Engineering*, *43*, 52–62. https://doi.org/10.1016/j.ijimpeng.2011.11.007

Sheikh, N. M., Bligh, R. P., & Menges, W. L. (2011). *Determination of minimum height and lateral design load for MASH test level 4 bridge rails* (Report No. FHWA/TX-12/9-1002-5). Texas Transportation Institute. https://rosap.ntl.bts.gov/view/dot/23779

Trajkovski, J., Ambrož, M., & Kunc, R. (2018). The importance of friction coefficient between vehicle tyres and concrete safety barrier to vehicle rollover – FE analysis study. *Journal of Mechanical Engineering*, *64*(12), 753–762. https://doi.org/10.5545/sv-jme.2018.5290

Wardhana, K., & Hadipriono, F. C. (2003). Analysis of recent bridge failures in the United States. *Journal of Performance of Constructed Facilities*, *17*(3), 144–150. https://doi.org/10.1061/(ASCE)0887-3828(2003)17:3(144)

Williams, W. F., Buth, C. E., & Menges, W. L. (2007). *Repair/retrofit anchorage designs for bridge rails* (Report No. 0-4823-T1-1). Texas Transportation Institute. https://rosap.ntl.bts.gov/view/dot/37988

Zhou, D., & Li, R. (2018). Damage assessment of bridge piers subjected to vehicle collision. *Advances in Structural Engineering*, *21*(15), 2270–2281. https://doi.org/10.1177/1369433218772344

Zhou, D., Li, R., Wang, J., & Guo, C. (2017). Study on impact behavior and impact force of bridge pier subjected to vehicle collision. *Shock and Vibration*, *2017*, Article 7085392. https://doi.org/10.1155/2017/7085392

Appendix

Table A.1: Sectional Capacity from AASHTO YLA Procedure

Property	Mz		Mx (for 1ft segment width)		
	Section 1 (Z_1= 0-22 in)	Section 2 (Z_1= 22-32 in)	Section 1 (Z_1= 0 in)	Section 2 (Z_2= 22	Section 3 (Z_3= 32 in)
b (in)	22	10	12	12	12
h (in)	(7.5+9.75)/2=8.625	(14.75+9.75)/2=12.25	7.5	9.75	14.75
c (in)	4.3125	6.125	3.75	4.875	7.375
Ig (in^4)	1176.3	1531.8	421.875	926.86	3209
Moment	118.64 kip.in	129.38 kip.in	53.4 kip.in	90.2 kip.in	206.4 kip.in
	Sum = 248 kip.in = 20.67 kip.ft		Weighted avg. = (0.5(53.4+90.2)22+0.5 (90.2+206.4)10)/32 = 95.7 kip.in = 8 kip.ft		

Table A.2: Back-Side Sectional Capacity around the Vertical Axis

	Back Side	
Step	Section 1 (Z_1= 0 – 22 in.)	Section 2 (Z_2= 22 – 32 in.)
1	$\frac{As}{h} = \frac{0.44 + 0.2 + 0.2}{32} = 0.02625\ in^2/in$	
2	$Avg.Cover = \frac{3.62 \times 0.44 + 2.36 \times 0.2 + 2.36 \times 0.2}{0.84} = 3\ in.$	
3	$d_0 = 7.5 - 3 = 4.5\ in.$ $d_{z1} = 4.5 + Slope1 \times Z_1$ $= 4.5 + 0.1025\ Z_1$	$d_0 = 7.5 + Slope1 \times Z_1 - 3$ $d_{z2} = 6.755 + Slope2 \times Z_2$ $= 6.755 + 0.5\ Z_2$
4	$M_{Z1} = A_s\ f_y\ \left(d - \frac{a}{2}\right)$ $a = \frac{A_s\ f_y}{0.85\ fc'b} = \frac{0.84 \times\ 60}{0.85\ \times 4 \times 32} = 0.463\ in$ $M_{Z1} = 0.02625 \times 60 \times \left(4.5 + 0.1025\ Z_1 - \frac{0.463}{2}\right)$	$M_{Z2} = A_s\ f_y\ \left(d - \frac{a}{2}\right)$ $a = \frac{A_s\ f_y}{0.85\ fc'b} = \frac{0.84 \times 60}{0.85\ \times 4 \times 32} = 0.463\ mm$ $M_{Z2} = 0.02625 \times 60 \times \left(6.755 + 0.5\ Z_2 - \frac{0.463}{2}\right)$
5	$M_{Z1} = 6.723 + 0.1615 \times Z_1\ kips.in/in$	$M_{Z2} = 10.2745 + 0.7875 \times Z_2\ kips.in/in$ $M_{Z2} = 18.14 - 0.7875\ (32 - Z_2)\ kips.in/in$

Table A.3: Front-Side Sectional Capacity around the Vertical Axis

	Front Side	
Step	Section 1 (Z_1= 0 – 22 in.)	Section 2 (Z_2= 22 – 32 in.)
1	$\frac{As}{h} = \frac{0.44 + 0.2 + 0.2 + 0.2 + 0.2}{32} = 0.03875\ in^2/in$	
2	$Avg.Cover = \frac{4.21 \times 0.44 + 3 \times 0.2 + 3 \times 0.2 + 4.8 \times 0.2 + 1.77 \times 0.2}{1.24} = 3.52\ mm$	
3	$d_0 = 7.5 - 3.52 = 3.98\ in.$ $d_{z1} = 3.98 + Slope1 \times Z_1$ $= 3.98 + 0.1025\ Z_1$	$d_0 = 7.5 + Slope1 \times Z_1 - 3.52$ $d_{z2} = 6.235 + Slope2 \times Z_2$ $= 6.235 + 0.5\ Z_2$
4	$M_{Z1} = A_s\ f_y\ \left(d - \frac{a}{2}\right)$ $a = \frac{A_s\ f_y}{0.85\ fc'b} = \frac{1.24 \times\ 60}{0.85\ \times 4 \times 32} = 0.684\ in.$ $M_{Z1} = 0.0387 \times 60 \times \left(3.98 + 0.1025\ Z_1 - \frac{0.684}{2}\right)$	$M_{Z2} = A_s\ f_y\ \left(d - \frac{a}{2}\right)$ $a = \frac{A_s\ f_y}{0.85\ fc'b} = \frac{1.24 \times\ 60}{0.85\ \times 4 \times 32} = 0.684\ in.$ $M_{Z2} = 0.03875 \times 60 \times \left(6.235 + 0.5\ Z_2 - \frac{0.684}{2}\right)$
5	$M_{Z1} = 8.447 + 0.2383 \times Z_1\ kips.in/in$	$M_{Z2} = 13.7 + 1.1625 \times Z_2\ kN.mm/mm$ $M_{Z2} = 25.325 - 1.1625\ (32 - Z_2)\ kips.in/in$

The equations below are the general equations adopted in step 5 of Table A.3.

$$\boldsymbol{M_{z\_back}(z)} = \begin{cases} \boldsymbol{6.723 + 0.1615\ z\ kips.\frac{in}{in}} & , \quad \boldsymbol{0 \le z \le 22} \\ \boldsymbol{18.14 - 0.7875\ (32 - z)\ kips.\frac{in}{in}}, & \boldsymbol{22 \le z \le 32} \end{cases}$$

$$\boldsymbol{M_{z\_front}(z)} = \begin{cases} \boldsymbol{8.447 + 0.2383\ z\ kips.\frac{in}{in}} & , \quad \boldsymbol{0 \le z \le 22} \\ \boldsymbol{25.325 - 1.1625\ (32 - z) kips.\frac{in}{in}} & , \quad \boldsymbol{22 \le z \le 32} \end{cases}$$

Table A.4: Back-Side Sectional Capacity around the Longitudinal Axis

Step	Back Side		
1	Section 1 (Z_1= 0 in)	Section 2 (Z_2= 22 in)	Section 3 (Z_3= 32 in)
2	$\frac{As}{b} = \frac{0}{12} = 0\ in^2/in$	$\frac{As}{b} = \frac{0.62}{12} = 0.0516\ in^2/in$	$\frac{As}{b} = \frac{0.31}{12} = 0.026\ in^2/in$
3	$M_{Z1} = \frac{f_r\, I}{h/_2}\frac{1}{12}$ $fr = 7.5\sqrt{4000} = 474.3\ psi = 0.474\ ksi$ $I = \frac{bh^3}{12} = \frac{12 \times 7.5^3}{12} = 421.9\ in^4$ $M_{Z1} = \frac{0.474 \times 421.9}{7.5 \times 12/_2} = 4.443\ kips.in/in$	$d = 7.5 + Slope1 \times Z_2 - cover - 0.5 \times \emptyset_{stirrup}$ $d = 7.5 + 0.1025 \times 22 - 1.5 - 0.3125 = 7.94\ in.$ $M_{Z2} = A_s\, f_y \left(d - \frac{a}{2}\right)$ $a = \frac{A_s\, f_y}{0.85\, fc'b} = \frac{0.62 \times 60}{0.85 \times 4 \times 12} = 0.91\ in.$ $M_{Z2} = 0.0516 \times 60 \times \left(7.94 - \frac{0.91}{2}\right) = 23.18\ kips.in/in$	$d = 14.75 - cover - 0.5 \times \emptyset_{stirrup}$ $d = 14.75 - 1.5 - 0.3125 = 12.9375\ in$ $M_{Z3} = A_s\, f_y \left(d - \frac{a}{2}\right)$ $a = \frac{A_s\, f_y}{0.85\, fc'b} = \frac{031 \times 60}{0.85 \times 4 \times 12} = 0.456\ in$ $M_{Z3} = 0.026 \times 60 \times \left(12.9375 - \frac{0.456}{2}\right) = 19.83\ kips.in/in$
4	$slope_{12} = 0.8517$		
		$slope_{23} = -0.3353$	
5	$M_{x\_back}(z) = \begin{cases} M_{Z1} + slope_{12}\, Z\ kips.\frac{in}{in}, & 0 \le z \le 22 \\ M_{Z3} - slope_{23}(height - Z)\ kips.\frac{in}{in}, & 22 \le z \le 32 \end{cases} \rightarrow M_{x\_back}(z) = \begin{cases} 4.443 + 0.8517\, Z\ kips.\frac{in}{in}, & 0 \le z \le 22 \\ 19.83 + 0.3353(32 - Z)\ kips.\frac{in}{in}, & 22 \le z \le 32 \end{cases}$		

Table A.5: Front-Side Sectional Capacity around the Longitudinal Axis

Step	Front Side		
1	Section 1 (Z_1= 0 in.)	Section 2 (Z_2= 22 in.)	Section 3 (Z_3= 32 in.)
2	$\frac{As}{b} = \frac{0}{12} = 0\ in^2/in$	$\frac{As}{b} = \frac{0.62}{12} = 0.0516\ in^2/in$	$\frac{As}{b} = \frac{0.31}{12} = 0.026\ in^2/in$
3	$M_{Z1} = \frac{f_r\, I\, 1}{h/_2\ 12}$ $fr = 7.5\sqrt{4000} = 474.3\ psi = 0.474\ ksi$ $I = \frac{bh^3}{12} = \frac{12 \times 7.5^3}{12} = 421.9\ in^4$ $M_{Z1} = \frac{0.474 \times 421.9}{7.5 \times 12/_2} = 4.443\ kips.in/in$	$d = 7.5 + Slope1 \times Z_2 - cover - 0.5 \times \emptyset_{stirrup}$ $d = 7.5 + 0.1025 \times 22 - 2.12 - 0.3125$ $= 7.32\ in.$ $M_{Z2} = A_s\, f_y \left(d - \frac{a}{2}\right)$ $a = \frac{A_s\, f_y}{0.85\, fc'b} = \frac{0.62 \times 60}{0.85 \times 4 \times 12} = 0.91\ in.$ $M_{Z2} = 0.0516 \times 60 \times \left(7.32 - \frac{0.91}{2}\right)$ $= 21.25\ kips.in/in$	$d = 14.75 - cover - 0.5 \times \emptyset_{stirrup}$ $d = 14.75 - 3 - 0.3125 = 11.4375\ in.$ $M_{Z3} = A_s\, f_y \left(d - \frac{a}{2}\right)$ $a = \frac{A_s\, f_y}{0.85\, fc'b} = \frac{0.31 \times 60}{0.85 \times 4 \times 12} = 0.456\ in.$ $M_{Z3} = 0.026 \times 60 \times \left(11.4375 - \frac{0.456}{2}\right)$ $= 17.487\ kips.in/in$
4	$slope_{12} = 0.764$		
		$slope_{23} = -0.3763$	
5	$M_{x\_front}(z) = \begin{cases} M_{Z1} + slope_{12}\, Z\ \ kips.\frac{in}{in}, & 0 \le z \le 22 \\ M_{Z3} - slope_{23}(height - Z)\ \ kips.\frac{in}{in}, & 22 \le z \le 32 \end{cases} \rightarrow M_{x\_front}(z) = \begin{cases} 4.443 + 0.764\, Z\ kips.\frac{in}{in}, & 0 \le z \le 22 \\ 17.487 + 0.3763\ (32 - Z)\ \ kips.\frac{in}{in}, & 22 \le z \le 32 \end{cases}$		

The equations below are the general equations adopted in step 5 of Table A.5.

$$\boldsymbol{M_{x\_back}(z)} = \begin{cases} \boldsymbol{14.443 + 0.8517\, z\ kips.\frac{in}{in}}, & \boldsymbol{0 \le z \le 22} \\ \boldsymbol{19.83 + 0.3353(32 - z)\ kips.\frac{in}{in}}, & \boldsymbol{22 \le z \le 32} \end{cases}$$

$$\boldsymbol{M_{x\_front}(z)} = \begin{cases} \boldsymbol{4.443 + 0.764\, z\ kips.\frac{in}{in}}, & \boldsymbol{0 \le z \le 22} \\ \boldsymbol{17.487 + 0.3763\ (32 - z)\ kips.\frac{in}{in}}, & \boldsymbol{22 \le z \le 32} \end{cases}$$

K-TRAN

KANSAS TRANSPORTATION RESEARCH AND NEW-DEVELOPMENT PROGRAM

AD ASTRA PER ASPERA

Kansas

Department of Transportation